

NANOPOROUS GLASS-CERAMICS FOR GAS SEPARATION

BY

MICHELENE E. MILLER

A THESIS

SUBMITTED TO THE FACULTY OF

ALFRED UNIVERSITY

IN PARTIAL FULFILLMENT OF THE REQUIREMENTS
FOR THE DEGREE OF

DOCTOR OF PHILOSOPHY

IN

MATERIALS SCIENCE AND ENGINEERING

ALFRED, NEW YORK

DECEMBER, 2008

Alfred University theses are copyright protected and may be used for education or personal research only. Reproduction or distribution in part or whole is prohibited without written permission from the author.

NANOPOROUS GLASS-CERAMICS FOR GAS SEPARATION

BY

MICHELENE E. MILLER

B.S. ALFRED UNIVERSITY (2004)

M.S. ALFRED UNIVERSITY (2005)

SIGNATURE OF AUTHOR _____ (Signature on file)

APPROVED BY _____ (Signature on file)

SCOTT T. MISTURE, ADVISOR

(Signature on file)

WILLIAM M. CARTY, ADVISORY COMMITTEE

(Signature on file)

DOREEN D. EDWARDS, ADVISORY COMMITTEE

(Signature on file)

WILLIAM C. LACOURSE, ADVISORY COMMITTEE

(Signature on file)

DOREEN D. EDWARDS, CHAIR
ORAL THESIS DEFENSE

ACCEPTED BY _____ (Signature on file)

ALASTAIR N. CORMACK, DEAN
KAZUO INAMORI SCHOOL OF ENGINEERING

ACCEPTED BY _____ (Signature on file)

WILLIAM M. HALL, ASSOCIATE PROVOST FOR
GRADUATE AND PROFESSIONAL PROGRAMS
ALFRED UNIVERSITY

ACKNOWLEDGMENTS

I would like to thank the following people who have made significant contributions to assist me during my term as a graduate student.

- Dr. Misture who is amongst the best facilitators. The opportunity to present our work at several conferences enabled me to improve my presentation skills. His continual support and high expectations for his students and their research has given me every opportunity to excel.
- Swavek for fielding any and every question, and fixing everything.
- My committee for providing insightful revisions to my thesis.
- Dr. Shelby for the hands on training earlier in my graduate career which gave me confidence in the lab. I would not have accomplished nearly as much in my graduate career had it not been for Dr. Shelby's patience, and basic training both in and out of the classroom.
- All Alfred faculty and graduate students for both teaching and sharing their research experiences with me.
- My family (including Lola) who has supported all of my endeavors beyond the lab.
- Matt for being my sounding board through the steady stream of the highs and lows encountered in my research.

TABLE OF CONTENTS

Introduction	1
Methane Steam Reforming (MSR)	1
Gas Separation Membranes.....	2
Microporous Membranes	2
Dense Inorganic Membranes.....	3
Novel Processing of Microporous Glass-Ceramics	4
Ni-containing Cordierite Glass-Ceramics	5
Thesis Scope.....	7
References	8
Chapter 1: Stoichiometric Nickel Cordierite Glass-Ceramics.....	10
1.1 Abstract.....	10
1.2 Introduction	11
1.3 Experimental procedure	12
1.3.1 Kinetics study (DTA and HTXRD measurements)	12
1.3.2 Glass properties study (dilatometer measurements only).....	12
1.4 Results	13
1.4.1 Glass properties	13
1.4.2 Crystallization	14
1.4.3 Transformation kinetics	15
1.4.3.1 Non-isothermal analysis (Kissinger method).....	15
1.4.3.2 Isothermal analysis (JMAK)	16
1.4.4 $\text{Ni}_x\text{Mg}_{2-x}\text{Al}_4\text{Si}_5\text{O}_{18}$ cordierite	18
1.4.5 $\text{Ni}_x\text{Mg}_{1-x}\text{Al}_2\text{O}_4$ spinel.....	18
1.5 Discussion.....	19
1.5.1 Glass properties	19
1.5.2 Crystallization	19
1.5.3 Transformation kinetics	20
1.5.4 $\text{Ni}_x\text{Mg}_{2-x}\text{Al}_4\text{Si}_5\text{O}_{18}$ cordierite	21
1.5.5 $\text{Ni}_x\text{Mg}_{1-x}\text{Al}_2\text{O}_4$ spinel.....	21

1.6 Conclusions	22
1.7 References.....	23
1.8 Tables	24
1.9 Figures	26
Justification of single phase $\text{Ni}_x\text{Mg}_{1-x}\text{Al}_2\text{O}_4$ spinel studies.....	34
Chapter 2: Defect Structure of Alumina-rich Magnesium Aluminate Spinel.....	35
2.1 Abstract.....	35
2.2 Introduction	36
2.3 Experimental procedure	37
2.4 Results.....	38
2.4.1 $\text{Ni}_x\text{Mg}_{1-x}\text{Al}_2\text{O}_4$ spinel structure.....	38
2.4.2 H_2 reaction with $\text{Ni}_x\text{Mg}_{1-x}\text{Al}_2\text{O}_4$ spinel.....	38
2.4.2.1 Products of the H_2 reaction	38
2.4.2.2 Stability of the spinel framework	38
2.4.2.3 Quantification of phases	39
2.4.2.4 Defect spinel structure	39
2.4.2.5 Formation of $V_{\text{Ni}}^{\bullet\bullet}$	39
2.4.2.6 Formation of V_{O}^{\bullet}	40
2.4.2.7 Non-stoichiometric spinel lattice parameters	41
2.4.3 Re-oxidation/Reverse Reactions	41
2.4.3.1 Quantification of phases	41
2.4.3.2 Spinel lattice parameter	42
2.4.3.3 Weight gain during re-oxidation	42
2.5 Discussion.....	42
2.5.1 $\text{Ni}_x\text{Mg}_{1-x}\text{Al}_2\text{O}_4$ spinel structure.....	42
2.5.2 H_2 reaction with $\text{Ni}_x\text{Mg}_{1-x}\text{Al}_2\text{O}_4$	43
2.5.3 Re-oxidation/Reverse Reactions	44
2.5.4 Defect spinel structure.....	45
2.5.5 Relating alumina-rich spinel to $\gamma\text{-Al}_2\text{O}_3$	46
2.5.5.1 Transition from $\text{Mg}_{1-x}\text{Al}_2\text{O}_4$ spinel to $\gamma\text{-Al}_2\text{O}_3$	46
2.5.5.2 Applying the alumina-rich spinel defect equation to $\gamma\text{-Al}_2\text{O}_3$	47

2.5.5.3 Porosity inherent to defect spinel structures	47
2.6 Conclusions	48
2.7 References.....	50
2.8 Tables	52
2.9 Figures.....	53
Chapter 3: (Ni,Mg)-aluminate Spinel Catalysts.....	65
3.1 Abstract.....	65
3.2 Introduction	66
3.3 Experimental procedure	67
3.4 Results.....	68
3.4.1 Formation of metallic nickel	68
3.4.2 Temperature vs. size of crystallites	68
3.4.3 Time vs. size of crystallites.....	68
3.4.4 Wt % of metallic Ni vs. Size.....	69
3.4.5 Reaction products.....	69
3.4.5.1 Spinel stability limits.....	69
3.4.5.2 Transition sequence for $\text{Ni}_{0.75}\text{Mg}_{0.25}\text{Al}_2\text{O}_4$ and NiAl_2O_4	70
3.4.5.3 Quantification of phases	70
3.4.6 Re-oxidation of reduced (Ni,Mg)-aluminate spinels.....	71
3.4.7 Spinel structure.....	71
3.4.7.1 Lattice Constant & Strain	71
3.5 Discussion.....	72
3.5.1 Formation of metallic nickel	72
3.5.2 Reaction products.....	73
3.5.2.1 Spinel stability limits.....	73
3.5.2.2 Transition sequence for $\text{Ni}_{0.75}\text{Mg}_{0.25}\text{Al}_2\text{O}_4$ and NiAl_2O_4	73
3.5.3 Quantification of phases	75
3.5.4 Re-oxidation of reduced (Ni,Mg)-aluminate spinels.....	75
3.5.5 Spinel structure.....	76
3.5.5.1 Lattice strain.....	76
3.6 Conclusion	77

3.7 References.....	78
3.8 Tables	81
3.9 Figures	82
Linking spinel glass-ceramics to single phase spinel.....	90
Appendix 1: NiO MgO Al ₂ O ₃ SiO ₂ Glasses.....	92
A1.1 Introduction.....	92
A1.2 Experimental Procedures	92
A1.3 Results and discussion	93
A1.3.1 Glass transition temperature	93
A1.3.2 Crystallization temperatures.....	94
A1.3.3 Hot stage microscope (HSM)	95
A1.4 Conclusions	95
A1.5 Suggestions.....	96
A1.6 References	97
A1.7 Tables.....	98
A1.8 Figures.....	99
Appendix 2: Measuring high temperature permeability.....	107
A2.1 Pressure-drop technique	107
A2.2 High temperature permeability apparatus.....	107
A2.3 References	108
A2.4 Figures.....	108

LIST OF TABLES

Table I.	CTE, T_g , and T_d for β -quartz, Cordierite and Spinel in $x\text{NiO}$ $(2-x)\text{MgO}$ $2\text{Al}_2\text{O}_3$ 5SiO_2 Glasses.....	24
Table II.	Activation Energies for β -quartz Crystallization and β -quartz to Cordierite Transformation.....	24
Table III.	JMAK Parameters for β -quartz Crystallization and β -quartz to Cordierite Transformation.....	25
Table IV.	Lattice Parameters for the Spinel Phase Crystallizing in $x\text{NiO}$ $(2-x)\text{MgO}$ $2\text{Al}_2\text{O}_3$ 5SiO_2 Glasses	25
Table V.	Reaction Temperatures and Times for $\text{Ni}_x\text{Mg}_{1-x}\text{Al}_2\text{O}_4$ Spinel Solid Solution, where $0 \leq x \leq 1$, in ~ 300 torr of H_2	52
Table VI.	Reaction Temperatures and Times for the Spinel Series $\text{Ni}_x\text{Mg}_{1-x}\text{Al}_2\text{O}_4$, where $0 \leq x \leq 1$, in 300 torr of H_2	81
Table VII.	$\text{NiO-MgO-Al}_2\text{O}_3\text{-SiO}_2$ Glass Properties	98

LIST OF FIGURES

Figure 1.	A flow diagram for the processing of novel microporous glass-ceramic membranes for H ₂ separation.	5
Figure 2.	Projections of the orthorhombic cordierite crystal structure.	6
Figure 3.	A DTA plot of xNiO (2-x)MgO 2Al ₂ O ₃ 5SiO ₂ glasses showing the crystallization behavior as a function of nickel content.	26
Figure 4.	DTA data for NiO MgO 2Al ₂ O ₃ 5SiO ₂ glass collected at various heating rates.	27
Figure 5.	A series of HTXRD patterns collected in 1200 second intervals at 1010°C showing the crystallization of cordierite glass.	28
Figure 6.	A Kissinger plot for β-quartz crystallization and the β-quartz to cordierite transformation determined using DTA.	29
Figure 7.	(a) The series of HTXRD patterns for the 0.75NiO 1.25MgO 2Al ₂ O ₃ 5SiO ₂ glass heated at 942°C to crystallize β-quartz.	30
Figure 8.	JMAK plot for β-quartz crystallization in xNiO (2-x)MgO 2Al ₂ O ₃ 5SiO ₂ glasses determined using HTXRD.	31
Figure 9.	JMAK plot for cordierite crystallization in xNiO (2-x)MgO 2Al ₂ O ₃ 5SiO ₂ glasses determined using HTXRD.	32
Figure 10.	The effect of Ni ²⁺ substituted for Mg ²⁺ on the axial expansion in Ni _x Mg _{2-x} Al ₄ Si ₅ O ₁₈ cordierite.	33
Figure 11.	HTXRD pattern for NiO MgO 2Al ₂ O ₃ 5SiO ₂ glass-ceramic reacted with H ₂ at 950°C in 1 hr intervals.	34
Figure 12.	The change in lattice parameter as a function of x for Ni _x Mg _{1-x} Al ₂ O ₄	53
Figure 13.	An example refinement of XRD data for Ni _{0.5} Mg _{0.5} Al ₂ O ₄ reacted at 850°C for 24 hrs in H ₂	54
Figure 14.	X-ray diffraction data illustrating the transformation of NiAl ₂ O ₄ to metastable alumina polymorphs.	55
Figure 15.	The normalized fraction of nickel vacancies formed and the weight percent of metallic nickel formed.	56
Figure 16.	TGA data illustrating the weight loss for the spinel samples as a function of temperature.	57
Figure 17.	The experimentally determined weight loss in the spinel compositions Ni _x Mg _{1-x} Al ₂ O ₄ during reaction with hydrogen.	58
Figure 18.	(a) In situ XRD of Ni _{0.5} Mg _{0.5} Al ₂ O ₄ in flowing 4H ₂ -96N ₂ at 800°C. (b) Change in lattice parameter as spinel reacts with H ₂	59

Figure 19. Change in lattice parameter for non-stoichiometric spinel compositions.	60
Figure 20. The weight percent of phases calculated from in situ XRD data recorded for the re-oxidation of Ni + Mg _{0.5} Al ₂ O _{3.5}	61
Figure 21. In situ TGA data showing the weight gain as Ni + Mg _{0.5} Al ₂ O _{3.5} re-oxidizes to form Ni _{0.5} Mg _{0.5} Al ₂ O ₄	62
Figure 22. The change in the spinel lattice parameter recorded in situ for the re-oxidation of Ni + Mg _{0.5} Al ₂ O _{3.5}	63
Figure 23. The percent free volume in Ni _x Mg _{1-x} Al ₂ O ₄ and Mg _{1-x} Al ₂ O _{4-x} calculated using the measured lattice parameters.	64
Figure 24. A SEM micrograph illustrating the formation of metallic nickel crystallites evenly dispersed on the surface of spinel.....	82
Figure 25. A plot of the average crystallite size for nickel at the specified reaction temperatures.	83
Figure 26. The relationship between the average crystallite size and the weight percent of metallic nickel formed.....	84
Figure 27. An example of the Rietveld refinement of X-ray diffraction data.....	85
Figure 28. The weight percent of metallic nickel formed during reaction with hydrogen at the specified reaction temperature.....	86
Figure 29. The reaction products for NiAl ₂ O ₄ with H ₂ at the indicated temperatures.	87
Figure 30. The change in lattice parameter as a function of reaction temperature for Ni _{0.5} Mg _{0.5} Al ₂ O ₄	88
Figure 31. The phase transformation sequence during the re-oxidation of Ni supported on non-stoichiometric spinel.....	89
Figure 32. HTXRD pattern for NiO MgO 2Al ₂ O ₃ 5SiO ₂ glass-ceramic reacted with H ₂ at 1000°C in flowing 4H ₂ -96N ₂	91
Figure 33. The NiO-MgO-Al ₂ O ₃ -SiO ₂ glass compositions (wt %) for which the viscosity and crystallization behavior are analyzed.	99
Figure 34. The effect of NiO-MgO on the glass transition temperature in NiO-MgO-Al ₂ O ₃ -SiO ₂ glasses.....	100
Figure 35. The effect of Al ₂ O ₃ on the glass transition temperature in NiO-MgO-Al ₂ O ₃ -SiO ₂ glasses.	101
Figure 36. The effect of SiO ₂ on the glass transition temperature in NiO-MgO-Al ₂ O ₃ -SiO ₂ glasses.	102
Figure 37. The effect of NiO-MgO on the crystallization temperatures for spinel and β-quartz in NiO-MgO-Al ₂ O ₃ -SiO ₂ glasses.....	103

Figure 38. The effect of Al_2O_3 on the crystallization temperatures for spinel and β -quartz in NiO-MgO- Al_2O_3 - SiO_2 glasses.....	104
Figure 39. The effect of SiO_2 on the crystallization temperatures for spinel and β -quartz in NiO-MgO- Al_2O_3 - SiO_2 glasses.....	105
Figure 40. HSM data for 11.9NiO 19.8MgO 11.7 Al_2O_3 56.6 SiO_2 glass recorded at 10 K/min.....	106
Figure 41. Pressure-drop measurement for the determination of hydrogen permeability through porous monoliths.....	108
Figure 42. Stainless steel sample holder for high temperature permeability measurements.	109

ABSTRACT

The development of nanoporous gas separation membranes to extract H₂ from a mixed fuel stream of CH₄/H₂O/CO₂/CO is desirable for use in methane steam reforming reactions. Ni-containing cordierite glass-ceramics are candidate materials for this application. The final microstructure of these glass-ceramics includes two sieving mechanisms: (1) a 5 Å channel inherent to the cordierite crystal structure which grows normal to the surface of the glass, and (2) a nanoporous non-stoichiometric spinel in the bulk with theoretical pore diameters ranging from 4-8 Å.

Through reaction with hydrogen we demonstrate the ability to form nanopores in Ni_xMg_{1-x}Al₂O₄ spinel. The stability limit for the non-stoichiometric spinel formed during the H₂ reaction lies between 0.5 ≤ x ≤ 0.75. The formation of an equal number of nickel and oxygen vacancies in spinel is determined using Rietveld refinement of X-ray diffraction data and thermogravimetric analysis. These vacant sites form the nanopores in the defect spinel structure.

INTRODUCTION

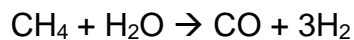
Recent global climate changes have raised both awareness and concern for the long term effects of elevated greenhouse gas emissions on global warming. Scientists believe that the accumulation of anthropogenic carbon dioxide (CO₂) emissions in the atmosphere is one cause of rising surface temperatures and subsurface ocean temperatures.

The primary source of energy worldwide derives from the combustion of fossil fuels – the largest single contributor to anthropogenic greenhouse gas emissions in the United States and the world. In 2004, CO₂ accounted for more than 80 % of greenhouse gas emissions in the U.S, 98 % of which resulted from the combustion of fossil fuels.¹

The world's energy consumption is anticipated to double by the year 2050 with an increasing standard of living.² The projected energy demands cannot be sustained with current U.S. energy resources. Additionally, current methods of energy production lead to unacceptable levels of CO₂ emissions. Shifting to a hydrogen economy offers the potential to sustain the world's energy needs while limiting the accumulation of CO₂ in the atmosphere.

Methane Steam Reforming (MSR)

Steam reforming of methane and light hydrocarbons is the primary method for producing hydrogen today.³ The process involves the reversible reaction of high temperature steam with methane over a catalyst to produce hydrogen and carbon monoxide. A variety of carbon sources including natural gas, liquid petroleum, naphtha or refinery off-gas can be used in this reaction.⁴



The products of this reversible reaction are controlled predominately by thermodynamics. The favored product at low temperatures is methane while hydrogen is preferred at high temperatures > 800°C. Integration of a separation membrane into the reactor simplifies the chemical process by driving the reaction forward through the selective removal of at least one product. In this case, the

selective removal of hydrogen from the reactor will drive the reaction beyond the thermodynamic equilibrium.

The extraction of hydrogen from the mixed gas stream consisting of $\text{CO}_2/\text{CO}/\text{CH}_4/\text{H}_2\text{O}$ that is produced in the methane steam reforming reaction is beneficial to a future hydrogen-based economy. The use of separation membranes capable of functioning in extreme chemical environments are essential for efficiently producing hydrogen in MSR and improving the efficiency of the reactor.⁵ The gained efficiency of the combined hydrogen production and separation processes into one reactor will reduce CO_2 emissions. The use of separation membranes is more cost effective and has potential for higher purification levels than existing methods of separation.⁶

Gas Separation Membranes

Gas separation membranes that are suitable for high temperature application can be broken down into two categories; microporous membranes and dense inorganic membranes.

Microporous Membranes

A micropore is defined as a pore less than 2 nm in diameter by the International Union of Pure and Applied Chemistry.⁷ Microporous membranes act as molecular sieves, separating gases based on molecular size. Diffusion through such membranes may occur by either Fickian or Knudsen diffusion depending on the pore size.⁸ This technology is particularly useful as hydrogen is the smallest molecule in methane steam reforming reactions. Hydrogen will be able to permeate through the membrane while the larger gas molecules in the mixed gas stream will not be able to permeate. Microporous membranes are typically constructed using amorphous silica, zeolites and carbon.

Amorphous silica membranes are porous materials produced by leaching the soluble phase from phase separated glasses.⁹ The residual silica scaffold has a range of pore sizes limiting the selectivity of these membranes. In hydrothermal environments, microporous silica membranes are prone to sintering.¹⁰ The reaction of water with silica lowers the viscosity of the glass at

operating temperatures. The consequence of this reaction is the closing of the pores during operation. Alternative methods for forming microporous silica membranes include sol-gel techniques, chemical vapor deposition methods and combinations of some or all methods.¹¹⁻¹³ Sol-gel and CVD methods are prone to additional drawbacks during the processing of the membranes. While the sol-gel technique is simple, the processing of the membranes is not very reproducible.¹⁴ The CVD method is costly and requires controlled conditions of deposition.¹⁵

Zeolites are framework silicate or aluminosilicates that have large, cage-like structures. The regular three-dimensional pores inherent in zeolites are not prone to hydrothermal sintering because the porosity is an inherent part of the crystalline structure – hydrothermal synthesis is the most commonly used route to the formation of zeolites.¹⁶ However, researchers have been unsuccessful in forming oriented zeolite layers with few defects.⁶ The orientation of the zeolite layers is necessary because the permeability through the crystal depends on the crystallographic direction. As is the case for sol-gel and CVD derived silica membranes, the processing of zeolites presents the largest hurdle toward the commercialization of these membranes. Non-zeolitic pores (intercrystalline pores) are pinholes in the membrane formed during processing. These defects limit the sieving function of the membrane by allowing contaminant gases to permeate through the zeolite layer.¹⁵

Microporous carbon membranes are prepared by carbonizing polymers at high temperatures under controlled conditions. The membranes are inexpensive and highly selective, however, permeation rates are too low.¹⁵ Lastly, carbon membranes become deactivated by the adsorption of hydrocarbons obstructing the passage of smaller molecules.¹⁷

Dense Inorganic Membranes

Dense inorganic membranes include solid electrolytes such as perovskites and metals such as palladium, silver and nickel. Transport of atomic hydrogen through metals occurs by dissociation of molecular hydrogen into atomic hydrogen at the surface, subsequent diffusion of interstitial atomic hydrogen, and

association at the opposing membrane surface. The instability of support substrates, an issue rarely researched, is proving to be a primary limitation for Pd membranes.⁷ The cost of Pd is shifting the focus to thinner membranes leading to cracking or flaking of Pd away from the support during thermal cycling. Other Pd membrane limitations include hydrogen embrittlement and poisoning of the membrane by the adsorption of gases that block hydrogen surface sites.

Current leading separation technologies do not meet the performance requirements or are not cost effective to be used in large-scale hydrogen energy systems. Membranes for the separation of gaseous species in methane steam reforming reactors must exhibit mechanical, chemical, and thermal stabilities at high temperature. High temperatures between 700°C and 950°C, low pressure and high steam to carbon ratios (~4) are necessary to ensure a high methane conversion.¹⁸ The three primary areas hindering the use of separation membranes in the reactors are stability, selectivity and flux. The combination of flowing mixed gases at high temperature is a highly corrosive environment making phase stability a significant challenge. A second hurdle in the processing of microporous membranes is the tradeoff between selectivity and flux. Larger pores have a lower selectivity but higher flux and vice versa; one property must be sacrificed at the expense of the other.

Novel Processing of Microporous Glass-Ceramics

The production of microporous membranes using the well-established glass-ceramic process combines the advantages of both amorphous silica and zeolites. In this process, traditional glass forming methods are employed, and the pore structure is controlled by the crystalline phases. The process involves the exposure of a glass-ceramic to a reducing atmosphere to produce a microporous membrane with evenly dispersed nickel metal colloids. A flow diagram highlighting the key processing steps for the proposed microporous glass-ceramic is shown in Figure 1.

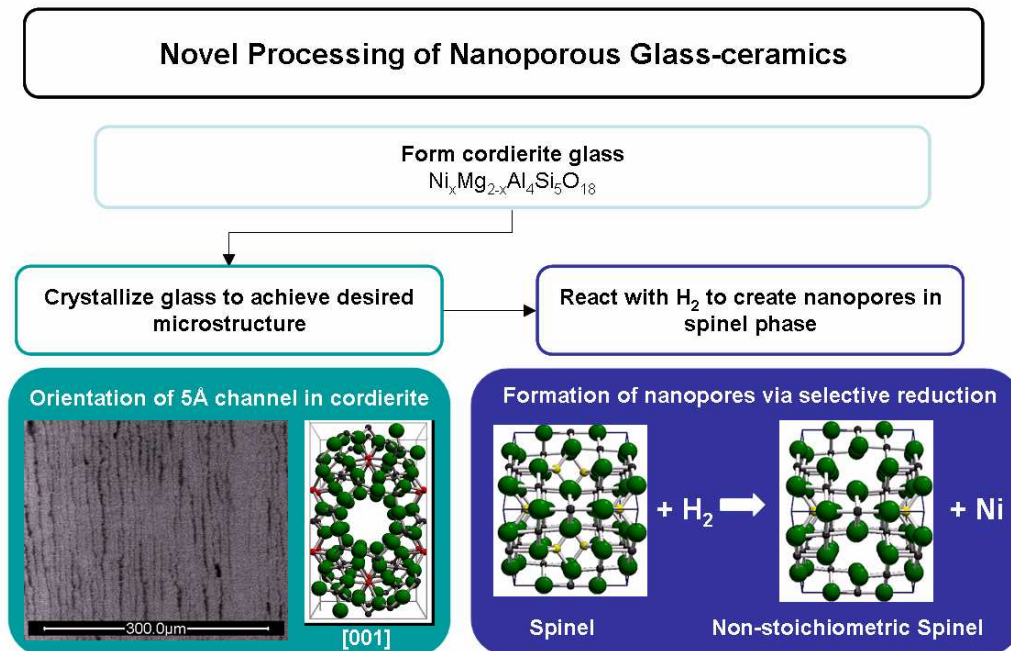


Figure 1. A flow diagram for the processing of novel microporous glass-ceramic membranes for H_2 separation.

Nickel doped aluminosilicate glasses are nucleated and crystallized to form nickel-containing aluminosilicate phases with a desired microstructure. Subsequent exposure of the glass-ceramic to a reducing atmosphere results in a hydrogen reduction reaction with nickel. Divalent nickel (Ni^{2+}) is reduced to the metallic state (Ni^0), while the Al-O-Si framework remains intact. This novel approach for controlling porosity by reducing nickel from the crystal lattice may be used to create an unlimited number of pore shapes and sizes at the nanoscale. The resulting solid with dispersed nickel metal colloids and a nanoscale pore structure may find additional application as oxide-supported catalysts in methane-steam reforming reactors.

Ni-containing Cordierite Glass-Ceramics

Nickel doped cordierite ($\text{Ni}_x\text{Mg}_{2-x}\text{Al}_4\text{Si}_5\text{O}_{18}$) glass-ceramics are candidate materials for microporous gas separation membranes. Cordierite glass-ceramics crystallize to form varying amounts of spinel and cordierite depending on the heat treatment temperature, heat treatment time and composition of the starting glass. Heat treatment of the cordierite glasses at ca. 1000°C results in cordierite

($\text{Ni}_x\text{Mg}_{2-x}\text{Al}_4\text{Si}_5\text{O}_{18}$) crystallization at the surface of the glass and spinel $\text{Ni}_x\text{Mg}_{1-x}\text{Al}_2\text{O}_4$ crystallization in the bulk.¹⁹ The resulting microstructure is outlined in Figure 1. The incorporation of nickel into both crystalline phases enables the crystal structures to be manipulated through the selective reduction reaction.

In addition to the capability of manipulating the crystal structure of Ni-doped cordierite through hydrogen reduction reactions, cordierite exhibits an inherent sieving mechanism. Cordierite exhibits about a 5 Å-wide channel formed by six corner-sharing Si-O and Al-O tetrahedra parallel to the [001] direction. This channel may serve as a diffusion pathway for the hydrogen to flow. Three projections of the orthorhombic cordierite crystal structure are shown in Figure 2. The gas permeability along the [100] and [010] directions is expected to be very low due to the dense atomic packing. The interstices and doorways are too small, requiring activated diffusion of gases through the structure. Therefore, the crystal grains must be oriented with the c-axis perpendicular to the membrane surface to maximize the flux of gas through the membrane. Surface crystallization of cordierite glass results in the spontaneous orientation of cordierite with the c-axis normal to the growth front.²⁰

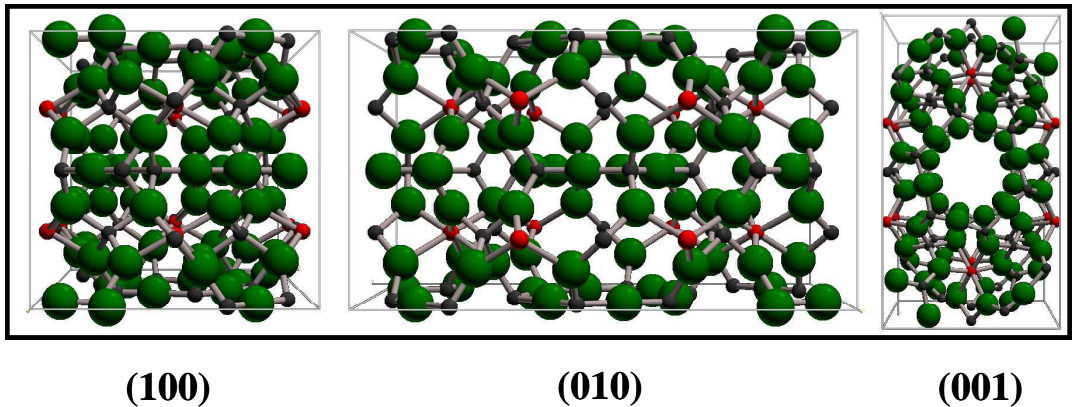


Figure 2. Projections of the orthorhombic cordierite crystal structure.

Thesis Scope

The primary focus of this thesis is the development of a microporous membrane by selectively reducing nickel from the crystalline phase of a glass-ceramic. During the course of this project, the focus shifted towards the potential for these materials to function as both the catalyst and the gas separation membrane for methane steam reforming reactors.

Three manuscripts which have been submitted to peer-reviewed journals encompass the most significant observations, and the implications of such, of the selective reduction reaction. The first manuscript focuses on the crystallization behavior of Ni-containing cordierite glass-ceramics. The second manuscript addresses the feasibility of generating pores in the spinel phase which crystallizes in the bulk of Ni-containing cordierite glasses. This manuscript is written for an audience interested in the defect structure of non-stoichiometric magnesium aluminate spinel. The third manuscript is an interpretation of the data presented in the second manuscript from the perspective of catalysis. I speculate on the use of these materials as a catalyst based on results in the existing catalyst literature.

In the appendix, the results of a simple compositional design space for NiO-MgO-Al₂O₃-SiO₂ glasses are presented. The intent of this study is to determine the effect of NiO-MgO, Al₂O₃ and SiO₂ on the glass viscosity and the crystallization behavior. Additionally, the development of an apparatus for measuring the gas permeability through plates at high temperatures is presented.

References

1. J. Conti, "Emissions of Greenhouse Gases in the United States 2004" (2005) Energy Information Administration. Accessed on: November, 2008. Available at <http://tonto.eia.doe.gov/FTP/ROOT/environment/057304.pdf>
2. "Hydrogen from Coal Program: Research, Development and Demonstration Plan" (2007) Department of Energy: Office of Fossil Energy. Accessed on: November, 2008. Available at http://www.netl.doe.gov/technologies/hydrogen_clean_fuels/refshelf/pubs/External_H2_from_Coal_RDD_Plan_September_13.pdf
3. T. E. Drennen and J. E. Rosthal, *Pathways to a Hydrogen Future*; p. 304. Elsevier, Amsterdam, 2007.
4. R. H. Jones and G. J. Thomas, *Materials for the Hydrogen Economy*; p. 352. CRC Press, Boca Raton, FL, 2007.
5. M. Dresselhaus, G. Crabtree, M. Buchanan, T. Mallouk, L. Mets, and K. Taylor, "Basic Research Needs for the Hydrogen Economy" (2004) U.S. Department of Energy. Accessed on: November, 2008. Available at http://www.sc.doe.gov/bes/reports/files/NHE_rpt.pdf
6. H. A. Meinema, R. W. J. Dirrix, H. W. Brinkman, T. A. Terpstra, J. Jekerle, and P. H. Kusters, "Ceramic Membranes for Gas Separation - Recent Developments and State of the Art," *Interceram*, **54** [2] 86-91 (2005).
7. R. Bredesen, K. Jordal, and O. Bolland, "High-Temperature Membranes in Power Generation with CO₂ Capture," *Chem. Eng. Process.*, **43** [9] 1129-58 (2004).
8. J. E. Shelby, *Gas Diffusion in Solids and Melts*. ASM International, Materials Park. OH, 1996.
9. C. E. Lord, "Alkali Borosilicate Glasses as Precursors for Nanoporous Membranes"; Ph.D. Thesis. Alfred University, Alfred, 1998.
10. V. Boffa, D. H. A. Blank, and J. E. ten Elshof, "Hydrothermal Stability of Microporous Silica and Niobia-Silica Membranes," *J. Membr. Sci.*, **319** [1-2] 256-63 (2008).
11. A. K. Prabhu and S. T. Oyama, "Highly Hydrogen Selective Ceramic Membranes: Application to the Transformation of Greenhouse Gases," *J. Membr. Sci.*, **176** [2] 233-48 (2000).
12. M. Nomura, H. Aida, S. Gopalakrishnan, T. Sugawara, S.-I. Nakao, S. Yamazaki, T. Inada, and Y. Iwamoto, "Steam Stability of a Silica

Membrane Prepared by Counterdiffusion Chemical Vapor Deposition," *Desalination*, **193** [1-3] 1-7 (2006).

13. S. Nakao, T. Suzuki, T. Sugawara, T. Tsuru, and S. Kimura, "Preparation of Microporous Membranes by TEOS/O₃ CVD in the Opposing Reactants Geometry," *Microporous and Mesoporous Mater.*, **37** [1-2] 145-52 (2000).
14. C.-Y. Tsai, S.-Y. Tam, Y. Lu, and C. J. Brinker, "Dual-Layer Asymmetric Microporous Silica Membranes," *J. Membr. Sci.*, **169** [2] 255-68 (2000).
15. K. Li, *Ceramic Membranes for Separation and Reaction*; p. 306. John Wiley & Sons, West Sussex, England, 2007.
16. J. D. F. Ramsay and S. Kallus, "Zeolite Membranes," pp. 373-95 in *Recent Advances in Gas Separation by Microporous Ceramic Membranes*. Edited by N. K. Kanellopoulos. Elsevier, Amsterdam, 2000.
17. A. F. Ismail and L. I. B. David, "A Review on the Latest Development of Carbon Membranes for Gas Separation," *J. Membr. Sci.*, **193** [1] 1-18 (2001).
18. F. Joensen and J. R. Rostrup-Nielsen, "Conversion of Hydrocarbons and Alcohols for Fuel Cells," *J. Power Sources*, **105** [2] 195-201 (2002).
19. F. J. Torres and J. Alarcon, "Ni-Containing Spinel Aluminates Glass-Ceramic Materials Obtained from Cordieritic Bulk Glasses," *J. Non-Cryst. Solids*, **320** [1-3] 246-54 (2003).
20. N. Diaz-Mora, E. D. Zanotto, R. Hergt, and R. Muller, "Surface Crystallization and Texture in Cordierite Glasses," *J. Non-Cryst. Solids*, **273** 81-93 (2000).

Chapter 1: Stoichiometric Nickel Cordierite Glass-Ceramics

1.1 Abstract

The effect of nickel on both the crystallization behavior and properties of $x\text{NiO} (1-x)\text{MgO} \cdot 2\text{Al}_2\text{O}_3 \cdot 5\text{SiO}_2$ glasses is studied. A minimum in the softening temperature is attained for $x=0.75$ and $x=1.0$ indicating that glass-in-glass phase separation occurs for glasses with nickel contents where $x \geq 0.75$. The effect of nickel on the crystallization temperature of β -quartz is related to the occurrence of phase separation. The temperature at which β -quartz transforms to hexagonal cordierite increases with increasing amounts of nickel. The incorporation of nickel in hexagonal cordierite reduces the anisotropy in the coefficient of thermal expansion. For $x \geq 0.5$, $\text{Ni}_x\text{Mg}_{1-x}\text{Al}_2\text{O}_4$ spinel crystallizes in the bulk of the glass. The spinel composition is calculated from its lattice parameter. The composition is dependent on the initial glass composition and the spinel crystallization temperature. Glasses treated at their respective spinel crystallization temperatures have a Ni/Mg ratio that is equal to the Ni/Mg ratio in the starting glass composition.

1.2 Introduction

The application of Ni-containing cordierite glass-ceramics in methane steam reforming reactors is desirable. The materials in methane steam reforming reactors must be able to withstand highly aggressive environments (CH_4 , H_2O , CO_2 , CO , and H_2) at temperatures in excess of 800°C depending on the catalyst employed.¹

Cordierite ceramics and glass-ceramics are widely used in high temperature applications such as diesel particulate filters and heat regenerators.^{2,3} Cordierite has an excellent resistance to thermal shock owing to its very low coefficient of thermal expansion in polycrystalline form. Cordierite glass-ceramics exhibit a desirable combination of excellent thermal and chemical stabilities.⁴

The substitution of Mg^{2+} with Ni^{2+} in cordierite glass-ceramics lowers the thermal stability of the cordierite phase.⁵ Additionally, the incorporation of Ni^{2+} changes the crystallization behavior of these glasses to crystallize a spinel phase in the bulk of the glass.^{6,7} The crystallization of spinel in these glasses results in a stiff, strong glass-ceramic with a very fine microstructure.⁸ The composition of the spinel solid solution in nickel aluminosilicate glass-ceramics is dependent on the starting glass composition. $[\text{Ni},\text{Mg}]\text{Al}_2\text{O}_4$ spinels are employed as the oxide support for catalysts in methane steam reforming reactions.^{9,10} The individual application of both cordierite and spinel in highly aggressive conditions makes these glass-ceramics candidates for use in methane steam reforming reactors.

This study investigates the effect of Ni^{2+} in $x\text{NiO} (1-x)\text{MgO} 2\text{Al}_2\text{O}_3 5\text{SiO}_2$ glasses on the crystallization sequence, the kinetics of β -quartz crystallization and β -quartz to cordierite transformation, and the coefficient of thermal expansion of Ni-containing cordierite. Knowledge of the weight fractions of the phases in these glass-ceramics, and the composition of the spinel phase are also of interest.

1.3 Experimental procedure

1.3.1 Kinetics study (DTA and HTXRD measurements)

The samples used in the kinetics study were prepared by dissolving/suspending the raw materials in a sol followed by precipitating the cations from solution. This method was used to ensure excellent homogeneity of the batch prior to melting. The batch components were $\text{Al}(\text{NO}_3)_3 \cdot 9\text{H}_2\text{O}$, $\text{Mg}(\text{OH})_2$, NiCO_3 , and fumed amorphous SiO_2 . The $\text{Al}(\text{NO}_3)_3 \cdot 9\text{H}_2\text{O}$ was dissolved in 75 mL of DI water followed by the addition of $\text{Mg}(\text{OH})_2$, NiCO_3 and SiO_2 . An additional 75 mL of DI water was added to completely dissolve/suspend the batch. The suspension was mixed on a hot plate using a titanium ultrasonic probe until 100 mL of solution remained. The suspension was then added to 50 mL of 1.0N NH_4OH using a peristaltic pump at a rate of about 2 drops/second. The precipitated solution was dried in an oven set at 110°C overnight. The batch was further dried in an Al_2O_3 crucible prior to melting at a heating rate of 2 K/min to 1000°C. Batches were reacted in a Pt crucible at 1600°C for 4 hrs and quenched into DI water. The glasses were crushed and sieved to < 106 microns prior to ball milling in DI water with alumina media for 24 hrs. The ball milled batch was dried at 90°C for 12 hours.

Kinetics measurements were recorded using a custom high temperature X-ray diffractometer.¹¹ Powder glass samples were mounted onto polycrystalline alumina sample holders. The glasses were heated at 60 K/min to the target temperature. Scans were recorded from 28 to 32 °2θ with collection times ranging from 45 to 85 seconds. The diffraction furnace temperature was calibrated using common phase transformation standards.

1.3.2 Glass properties study (dilatometer measurements only)

Ni-containing stoichiometric cordierite glasses, $x\text{NiO} (1-x)\text{MgO} 2\text{Al}_2\text{O}_3 5\text{SiO}_2$ with $x=0.0, 0.25, 0.50, 0.75$ and 1.0, were batched from reagent grade $\text{Mg}(\text{OH})_2$, NiO , Al_2O_3 and SiO_2 . One hundred gram batches were mixed in deionized water and dried prior to melting. The dried batches were reacted at

1600°C for 4 hrs in a Pt crucible. The melts were poured into a 1" diameter cylindrical graphite mold. The samples were annealed at 750°C for 1 hr and cooled at 3 K/min to room temperature. The NiO MgO 2Al₂O₃ 5SiO₂ sample prepared using this method was used for the kinetics study. This method of preparation was used for this sample because the β-quartz to cordierite transformation was inhibited. Presumably, contamination from the titanium ultrasonic probe prevented this transformation. The authors have observed this behavior in stoichiometric cordierite glasses intentionally doped with titania (not reported).

Thermal expansion measurements were recorded using a double push rod silica dilatometer at a heating rate of 4 K/min from room temperature to 900°C. Dilatometer measurements were repeated three times for each composition using three separate rods from the same melt.

Differential thermal analysis measurements were recorded using a DuPont 1600 DTA in static air. Samples were contained in alumina pans and alumina powder was used as the reference material. The sample sizes ranged from 20 to 35 mg.

1.4 Results

1.4.1 Glass properties

The glass transition temperature (T_g), dilatometric softening temperature (T_d), and coefficient of thermal expansion (CTE) for the Ni-containing cordierite glasses are reported in Table I. Both T_g and T_d decrease as increasing amounts of Ni²⁺ are substituted for Mg²⁺ in the cordierite glasses. The glass transition temperature decreases from 816±3°C to 796±1°C over the compositional range from 2MgO 2Al₂O₃ 5SiO₂ to NiO MgO 2Al₂O₃ 5SiO₂, respectively. The softening temperature decreases ~ 25 °C from 855±4 °C to 830±4 °C over the same compositional range. The effect of Ni²⁺ on the T_g and T_d of stoichiometric cordierite glasses does not carry over to the CTE behavior. The Mg-cordierite glass has the lowest CTE between 200°C and 600°C of 3.7 ppm/K. The

substitution of Ni^{2+} for Mg^{2+} increases the CTE of the glass only slightly to 4.0 ppm/K for all compositions containing nickel ($x \geq 0.25$).

1.4.2 Crystallization

A series of differential thermal analysis (DTA) curves for $x\text{NiO} (2-x)\text{MgO} 2\text{Al}_2\text{O}_3 5\text{SiO}_2$ glasses where $0 \leq x \leq 1$ are shown in Figure 1. All compositions exhibit an exotherm between 960°C and 990°C , which corresponds to β -quartz crystallization. The crystallization of β -quartz only occurs at the surface of the glass for all compositions. The crystallization temperature for β -quartz varies with the amount of Ni^{2+} in the initial glass composition. This trend does not vary systematically over the compositional range from $2\text{MgO} 2\text{Al}_2\text{O}_3 5\text{SiO}_2$ to $\text{NiO} \text{MgO} 2\text{Al}_2\text{O}_3 5\text{SiO}_2$. A minimum in the β -quartz crystallization temperature occurs between $x=0.0$ and $x=0.50$. Initially, the substitution of Ni^{2+} for Mg^{2+} where $x=0.25$ results in a lowering of the crystallization temperature. However, this temperature increases with Ni^{2+} additions from $x=0.25$ to $x=0.50$. For $0.5 \geq x \geq 1.0$, increasing amounts of Ni^{2+} incrementally lowers the β -quartz crystallization temperature from $985 \pm 1^\circ\text{C}$ to $962 \pm 4^\circ\text{C}$.

A second exotherm occurs for all glass compositions which corresponds to the transformation of β -quartz to cordierite. The temperature at which this transformation occurs is strongly dependent on the initial glass composition. The transformation temperature increases from $1039 \pm 3^\circ\text{C}$ to $1154 \pm 7^\circ\text{C}$ as the Ni^{2+} content increases over the compositional range from $2\text{MgO} 2\text{Al}_2\text{O}_3 5\text{SiO}_2$ to $\text{NiO} \text{MgO} 2\text{Al}_2\text{O}_3 5\text{SiO}_2$.

A third exotherm is evident in the DTA curves for the Ni-containing glasses. This exotherm corresponds to the crystallization of a spinel phase in the bulk of the glass. The exotherm for the β -quartz to cordierite transformation occurring at 1063°C for $x=0.25$ is asymmetrical with an apparent shoulder forming on the low temperature side of this peak. This shoulder may be attributed to the spinel phase crystallizing in the bulk. The presence of this exotherm becomes more evident as the Ni content in the glass increases. For $x=0.50$, the exotherms for spinel crystallization and the β -quartz to cordierite

transformation overlap (seen as a doublet centered near 1080°C). However, the presence of spinel is not detected in the XRD patterns for $x=0.25$ and $x=0.50$ crystallized at 1050°C for 100 hrs. A complete separation of these exothermic processes is clearly distinguished for the glass composition where $x=0.75$. Though a third exotherm is not observed in the DTA data recorded at 20 K/min for $x=1.0$, the presence is resolved in the DTA data recorded at higher heating rates. A series of DTA measurements recorded for NiO MgO 2Al₂O₃ 5SiO₂ glass at various heating rates is shown in Figure 4. The convolution of two exotherms becomes apparent as the heating rates are varied because these processes exhibit different activation energies.

A series of high temperature X-ray diffraction (HTXRD) patterns recorded at 1010°C for NiO MgO 2Al₂O₃ 5SiO₂ glass powder (shown in Figure 5) reveals the simultaneous transformation of β -quartz to cordierite and spinel crystallization. This observation verifies the second exotherm in the DTA pattern for $x=1.0$ is the convolution of two peaks – exotherms for both the β -quartz to cordierite transformation and spinel crystallization. Based on the intensities of the spinel reflections shown in Figure 5, the extent of spinel crystallization in the bulk is apparently minimal in the NiO MgO 2Al₂O₃ 5SiO₂ glass. However, the in situ diffraction data is measured on ball milled glass powder that has a very high surface to bulk ratio. Therefore, the diffraction pattern is dominated by the phase crystallizing at the surface – β -quartz and ultimately cordierite. The amount of spinel crystallizing in the bulk is greater than is revealed in the HTXRD data.

1.4.3 Transformation kinetics

1.4.3.1 Non-isothermal analysis (Kissinger method)

The Kissinger plot for β -quartz crystallization and the β -quartz to cordierite transformation is shown in Figure 6. The activation energies associated with the data represented in this plot are recorded in Table II. The activation energy for β -quartz crystallization is independent of the glass composition though the crystallization temperatures vary slightly. The activation energy for β -quartz crystallization is ~ 500 kJ/mol for all compositions.

The calculated activation energies required for the β -quartz to cordierite transformation in the stoichiometric cordierite glasses are very high. As Ni^{2+} is substituted for Mg^{2+} , this energy increases significantly from 620 kJ/mol to values in excess of 1000 kJ/mol for some Ni-containing compositions, though the activation energies determined for $x=0.25$ and $x=1.0$ both have significant error. This error is caused by the overlapping exotherm corresponding to spinel crystallizing in the bulk. For $x=0.50$ and $x=0.75$, the exotherms are more readily deconvoluted due to the larger separation between the β -quartz to cordierite transformation and spinel crystallization temperatures.

The calculated transformation kinetics determined from the non-isothermal analysis of DTA data (Kissinger method) seem unreasonably high. The overlapping peaks in the DTA data interfere with the analysis of both the spinel crystallization and the β -quartz to cordierite transformation. However, the isothermal analysis of HTXRD data is not prone to such interferences because both transformations are resolvable simultaneously through their respective diffraction lines.

1.4.3.2 Isothermal analysis (JMAK)

The integrated intensities of the (101) reflection for β -quartz and the (112) reflection for cordierite were used to determine the reaction kinetics for the β -quartz crystallization and β -quartz to cordierite transformation. An example set of HTXRD data recorded for the JMAK analysis is shown in Figure 7a. It is observed in the HTXRD data that the glass fully crystallizes to β -quartz before the transformation to cordierite begins. A plot of the integrated intensities for the β -quartz and cordierite reflections versus time reflects this behavior (Figure 7b). In this figure, the β -quartz was crystallized at 942°C and subsequently transformed to cordierite at 1043°C.

The induction times, reaction rates, and reaction mechanisms for both the crystallization of β -quartz and the subsequent transformation to cordierite are reported in Table III. The induction time for β -quartz crystallization decreases with increasing Ni content at a given temperature. The opposite relationship is

observed for the β -quartz to cordierite transformation. The effect of Ni^{2+} is to suppress the transformation. A dramatic increase in induction time is observed as the Ni^{2+} content increases in the initial glass composition. The reaction rates for β -quartz crystallization and β -quartz to cordierite transformation follow the same compositional dependence as their respective transformation temperature. A local maximum in the reaction rate for β -quartz crystallization is observed between $0 \leq x \leq 0.5$. For $x \geq 0.5$, the reaction rate increases incrementally with increasing Ni^{2+} content. The reaction rate for the cordierite transformation decreases with increasing Ni^{2+} content at a given reaction temperature. The reaction mechanism or Avrami parameter is determined to be $\sim 1.4 - 1.5$ for both the β -quartz crystallization and the transformation of β -quartz to cordierite for all temperatures.

The Arrhenius plot used to calculate the activation energies for β -quartz crystallization determined from the JMAK analysis of HTXRD data is shown in Figure 8. The activation energy for β -quartz crystallization is ca. 600 kJ/mol for all compositions over the temperature range from 850°C to 950°C. The activation energy required to transform β -quartz to cordierite is between 800 and 850 kJ/mol for all compositions with the exception of $x=1.0$. This composition exhibits a very limited range over which the transformation to cordierite is stable. Only two sets of data were collected for $x=1.0$ to determine the activation energy. Additionally, the activation energy for the transformation to cordierite deviates from an Arrhenius behavior for $x=0.75$ and $x=1.0$ as the temperature increases. The temperature at which this deviation occurs increases with increasing amounts of Ni^{2+} in the initial glass composition.

The individual analysis of the integrated intensity of the β -quartz and cordierite diffraction lines is used to track the β -quartz to cordierite transformation. It is shown in Figure 9 that the transformation kinetics determined from the separate analysis of the β -quartz and cordierite diffraction lines are in excellent agreement for $x=1.0$.

1.4.4 Ni_xMg_{2-x}Al₄Si₅O₁₈ cordierite

The coefficient of thermal expansion for Ni-containing stoichiometric cordierite compositions is compared with Mg-cordierite in Figure 10. The expansion along the a-axis for all compositions of stoichiometric cordierite varies linearly over the temperature range from room temperature to 1000°C. The substitution of Ni²⁺ for Mg²⁺ in the indialite structure does not affect the CTE along the a-axis. However, the thermal expansion of cordierite along the c-axis is non-linear with a minimum in the expansion occurring between 650°C and 700°C for Mg₂Al₄Si₅O₁₈. The expansion along the c-axis becomes less negative as Ni²⁺ replaces Mg²⁺ in NiMgAl₄Si₅O₁₈. The overall effect of Ni²⁺ in the indialite structure is to reduce the anisotropy in the thermal expansion by decreasing the expansion (making it less negative) along the c-axis.

1.4.5 Ni_xMg_{1-x}Al₂O₄ spinel

The lattice parameters of the spinels forming in the Ni-containing cordierite glasses at 1050°C and 1100°C are reported in Table IV. The average composition of the spinel phase is determined from its lattice parameter. The glasses were crystallized for 100 hrs to develop the spinel phase and reduce the broadening in the XRD patterns. The average crystallite size of the spinel phase is only 20-30 nm following the 100 hr treatments.

The spinel lattice parameter is determined as a function of composition for Ni_xMg_{1-x}Al₂O₄ where 0 ≤ x ≤ 1 by synthesizing single phase solid solutions through the solid state reaction of raw oxides. (see Chapter 2) The linear regression for the lattice parameter as a function of composition is

$$a = (-0.036 \pm 0.001) * x + (8.0837 \pm 0.0006),$$

where *a* is the spinel lattice parameter and *x* is the fractional amount of Ni in Ni_xMg_{1-x}Al₂O₄ spinel.

The average composition of the spinel phase is dependent on both the initial glass composition and the crystallization temperature. The Ni/Mg ratio in the spinel phase is higher for glasses containing higher nickel contents. This ratio equals the ratio in the initial glass composition, for treatment temperatures

which overlap the crystallization temperature for the respective phase. This relationship is observed in $x=0.5$ treated at 1100°C and $x=1.0$ at 1050°C for 100 hrs. However, $x=1.0$ crystallizes to form a spinel phase with a lower Ni/Mg ratio at 1100°C . Treatments conducted at temperatures exceeding the spinel crystallization temperature result in a Ni/Mg ratio that differs from the initial glass composition. The residual glass content for $x=1.0$ is higher following treatment at 1100°C than 1000°C .

1.5 Discussion

1.5.1 Glass properties

Villegas and Alarcon observed that the T_g is independent of Ni^{2+} content in $\text{NiMgAl}_4\text{Si}_5\text{O}_{18}$ and $\text{Ni}_2\text{Al}_4\text{Si}_5\text{O}_{18}$ glasses.⁶ They measured a T_g of 810°C for both compositions using a DTA at a heating rate of 10 K/min. This value is in good agreement with our measured T_g for $\text{NiMgAl}_4\text{Si}_5\text{O}_{18}$ ($x=1.0$) based on dilatometry data collected at 4 K/min. This result coincides with our observations made on the effect of Ni^{2+} on the softening temperature. The softening temperature reaches a minimum value at 830°C and remains constant with increasing Ni^{2+} content for $x \geq 0.75$. This behavior may be attributed to glass-in-glass phase separation. The softening temperature is predominately controlled by the matrix phase for a droplet-in-matrix morphology. No change in softening temperature with increasing Ni^{2+} implies that the Ni^{2+} ions are concentrated in the droplet phase and the matrix composition is largely unaffected by further Ni^{2+} additions beyond $x \geq 0.75$. The droplet-in-matrix morphology for Ni-containing cordierite glasses ($x=1.0, 2.0$) observed by Villegas and Alarcon using TEM explains the effect of Ni^{2+} on both the T_g and T_d .⁶

1.5.2 Crystallization

Nickel aluminosilicate glasses crystallize to form a glass-ceramic with a very fine microstructure.⁸ Beall and Pierson have found that glasses containing at least 5 wt % NiO in the $\text{NiO-MgO-Al}_2\text{O}_3\text{-SiO}_2$ are often self-nucleating. The presence of Ni^{2+} in stoichiometric cordierite glasses induces volume crystallization of a spinel phase. Though the presence of a third exotherm in the

DTA data suggests that spinel crystallizes in all Ni-containing cordierite glasses for $x \geq 0.25$, the XRD data does not confirm this result for $x = 0.25$. Presumably, the crystallites are too small for detection using Cu $K\alpha$ radiation.

It is difficult to form $\text{NiMgAl}_4\text{Si}_5\text{O}_{18}$ because it crystallizes over a very limited temperature interval. This interval decreases with increasing Ni^{2+} content due to the increasing temperature required to transform β -quartz to cordierite along with the decreasing crystallization temperature for spinel. However, the thermal stability limit of $\text{NiMgAl}_4\text{Si}_5\text{O}_{18}$ was not observed at temperatures $< 1100^\circ\text{C}$.

1.5.3 Transformation kinetics

The reaction mechanism is determined to be ~ 1.5 for both the β -quartz and cordierite transformations for all glass compositions. This value indicates that the transformation processes are diffusion controlled with a nucleation rate of zero. However, no dimensionality of growth is implied as all shapes growing from small dimensions take on this value.¹²

The influence of nickel on the transformation temperatures for β -quartz crystallization and the transformation to cordierite is reflected in the reaction kinetics. A minimum in the β -quartz crystallization temperature corresponds to a minimum in the induction time and a maximum in the reaction rate at a given temperature. Boberski and Giess observed the same reaction rate dependence on the Ni content for cordierite glasses where $x = 0.0, 1.0, \text{ and } 2.0$. They attribute this relationship to a decreasing glass viscosity with increasing nickel content based on dilatometric data. Based on this argument, a minimum in T_g and T_d should occur between $x = 0.0$ and $x = 0.5$ to explain the dependence of the reaction kinetics on the glass viscosity. However, no minimum is observed for either of these glass properties over this compositional range. Crystallization kinetics are often related to the viscosity of the glass because ionic diffusion may be related to the glass viscosity. For the compositions studied by Boberski and Giess, the quenched glasses are phase separated with a droplet-in-matrix morphology.⁶ The kinetics of the β -quartz crystallization are affected by the glass

microstructure. The changing microstructure with increasing nickel content results in an anomalous change in the crystallization behavior. The systematic change in the cordierite transformation temperature with increasing nickel content implies that this transformation is not affected by the glass microstructure – it is dependent on the amount of nickel in the stuffed β -quartz phase.

A lower activation energy for β -quartz crystallization relative to the β -quartz to cordierite transformation is supported by the observation that the glass fully crystallizes to β -quartz prior to the β -quartz to cordierite transformation. Though the magnitudes of the activation energies differ between the non-isothermal and isothermal methods, the relationship between the activation energy and the nickel content in the glass is consistent between these methods.

For $x \geq 0.75$ the β -quartz to cordierite transformation rate deviates from an Arrhenius behavior. This deviation occurs at higher temperatures for higher nickel contents. The change in activation energy indicates that the transformation is controlled by at least two activated processes. The excellent agreement between the reaction rates for the β -quartz peak dissolution (decreasing (101) intensity) and the cordierite formation (increasing (112) intensity) shown in Figure 9 indicates that no other processes are contributing to formation of cordierite at higher temperatures. The transformation of β -quartz to cordierite is the sole process contributing to the formation of cordierite despite the decrease in activation energy with increasing temperature. These activated processes are related to the structural rearrangements associated with the β -quartz phase.

1.5.4 $\text{Ni}_x\text{Mg}_{2-x}\text{Al}_4\text{Si}_5\text{O}_{18}$ cordierite

The decrease in anisotropic thermal expansion of the cordierite phase is desirable in thermal cycling applications. A decrease in anisotropy is observed for other cordierite substitutions including Ca^{2+} , K^+ , and Cs^+ .⁴

1.5.5 $\text{Ni}_x\text{Mg}_{1-x}\text{Al}_2\text{O}_4$ spinel

A difference in the Ni/Mg ratios between the spinel and initial glass composition is accompanied with a high residual glass content. The residual

glass likely contains a significant amount of nickel because the Ni/Mg ratio in the spinel phase is lower than the initial glass composition.

1.6 Conclusions

The substitution of nickel for magnesium in stoichiometric cordierite glasses changes the crystallization behavior. The crystallization of a spinel phase in the bulk of the glass is observed for compositions having at least 6 wt % NiO. The changing glass microstructure due to phase separation affects the crystallization kinetics of β -quartz. The transformation of β -quartz to cordierite is related to the nickel content in the β -quartz structure. This transformation temperature increases with increasing nickel substituted for magnesium. The composition of the spinel phase is dependent on the treatment temperature and initial glass composition.

1.7 References

1. J. R. Rostrup-Nielsen, "Catalytic Steam Reforming," pp. 1-117 in *Catalysis: Science and Technology*, Vol. 5. Edited by J. R. Anderson and M. Boudart. Springer-Verlag, Berlin, 1984.
2. G. A. Merkel and T. Tao, Corning Incorporated, "Narrow Pore Size Distribution Cordierite Filters with Reduced Pressure Drop," U.S. 7,309,371, December 18, 2007.
3. N. Rafidi and W. Blasiak, "Thermal Performance Analysis on a Two Composite Material Honeycomb Heat Regenerators Used for HiTAC Burners," *Appl. Therm. Eng.*, **25** [17-18] 2966-82 (2005).
4. W. Holand and G. Beall, *Glass-Ceramic Technology*. The American Ceramic Society, Westerville, OH, 2002.
5. C. Boberski and E. A. Giess, "Crystallization of Nickel-Bearing Stoichiometric Cordierite Glasses," *J. Mater. Sci.*, **29** [1] 67-72 (1994).
6. M. A. Villegas and J. Alarcon, "Crystallization and Microstructural Development of Nickel-Containing Aluminosilicate Glasses with Cordierite Stoichiometry," *J. Non-Cryst. Solids*, **292** [1-3] 70-9 (2001).
7. F. J. Torres and J. Alarcon, "Ni-Containing Spinel Aluminates Glass-Ceramic Materials Obtained from Cordieritic Bulk Glasses," *J. Non-Cryst. Solids*, **320** [1-3] 246-54 (2003).
8. G. H. Beall and J. E. Pierson, Corning Incorporated, "Nickel Aluminosilicate Glass-Ceramics," U.S. 5,352,638, February 22, 1994.
9. J. Dohrup, C. J. H. Jacobsen, and C. Olsen, Haldor Topsoe A/S, "Process for Catalytical Steam Reforming of a Hydrocarbon Feedstock," U.S. 6,416,731, July 9, 2002.
10. J. Guo, H. Lou, H. Zhao, D. Chai, and X. Zheng, "Dry Reforming of Methane over Nickel Catalysts Supported on Magnesium Aluminate Spinel," *Appl. Catal. A*, **273** [1-2] 75-82 (2004).
11. S. T. Misture, "Large-Volume Atmosphere-Controlled High Temperature X-Ray Diffraction Furnace," *Meas. Sci. Technol.*, **14** [7] 1091-8 (2003).
12. J. W. Christian, *The Theory of Transformations in Metals and Alloys*, Vol. 7; p. 975. Edited by G. V. Raynor. Pergamon Press, New York, 1965.

1.8 Tables

Table I. CTE, T_g , and T_d for β -quartz, Cordierite and Spinel in $x\text{NiO} (2-x)\text{MgO} 2\text{Al}_2\text{O}_3 5\text{SiO}_2$ Glasses

X	CTE (ppm/K) (200-600) $^\circ\text{C}$	T_g ($^\circ\text{C}$)	T_d ($^\circ\text{C}$)	Crystallization Temperatures ($^\circ\text{C}$)		
				β -quartz	Cordierite	Spinel
0	3.74 \pm 0.07	816 \pm 3	855 \pm 4	987 \pm 3	1039 \pm 3	- \pm -
0.25	4.05 \pm 0.08	813 \pm 3	850 \pm 5	972 \pm 2	1053 \pm #	- \pm -
0.5	4.00 \pm 0.06	809 \pm 5	840 \pm 5	985 \pm 1	1074 \pm 1	1091 \pm 2
0.75	4.06 \pm 0.07	802 \pm 2	831 \pm 6	976 \pm 2	1108 \pm 5	1162 \pm 2
1	4.05 \pm 0.13	796 \pm 1	830 \pm 4	961 \pm 3	1154 \pm 7	1162 \pm 4

Table II. Activation Energies for β -quartz Crystallization and β -quartz to Cordierite Transformation in $x\text{NiO} (2-x)\text{MgO} 2\text{Al}_2\text{O}_3 5\text{SiO}_2$ Glasses

DTA - Kissinger			HTXRD - JMAK		
X	β -quartz	Cordierite	X	β -quartz	Cordierite
0	464 \pm 11	622 \pm 24	0	572 \pm 38	803 \pm 60
0.25	495 \pm 12	1071 \pm 110	0.25	591 \pm 29	852 \pm 37
0.5	487 \pm 20	822 \pm 68	0.5	562 \pm 21	1004 \pm 117
0.75	483 \pm 10	1021 \pm 65	0.75	582 \pm 58	845 \pm 51
1.0*	509 \pm 40	1089 \pm 150	1.0*	629 \pm 36	696 \pm -

Table III. JMAK Parameters for β -quartz Crystallization and β -quartz to Cordierite Transformation in $x\text{NiO} (2-x)\text{MgO} 2\text{Al}_2\text{O}_3 5\text{SiO}_2$ Glasses

β-quartz crystallization for $x\text{NiO} (2-x)\text{MgO} 2\text{Al}_2\text{O}_3 5\text{SiO}_2$ glasses															
T (°C)	X=0.0			X=0.25			X=0.50			X=0.75			X=1.0*		
	t_0 (s)	ln k	n	t_0 (s)	ln k	n	t_0 (s)	ln k	n	t_0 (s)	ln k	n	t_0 (s)	ln k	n
841				15383	-10.23	1.40	21600	-10.22	1.40						
862	11537	-9.77	1.40	4611	-9.06	1.40				395	-9.41	1.50	422	-8.47	1.48
882	3932	-8.31	1.40	910	-8.03	1.50	1851	-8.40	1.40	364	-8.29	1.50	334	-7.27	1.48
902	1228	-7.56	1.40	458	-6.46	1.50	571	-7.10	1.50	530	-7.88	0.90	132	-6.36	1.52
922	397	-6.34	1.50	166	-5.62	1.40	204	-6.21	1.50	121	-6.19	1.50	51	-4.99	0.68
933				147	-5.56	1.40									
943	202	-5.71	1.40	95	-4.97	1.40	73	-5.21	1.50	25	-5.30	1.50			
950	163	-5.88	1.30												
β-quartz \rightarrow cordierite transformation for $x\text{NiO} (2-x)\text{MgO} 2\text{Al}_2\text{O}_3 5\text{SiO}_2$ glasses															
T (°C)	X=0.0			X=0.25			X=0.50			X=0.75			X=1.0*		
	t_0 (s)	ln k	n	t_0 (s)	ln k	n	t_0 (s)	ln k	n	t_0 (s)	ln k	n	t_0 (s)	ln k	n
930	9106	-9.98	1.50												
950	3750	-8.07	1.40	12056	-9.86	1.50									
969	1250	-7.00	1.47	4343	-8.59	1.40									
989	499	-5.94	1.44	1120	-7.21	1.40									
999				561	-6.43	1.40									
1003							4876	-8.45	1.16	4225	-9.04	1.56			
1008	132	-4.95	1.40												
1018				211	-5.55	1.40									
1023							572	-6.50	1.59	1473	-7.87	1.44	685	-7.02	1.37
1043							99	-4.99	1.44	617	-6.81	1.50	200	-6.03	1.49
1053										255	-5.96	1.41	164	-5.96	1.47
1064							18	-4.18	1.37						
1074										117	-5.14	1.60			
1094										70	-4.88	1.46			

Table IV. Lattice Parameters for the Spinel Phase Crystallizing in $x\text{NiO} (2-x)\text{MgO} 2\text{Al}_2\text{O}_3 5\text{SiO}_2$ Glasses

$\text{Ni}_x\text{Mg}_{2-x}\text{Al}_4\text{Si}_5\text{O}_{18}$		$\text{Ni}_x\text{Mg}_{1-x}\text{Al}_2\text{O}_4$ 1050°C, 100 hrs		$\text{Ni}_x\text{Mg}_{1-x}\text{Al}_2\text{O}_4$ 1100°C, 100 hrs		
x	Ni/Mg	Lattice Parameter		Ni/Mg	Lattice Parameter	
0.5	0.25	-	±	-	8.0742 ± 0.0010	0.24
0.75	0.375	8.0747 ± 0.0008		0.23	8.0732 ± 0.0006	0.27
1.0*	0.5	8.0647 ± 0.0008		0.51	8.07 ± 0.0006	0.36

1.9 Figures

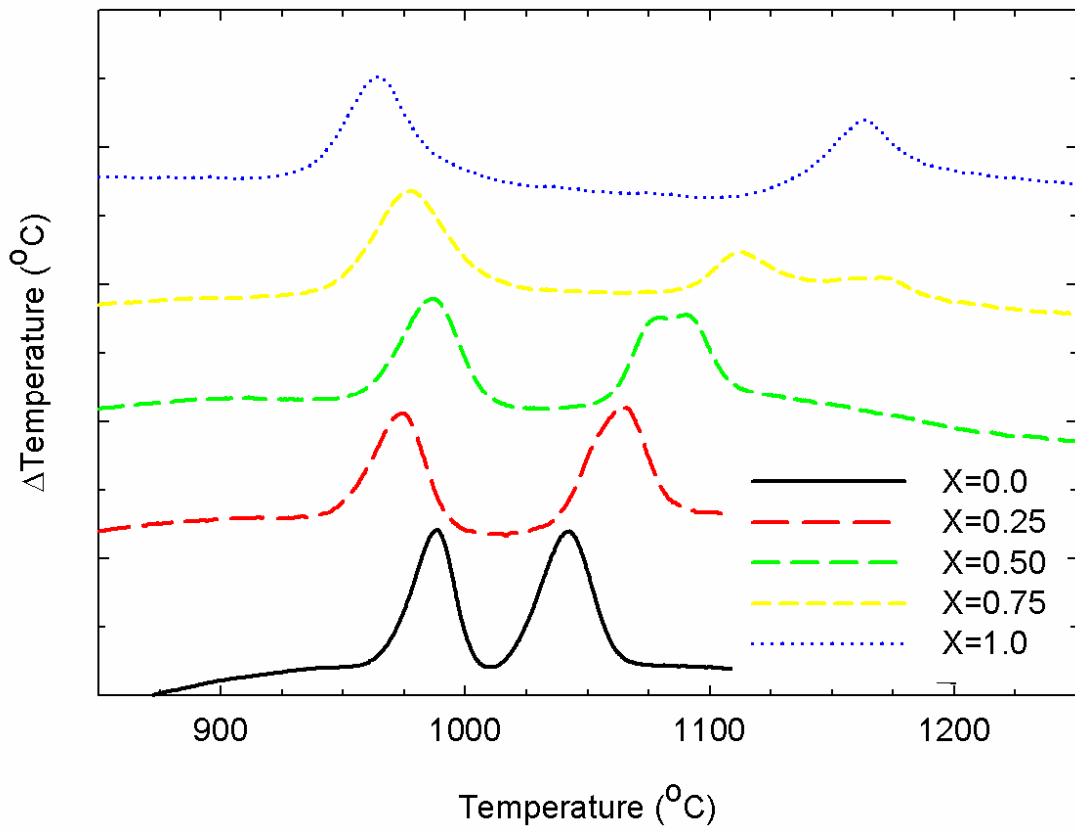


Figure 3. A DTA plot of $x\text{NiO} (2-x)\text{MgO} 2\text{Al}_2\text{O}_3 5\text{SiO}_2$ glasses showing the crystallization behavior as a function of nickel content.

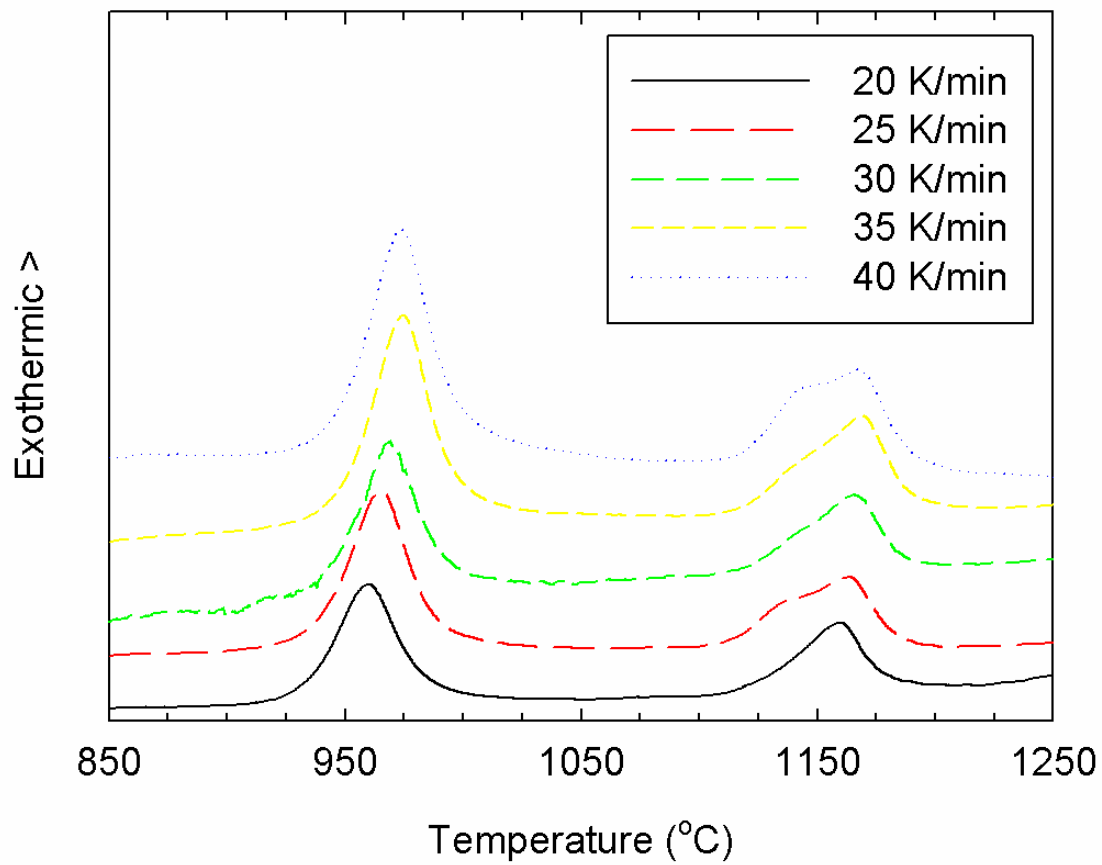


Figure 4. DTA data for NiO MgO 2Al₂O₃ 5SiO₂ glass collected at various heating rates.

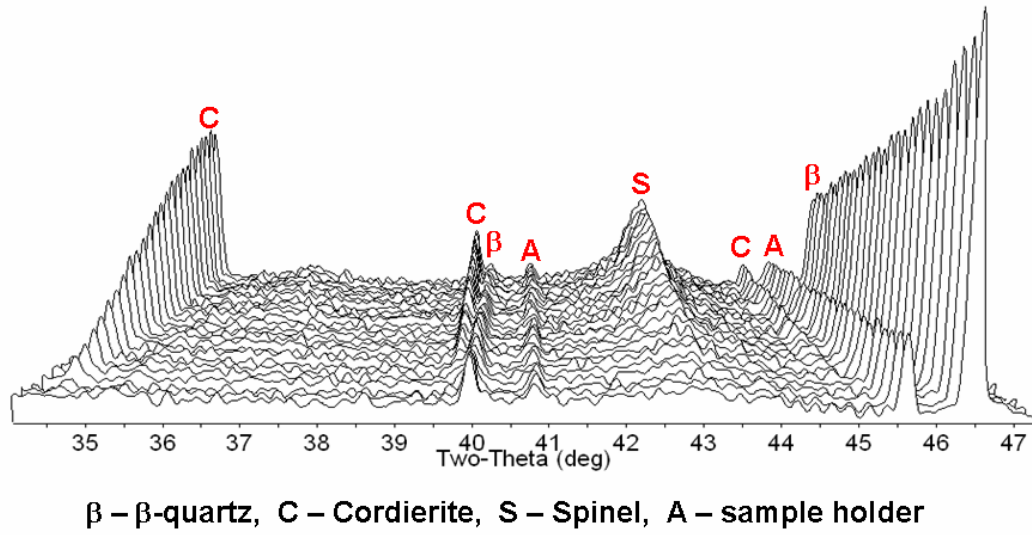


Figure 5. A series of HTXRD patterns collected in 1200 second intervals at 1010°C showing the crystallization of NiO MgO 2Al₂O₃ 5SiO₂ glass.

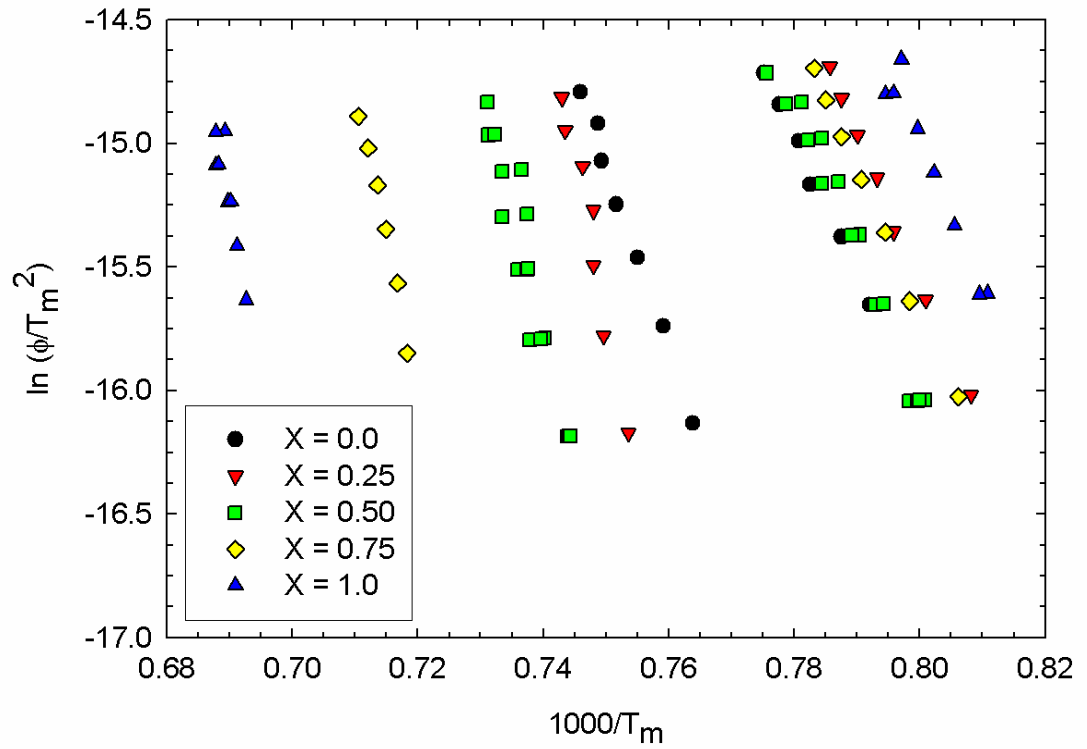


Figure 6. A Kissinger plot for β -quartz crystallization and the β -quartz to cordierite transformation in $x\text{NiO} (2-x)\text{MgO} 2\text{Al}_2\text{O}_3 5\text{SiO}_2$ glasses determined using DTA.

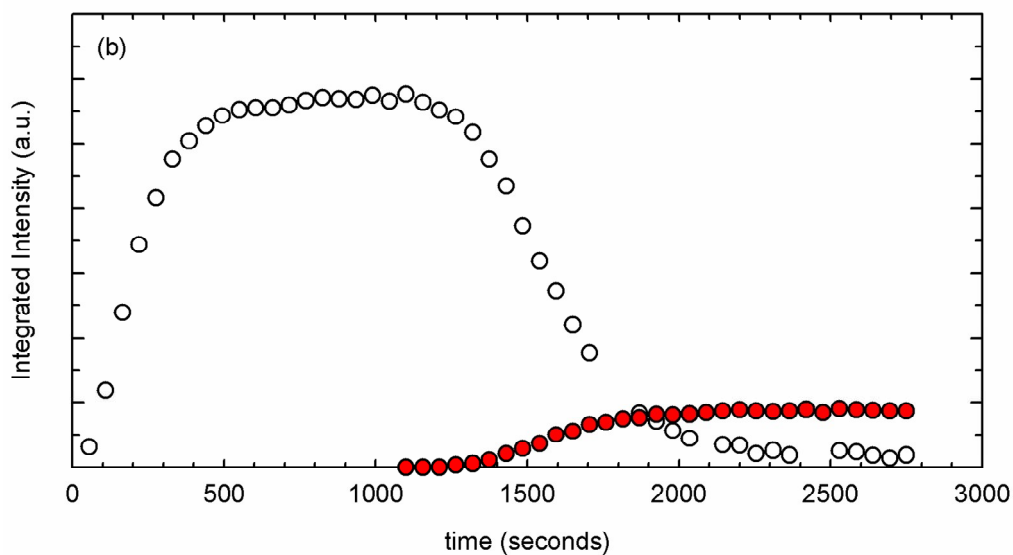
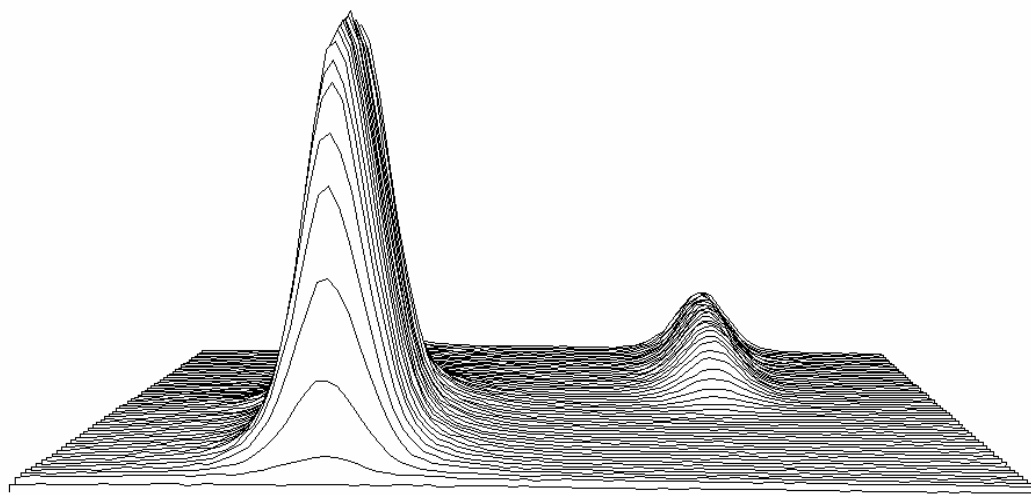


Figure 7. (a) The series of HTXRD patterns for the $0.75\text{NiO} \cdot 1.25\text{MgO} \cdot 2\text{Al}_2\text{O}_3 \cdot 5\text{SiO}_2$ glass heated at 942°C to crystallize β -quartz followed by heating to 1043°C to transform β -quartz to cordierite, and (b) the corresponding integrated intensities of the (101) and (112) diffraction lines for β -quartz and cordierite, respectively, are plotted as a function of time.

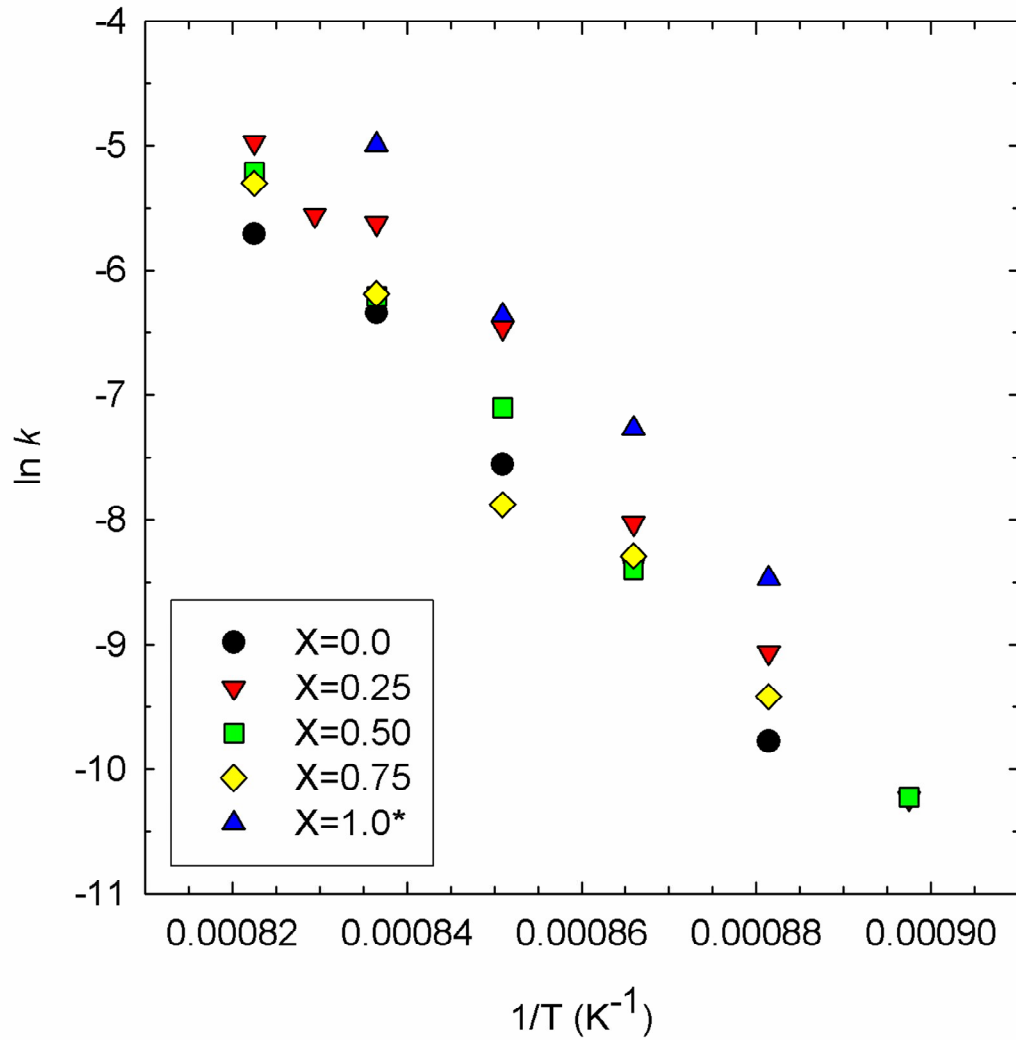


Figure 8. JMAK plot for β -quartz crystallization in $x\text{NiO} (2-x)\text{MgO} 2\text{Al}_2\text{O}_3 5\text{SiO}_2$ glasses determined using HTXRD.

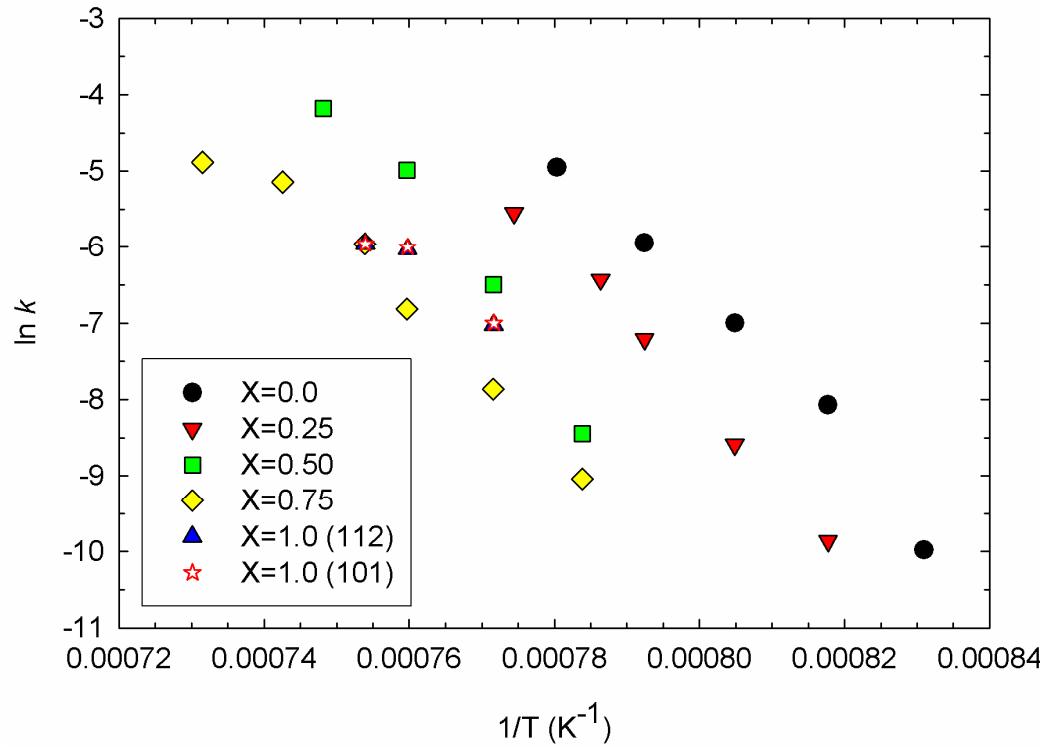


Figure 9. JMAK plot for cordierite crystallization in $x\text{NiO} (2-x)\text{MgO} 2\text{Al}_2\text{O}_3 5\text{SiO}_2$ glasses determined using HTXRD. This data is based on the analysis of the (112) cordierite diffraction line unless otherwise noted as the (101) β -quartz diffraction line.

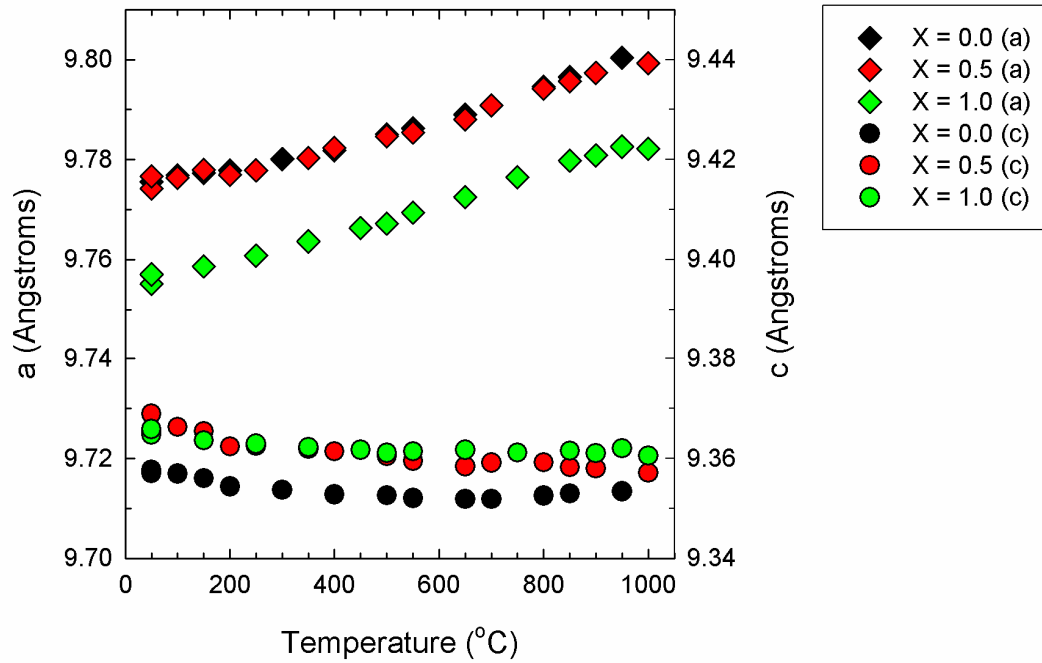


Figure 10. The effect of Ni^{2+} substituted for Mg^{2+} on the axial expansion in $\text{Ni}_x\text{Mg}_{2-x}\text{Al}_4\text{Si}_5\text{O}_{18}$ cordierite.

Justification of single phase $\text{Ni}_x\text{Mg}_{1-x}\text{Al}_2\text{O}_4$ spinel studies

A high temperature X-ray diffraction (HTXRD) pattern for $\text{NiO MgO } 2\text{Al}_2\text{O}_3$ 5SiO_2 glass-ceramic reacted with H_2 at 950°C is shown in Figure 11. The formation of metallic nickel and desorption of spinel occur simultaneously during the reaction with hydrogen. This observation suggests that the metallic nickel is reduced from the spinel phase. However, nickel may be incorporated into all of the individual phases of this multiphase glass-ceramic – β -quartz (not shown), cordierite, spinel, and the residual glass. To simplify the analysis, single phase $[\text{Ni,Mg}]\text{Al}_2\text{O}_4$ solid solutions were synthesized and reacted with hydrogen to determine the feasibility of creating nanopores in the spinel phase while maintaining the stability of the framework.

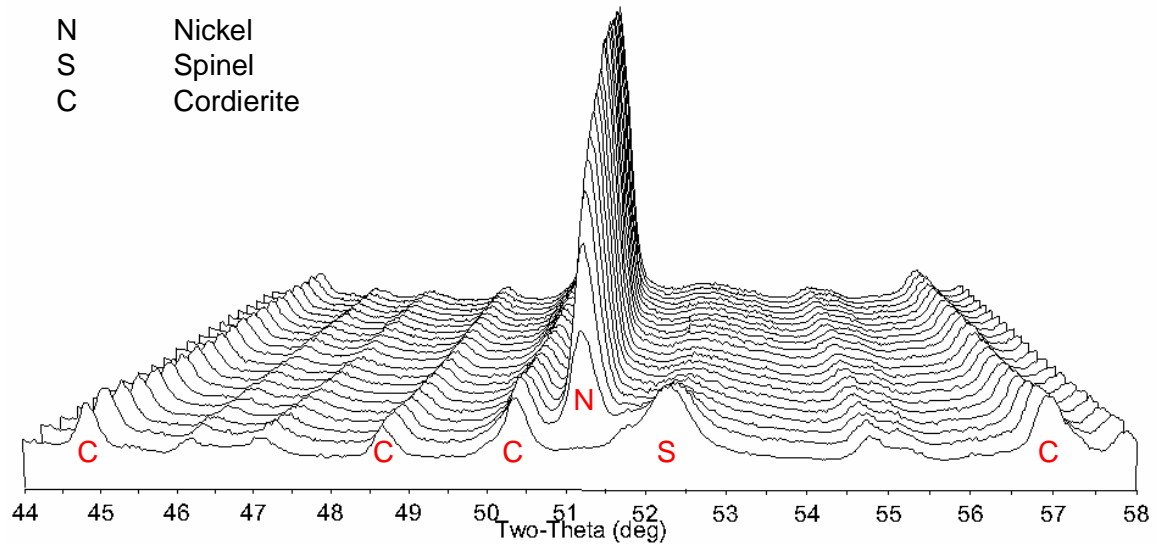


Figure 11. HTXRD pattern for $\text{NiO MgO } 2\text{Al}_2\text{O}_3$ 5SiO_2 glass-ceramic reacted with H_2 at 950°C in 1 hr intervals.

Chapter 2: Defect Structure of Alumina-rich Magnesium Aluminate Spinel

2.1 Abstract

The selective reduction of nickel from $\text{Ni}_x\text{Mg}_{1-x}\text{Al}_2\text{O}_4$ spinel through reaction with hydrogen is a novel method for determining the defect equation for alumina-rich spinel. This method enables the in situ analysis of the defect reaction as it progresses. The reaction is described by the following equation: $\text{Ni}_x\text{Mg}_{1-x}\text{Al}_2\text{O}_4 + x\text{H}_2 \rightarrow x\text{Ni}^0 + \text{Mg}_{1-x}\text{Al}_2\text{O}_{4-x} + xV_{\text{Ni}}'' + xV_{\text{O}}'' + x\text{H}_2\text{O}$. Rietveld refinement of X-ray diffraction data is used to determine: (1) the weight percents of the products, (2) the nickel occupancy in the spinel phase, and (3) the $\text{Mg}_{1-x}\text{Al}_2\text{O}_{4-x}$ lattice parameter. The weight loss during the hydrogen reaction is determined using in situ thermogravimetric analysis. The hydrogen reaction is generalized to describe the defect reaction for alumina-rich spinel: $\text{Al}_2\text{O}_3 \rightarrow V_{\text{Mg}}'' + 2\text{Al}_{\text{Al}}^x + 3\text{O}_{\text{O}}^x + V_{\text{O}}''$. Application of this defect equation to $\gamma\text{-Al}_2\text{O}_3$ predicts a significantly lower number of ions per unit cell than is commonly accepted. This defect model predicts 16 Al^{3+} ions and 24 O^{2-} ions per unit cell versus the commonly accepted $64/3$ Al^{3+} ions and 32 O^{2-} ions per unit cell. We relate the large concentration of vacancies to the porous microstructure of $\gamma\text{-Al}_2\text{O}_3$.

2.2 Introduction

The products of $[\text{Ni,Mg}]\text{Al}_2\text{O}_4$ spinel reacted with hydrogen are widely studied for catalytic application in reforming reactions. The products of this reaction are metallic nickel supported on spinel. There has been little effort to characterize the spinel support following the reaction with hydrogen, though the catalyst support is known to significantly impact the performance of the catalyst. The structure of the catalyst support following reaction with hydrogen is effectively a defect spinel phase.

The defect structures of non-stoichiometric magnesium aluminate spinel and $\gamma\text{-Al}_2\text{O}_3$ have been widely debated.¹ Most studies focus on the cation disorder and cation vacancy distribution in non-stoichiometric magnesium aluminate spinel.²⁻⁴ Cation disorder or the degree of inversion refers to the distribution of the Mg^{2+} and Al^{3+} ions on the tetrahedral and octahedral sites.

Studies involving a combination of neutron diffraction and X-ray diffraction², and nuclear magnetic resonance⁴ have focused on the cation vacancy distribution in non-stoichiometric magnesium aluminate spinels. These studies rely on complex relationships which are based on structural and charge neutrality conditions to describe the cation vacancy distribution.³ The results of this study do not address the site distribution of the cation vacancies, however, the stoichiometry of the defect spinel structure is interpreted.

In this study, the defect reaction for alumina-rich spinel is determined by selectively reducing nickel from $\text{Ni}_x\text{Mg}_{1-x}\text{Al}_2\text{O}_4$ spinel through reaction with hydrogen. This method enables the in situ analysis of the defect reaction as it progresses by observing the defect species as they evolve. By progressively forming a more alumina-rich spinel as nickel is reduced from $\text{Ni}_x\text{Mg}_{1-x}\text{Al}_2\text{O}_4$ spinel the $\gamma\text{-Al}_2\text{O}_3$ structure is approached. Finally, we apply the proposed defect equation for alumina-rich spinel to the $\gamma\text{-Al}_2\text{O}_3$ structure.

2.3 Experimental procedure

The compositional series $\text{Ni}_x\text{Mg}_{1-x}\text{Al}_2\text{O}_4$, where $0 \leq x \leq 1$, was synthesized from reagent grade MgOH_2 , NiO , and Al_2O_3 . Batches were ball milled using alumina media in deionized water and subsequently dried at 90°C . Pellets were sintered at 1450°C in increments of 18 hrs until phase purity was achieved. Between sintering cycles the pellets were crushed and ground using an alumina mortar and pestle for analysis using XRD.

Heat treatments of the spinel powders were conducted at ~ 300 torr of ultra pure H_2 for various times. The heat treatment temperatures and times are recorded in Table V. The reaction times exceed the time required to completely react the spinel samples with hydrogen for the given temperature. Completion of the hydrogen reaction was determined using *in situ* HTXRD isothermal treatments in flowing $4\text{H}_2\text{-}96\text{N}_2$. The end of the reaction is determined to be the time at which the formation of additional metallic nickel ceases.

X-ray diffraction data was collected using $\text{Cu K}\alpha$ radiation in Bragg-Brentano geometry. Data was collected from $5\text{-}160^\circ 2\theta$ using a 0.03° step size and 5 second dwell time. Topas V3 was used for Rietveld refinement of the X-ray diffraction data.⁵

In situ X-ray diffraction measurements were recorded using a custom high temperature X-ray diffractometer capable of full atmosphere control.⁶ Powder samples were mounted onto polycrystalline alumina sample holders. The diffraction furnace temperature was calibrated using common phase transformation standards.

Thermogravimetric measurements were performed on 15-30 mg powder samples contained in alumina pans. Each measurement was repeated at least three times for each composition.

2.4 Results

2.4.1 $\text{Ni}_x\text{Mg}_{1-x}\text{Al}_2\text{O}_4$ spinel structure

The relationship between the spinel lattice parameter and the composition for $\text{Ni}_x\text{Mg}_{1-x}\text{Al}_2\text{O}_4$ is shown in Figure 12. The lattice parameter decreases linearly with increasing amounts of nickel over the compositional range. The data for the spinels synthesized in this study are plotted with values reported in the literature. Overall the lattice parameters are in good agreement for all compositions though there is some scatter within and between the different studies. The quench temperature or temperature at which the spinels were synthesized in the respective study is noted. The lattice parameter is higher for samples quenched from higher synthesis temperatures for a given composition.

2.4.2 H_2 reaction with $\text{Ni}_x\text{Mg}_{1-x}\text{Al}_2\text{O}_4$ spinel

2.4.2.1 *Products of the H_2 reaction*

Rietveld analysis of the XRD data for $\text{Ni}_{0.5}\text{Mg}_{0.5}\text{Al}_2\text{O}_4$ following reaction at 850°C for 24 hrs is shown in Figure 13. The only products of the reaction of $\text{Ni}_x\text{Mg}_{1-x}\text{Al}_2\text{O}_4$ spinel with H_2 are metallic nickel and spinel for $x \leq 0.50$ for all reaction temperatures between 650°C and 1000°C. The corundum phase noted in Figure 13 is contamination that occurred during ball milling prior to reaction with hydrogen. The weight percent of corundum remains constant during the reaction with hydrogen at all reaction temperatures. The Mg-O-Al framework of the spinel phase is stable following the reaction with hydrogen up to 1000°C.

2.4.2.2 *Stability of the spinel framework*

The instability of the spinel framework for $x \geq 0.75$ is marked by the formation of transition alumina polymorphs for reaction temperatures between 800°C and 1000°C. The products of NiAl_2O_4 reacted with H_2 between 800°C and 1000°C are shown in Figure 14. The products of these reactions are dependent on the reaction temperature. The formation of γ -alumina occurs at 800°C for $x=0.75$ (not shown) and $x=1.0$. Transformation of γ -alumina to θ -alumina is observed at 1000°C with increasing amounts of θ -alumina forming at longer

reaction times for $x=1.0$. No evidence of γ -alumina transitioning to θ -alumina is observed for $x=0.75$ though the appearance of weak unidentifiable diffraction lines in the XRD pattern is observed.

2.4.2.3 Quantification of phases

The amount of nickel formed during the reaction of $\text{Ni}_{0.5}\text{Mg}_{0.5}\text{Al}_2\text{O}_4$ with H_2 is shown in Figure 15 for each reaction temperature. The weight percent of nickel is normalized to the weight percent of nickel in the starting spinel composition (i.e. each data point is divided by 18.4 because there is 18.4 wt % Ni in $\text{Ni}_{0.5}\text{Mg}_{0.5}\text{Al}_2\text{O}_4$). The quantity of the products is dependent on the reaction temperature. The amount of metallic nickel formed increases at higher reaction temperatures until a maximum value is reached at 850°C. The maximum amount of metallic nickel formed is approximately the amount of nickel in $\text{Ni}_{0.5}\text{Mg}_{0.5}\text{Al}_2\text{O}_4$ prior to reaction with hydrogen.

2.4.2.4 Defect spinel structure

As noted earlier, the spinel framework remains stable following the complete reduction of nickel from $\text{Ni}_x\text{Mg}_{1-x}\text{Al}_2\text{O}_4$ for $x \leq 0.50$. The lack of additional decomposition products suggests that the spinel structure is defective with vacancies on the nickel sites.

2.4.2.5 Formation of V_{Ni}''

The site occupancy for nickel on both the tetrahedral and octahedral sites in the defect spinel structure is determined from the Rietveld refinement of X-ray diffraction data. The occupancies of all spinel sites were constrained to maintain charge neutrality by creating an equal number of nickel vacancies (V_{Ni}'') to oxygen vacancies (V_{O}''). The validity of this constraint is addressed in the following section.

The site occupancy for divalent nickel in $\text{Ni}_{0.5}\text{Mg}_{0.5}\text{Al}_2\text{O}_4$ following the complete reaction of the spinel with hydrogen at various reaction temperatures is shown in Figure 15. The site occupancy in this figure is the sum of the nickel occupancy in both the tetrahedral and octahedral sites. While there is significant

error in the structure refinement, the site occupancy decreases with increasing reaction temperature until a minimum in nickel occupancy is reached. This minimum occurs at a reaction temperature of 850°C at which point there is no remaining nickel in the spinel framework.

The creation of nickel vacancies in the spinel framework follows the same trend with increasing reaction temperature as that for the formation of metallic nickel. For reactions occurring at 850°C, both the minimum in nickel site occupancy and the maximum in metallic nickel formed is achieved. To compare these independent parameters in the Rietveld refinement both the fraction of nickel vacancies and the weight percent of metallic nickel are normalized to their respective maxima. The normalized fraction of nickel vacancies created in $\text{Ni}_{0.5}\text{Mg}_{0.5}\text{Al}_2\text{O}_4$ and normalized fraction of metallic nickel formed are shown as a function of reaction temperature in Figure 15. It is evident that the creation of nickel vacancies in spinel coincides precisely with the weight percent of metallic nickel formed over the reaction temperature range of 650°C to 1000°C. The agreement between these independent parameters validates the nickel site occupancy trend shown in Figure 15.

2.4.2.6 Formation of V_{O}''

The selective reduction of nickel from spinel results in the formation of nickel vacancies. These vacancies must be charge balanced by either the formation of hydroxyl species or oxygen vacancies. The formation of oxygen vacancies (*evolution of O_2*) will result in a measurable weight loss. The weight loss of the spinel samples during reaction with hydrogen (flowing 4H₂-96N₂) is measured *in situ* using thermogravimetric analysis (TGA). An example set of data for $\text{Ni}_{0.50}\text{Mg}_{0.50}\text{Al}_2\text{O}_4$ is shown in Figure 16. The temperature profile for the measurement is included for clarity. The weight of the sample decreases as the reaction temperature increases until a minimum weight is reached at 1000°C. The weight loss for the samples is calculated from the difference in weights recorded at 600°C and 1000°C and normalizing this difference to the value at 600°C. A plot of the experimentally determined weight loss is shown in Figure 17 for each composition. Also included in the plot is the theoretical weight loss for

each composition that is expected to occur if oxygen vacancies are created to charge balance the formation of nickel vacancies during the reaction with hydrogen. The experimental data is in good agreement with the theoretical data for all compositions. Though there is no reducible specie in MgAl_2O_4 for this set of reaction conditions, this composition loses weight during the reaction with hydrogen. The weight loss is probably due to adsorbed water.

2.4.2.7 Non-stoichiometric spinel lattice parameters

In situ diffraction data for $\text{Ni}_{0.5}\text{Mg}_{0.5}\text{Al}_2\text{O}_4$ in flowing 4H_2 - 96N_2 reacted at 800°C is shown in Figure 18. The formation of metallic nickel with increasing reaction time is observed by the increasing intensity of the nickel diffraction line relative to the intensity of the corundum peak. The spinel lattice parameter corresponding to the in situ diffraction data is plotted as a function of reaction time in Figure 18b. The spinel lattice parameter decreases as nickel is selectively reduced while maintaining the stability of the spinel framework. This is seen visually in the 3D plot (Figure 18a) as a shifting of the spinel diffraction line to higher diffraction angle.

As the amount of nickel reduced from $\text{Ni}_x\text{Mg}_{1-x}\text{Al}_2\text{O}_4$ increases the spinel phase becomes increasingly defective or non-stoichiometric. The lattice parameters for the non-stoichiometric spinels for $x \leq 0.50$ formed by selectively reducing the nickel from $\text{Ni}_x\text{Mg}_{1-x}\text{Al}_2\text{O}_4$ are plotted in Figure 19. These lattice parameters are compared with values reported in the literature for non-stoichiometric spinels synthesized through the solid state reaction of oxides. The spinels formed in this study are in good agreement with the literature values.⁷⁻⁹

2.4.3 Re-oxidation/Reverse Reactions

2.4.3.1 Quantification of phases

Non-stoichiometric spinel $\text{Mg}_{0.5}\text{Al}_2\text{O}_{3.5}$ + Ni (formed by reacting $\text{Ni}_{0.5}\text{Mg}_{0.5}\text{Al}_2\text{O}_4$ with H_2 at 1000°C for 12 hrs) is re-oxidized by reheating in air. The weight percents of phases calculated from the Rietveld refinement of XRD data at the respective re-oxidation temperature is plotted in Figure 20. The weight percent of corundum (contamination from the ball milling is withheld from

this figure for clarity). The metallic nickel begins to oxidize at 300°C to form NiO. The oxidation of the nickel is complete following reaction at 500°C for 1 hr, however, the NiO does not react with the non-stoichiometric spinel until 800°C. This reaction is seen as a decrease in the weight percent of NiO concurrent with an increase in weight percent of the spinel phase. The spinel is almost fully reacted by 1000°C with only 2 wt % NiO remaining unreacted.

2.4.3.2 Spinel lattice parameter

The change in the spinel lattice parameter during the re-oxidation reaction is shown in Figure 22. The lattice expansion in air is compared with the expansion of the lattice in flowing 4H₂-96N₂ to prevent the re-oxidation of the non-stoichiometric spinel. The expansion of the lattice is independent of the atmosphere; the expansion in air is the same as the expansion in 4H₂-96N₂. At 800°C, the expansion of the spinel lattice in air begins to increase significantly. Following reaction at 1000°C for 1 hr in air the spinel lattice parameter is slightly higher than the spinel lattice parameter for Ni_{0.5}Mg_{0.5}Al₂O₄.

2.4.3.3 Weight gain during re-oxidation

Thermogravimetric analysis is used to measure the weight of non-stoichiometric spinel Mg_{0.5}Al₂O_{3.5} + Ni (formed by reacting Ni_{0.5}Mg_{0.5}Al₂O₄ with H₂ at 1000°C for 12 hrs) during re-oxidation in air. The same temperature profile is used as is used in the in situ XRD experiment for the re-oxidation of Mg_{0.5}Al₂O_{3.5} + Ni. Both the weight of the sample and the temperature profile are plotted as a function of reaction time in Figure 21. The sample gains a significant amount of weight between 300°C and 500°C (between ~ 100 and 400 minutes). A minimal amount of weight is gained between 600°C and 1000°C corresponding to an increase in the total weight gained from 4.56 % and 4.74 %, respectively.

2.5 Discussion

2.5.1 Ni_xMg_{1-x}Al₂O₄ spinel structure

The spinel lattice collapses as nickel is substituted for magnesium in Ni_xMg_{1-x}Al₂O₄. This collapse is related to a change in the degree of inversion as

the nickel content increases. The spinel degree of inversion refers to the occupation of the divalent cation on the octahedral site. The incorporation of nickel into $\text{Ni}_x\text{Mg}_{1-x}\text{Al}_2\text{O}_4$ spinel increases the degree of inversion – nickel preferentially occupies the octahedral site, thereby, displacing the smaller aluminum ion to the tetrahedral site.^{10, 11} The smaller cation on the tetrahedral site results in a collapse of the oxygen sublattice as is evidenced by a decrease in both the lattice parameter and the oxygen positional parameter. The relationship between the degree of inversion and the oxygen positional parameter has been confirmed for the spinels synthesized in this study from the Rietveld refinement of XRD data though it is not reported.

The effect of the quench temperature on the spinel lattice parameter is related to the degree of inversion and its temperature dependence.^{10, 12} As the quench temperature increases the cation distribution becomes more random (the degree of inversion decreases). The lattice parameter is inversely related to the degree of inversion, hence, increasing quench temperature results in an increase in the spinel lattice parameter.

The $\text{Ni}_x\text{Mg}_{1-x}\text{Al}_2\text{O}_4$ spinels have varying degrees of inversion which are dependent on the nickel content. We see no evidence that the degree of inversion influences the reactivity with H_2 ; the reaction is complete by 850°C for 24 hrs for all compositions. At the reaction temperatures used in this study it is reported that changes in the cation distribution occur.^{10, 12} The ability of the cation distribution to change over this temperature range supports the observation that the hydrogen reaction is independent of the degree of inversion.

2.5.2 H_2 reaction with $\text{Ni}_x\text{Mg}_{1-x}\text{Al}_2\text{O}_4$

The reaction of $\text{Ni}_x\text{Mg}_{1-x}\text{Al}_2\text{O}_4$ with hydrogen has the same temperature dependence for all compositions. The amount of metallic nickel formed reaches a constant value at 850°C indicating that the reaction of the spinel with hydrogen is complete by 850°C for 24 hrs for all compositions. Following the complete reduction of nickel from the spinel phases for $x \leq 0.50$, the spinel Mg-O-Al framework remains stable up to 1000°C as is evidenced in the XRD patterns.

The lack of additional decomposition products indicates that the spinel framework is defective with the presence of at least nickel vacancies.

The selective removal of nickel from $\text{Ni}_x\text{Mg}_{1-x}\text{Al}_2\text{O}_4$ spinel effectively results in the formation of a non-stoichiometric spinel phase with excess alumina $\text{MgO} \cdot n\text{Al}_2\text{O}_3$. The lattice parameters for the non-stoichiometric spinel formed through the selective reduction of nickel from stoichiometric $\text{Ni}_x\text{Mg}_{1-x}\text{Al}_2\text{O}_4$ spinel are in good agreement with non-stoichiometric $\text{MgO} \cdot n\text{Al}_2\text{O}_3$ spinels synthesized through the solid state reactions.⁷⁻⁹ The lattice parameters for the non-stoichiometric spinels formed in this study are slightly higher than the literature values for $\text{MgO} \cdot n\text{Al}_2\text{O}_3$ formed via solid state reaction. This difference may be due to variations in the cation distribution between non-stoichiometric spinel samples or the presence of some residual nickel in the spinel framework.

2.5.3 Re-oxidation/Reverse Reactions

The combined results of the in situ XRD and TGA analyses reveal that nickel and oxygen ions are incorporated into the spinel structure simultaneously during the re-oxidation of the $\text{Mg}_{1-x}\text{Al}_2\text{O}_{4-x}$ spinel + Ni. This behavior mirrors the hydrogen reaction for $\text{Ni}_x\text{Mg}_{1-x}\text{Al}_2\text{O}_4$ spinel where an equal amount of nickel and oxygen vacancies form concurrently. The weight gain at temperatures $< 800^\circ\text{C}$ is only attributable to the oxidation of nickel and no evidence oxygen entering the spinel structure is observed. The expansion of the $\text{Mg}_{1-x}\text{Al}_2\text{O}_4$ spinel lattice is independent of the reaction atmosphere (air vs. $4\text{H}_2\text{-}96\text{N}_2$) between room temperature and 800°C . At temperatures $\geq 800^\circ\text{C}$, the nickel or oxygen ions are incorporated into the spinel structure seen as a rapid increase in the lattice parameter concurrent with the depletion of NiO.

The difference in the lattice parameter at 1000°C may be due to the “quench temperature”, or the fact that a little NiO still remains and the structural rearrangement associated with the NiO re-entering the spinel lattice may be contributing to a larger unit cell. See Figure 12 for effect of quench temp on lattice parameter.

2.5.4 Defect spinel structure

The spinel framework remains stable following the complete reduction of nickel from $\text{Ni}_x\text{Mg}_{1-x}\text{Al}_2\text{O}_4$ for $x \leq 0.50$. The lack of additional decomposition products suggests that the spinel structure is defective with vacancies on the nickel sites. The formation of nickel vacancies must be charge balanced by either (1) the formation of hydroxyl $[\text{OH}]^-$, or (2) the formation of oxygen vacancies. The reduction reaction for the first proposed mechanism is as follows:



In this reaction the hydrogen molecule dissociates at the reaction site forming two hydroxyl species per divalent nickel ion reduced to the atomic state. The reduction of nickel from the tetrahedral site is anticipated to result in a decrease in the spinel lattice parameter. A decrease in the spinel lattice is observed in Figure 18 as nickel vacancies are created. However, there would not be a weight loss but rather a small weight gain as hydroxyl forms unless the nickel volatilizes. The close agreement between the maximum weight percent of metallic nickel formed during the hydrogen reaction and the weight percent of nickel in the stoichiometric $\text{Ni}_x\text{Mg}_{1-x}\text{Al}_2\text{O}_4$ spinel composition does not indicate a significant loss of nickel is occurring. The observed weight loss which occurs during the hydrogen reaction does not support the proposed reaction in which hydroxyl is formed to charge compensate the formation of nickel vacancies.

The alternative proposed defect reaction which may occur during the hydrogen reaction is the creation of an equal number of oxygen vacancies to charge balance the formation of nickel vacancies. This reduction reaction is stated below:

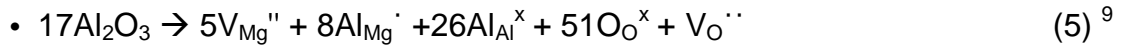


For this defect reaction, the formation of oxygen vacancies will result in a measurable weight loss. Excellent agreement between the experimental and theoretical weight loss for this defect reaction is shown in Figure 17 for all compositions. The measured weight loss is directly proportional to the number of oxygen vacancies formed and thus the number of nickel vacancies. The defect

equation for the reaction of hydrogen with $\text{Ni}_x\text{Mg}_{1-x}\text{Al}_2\text{O}_4$ can be generalized to describe the defect reaction for alumina-rich $\text{MgO } n\text{Al}_2\text{O}_3$ spinel:



Alternative defect reactions have been proposed for alumina-rich $\text{MgO } n\text{Al}_2\text{O}_3$ spinel. These reactions include:



None of these proposed defect reactions support the results in this study. Defect reactions (3) and (4) are ruled out because neither correctly account for the observed weight loss due to oxygen evolution from oxygen vacancy formation. Defect reaction (5) includes the formation of oxygen vacancies; however, this mechanism predicts a much lower weight loss than is observed.

The self diffusion of oxygen is higher in alumina-rich spinel is than in stoichiometric MgAl_2O_4 .¹⁵ This property may be explained by defect reactions (2b) and (5) which include $V_{\text{O}}^{\cdot\cdot}$ as a charge compensating specie.

2.5.5 Relating alumina-rich spinel to $\gamma\text{-Al}_2\text{O}_3$

2.5.5.1 Transition from $\text{Mg}_{1-x}\text{Al}_2\text{O}_4$ spinel to $\gamma\text{-Al}_2\text{O}_3$

The reaction of $\text{Ni}_x\text{Mg}_{1-x}\text{Al}_2\text{O}_4$ for $x \geq 0.75$ with hydrogen results in the formation of metastable transition alumina phases. The transition to $\gamma\text{-Al}_2\text{O}_3$ is continuous with increasing amounts of excess alumina (as x increases for $\text{Mg}_{1-x}\text{Al}_2\text{O}_{4-x}$). The change in the lattice parameter for non-stoichiometric spinel varies linearly as the amount of excess alumina increases. The relationship between the lattice parameter and the non-stoichiometric spinel composition is continuous with the reported lattice parameter for $\gamma\text{-Al}_2\text{O}_3$ (see Figure 19). The structure of $\gamma\text{-Al}_2\text{O}_3$ is widely disputed though it is generally agreed to be a defect spinel structure.¹ As nickel is reduced from $\text{Ni}_x\text{Mg}_{1-x}\text{Al}_2\text{O}_4$ the spinel phase becomes increasingly non-stoichiometric until ultimately transitioning to $\gamma\text{-Al}_2\text{O}_3$. The continuous transition of the alumina-rich spinels formed through the selective

reduction of nickel from $\text{Ni}_x\text{Mg}_{1-x}\text{Al}_2\text{O}_4$ offers a unique perspective into the structure of $\gamma\text{-Al}_2\text{O}_3$.

2.5.5.2 Applying the alumina-rich spinel defect equation to $\gamma\text{-Al}_2\text{O}_3$

One way of viewing the $\gamma\text{-Al}_2\text{O}_3$ structure is as an alumina-rich defect spinel for the limiting case where the MgO content approaches zero. This perspective enables us to apply the defect equations for alumina-rich spinel to describe the defect structure of $\gamma\text{-Al}_2\text{O}_3$. The structure of $\gamma\text{-Al}_2\text{O}_3$ is generally accepted to be a defect spinel structure which is described by the Fd-3m space group.¹ The O^{2-} ions are in an approximately cubic close-packed arrangement with $64/3 \text{ Al}^{3+}$ ions partially occupying the various combinations of symmetrically equivalent positions in the Fd-3m space group. The number of Al^{3+} cations ($64/3$) in the $\gamma\text{-Al}_2\text{O}_3$ structure is based on the assumption that 32 O^{2-} ions occupy the 32e Wyckoff positions; $64/3 \text{ Al}^{3+}$ ions are required to charge balance the 32 O^{2-} ions.¹

The authors find it remarkable to mention that the predicted defect species in $\gamma\text{-Al}_2\text{O}_3$ are an equal number of V_{Mg}'' and V_{O}'' . To our knowledge, the presence of V_{O}'' in $\gamma\text{-Al}_2\text{O}_3$ has not been previously proposed. A consequence of not accounting for the presence of oxygen vacancies is incorrectly determining the number of cations in the unit cell. The present model predicts that 16 Al^{3+} ions and 24 O^{2-} ions describe the $\gamma\text{-Al}_2\text{O}_3$ structure versus the more common $64/3 \text{ Al}^{3+}$ and 32 O^{2-} ions. Numerous attempts to determine the distribution of the cations over the tetrahedral and octahedral sites are reported in the literature; all of which assume $64/3 \text{ Al}^{3+}$ per unit cell.

2.5.5.3 Porosity inherent to defect spinel structures

The number of nickel and oxygen vacancies forming during the hydrogen reaction is dependent on the amount of nickel in the initial $\text{Ni}_x\text{Mg}_{1-x}\text{Al}_2\text{O}_4$ spinel composition. As the amount of nickel increases, the number of vacancies formed in $\text{Mg}_{1-x}\text{Al}_2\text{O}_{4-x}$ following reaction with hydrogen increases. The vacancies that form during the reaction of $\text{Ni}_x\text{Mg}_{1-x}\text{Al}_2\text{O}_4$ with hydrogen correspond to vacancies

in the resulting defect structure for alumina-rich $\text{Mg}_{1-x}\text{Al}_2\text{O}_{4-x}$ spinel. The results of this study indicate that the defect spinel structure consists of an equal number of V_{Mg}'' and V_{O}'' as excess alumina is incorporated in the structure. The number of both anion and cation vacancies forming in $\text{Mg}_{1-x}\text{Al}_2\text{O}_{4-x}$ spinel is equal to $8x$ per unit cell. The formation V_{Mg}'' and V_{O}'' in non-stoichiometric spinel combines with a comparatively small change in the lattice parameter to result in a large free volume. The theoretical free volume for $\text{Mg}_{1-x}\text{Al}_2\text{O}_4$ calculated using the measured lattice parameters and the proposed defect reaction (2b) is shown in Figure 23. This free volume is compared with the free volume for stoichiometric $\text{Ni}_x\text{Mg}_{1-x}\text{Al}_2\text{O}_4$ spinel prior to reaction with hydrogen. The free volume increases with increasing excess alumina due to the formation of increasing amounts of V_{Mg}'' and V_{O}'' .

The free volume in $\text{Mg}_{1-x}\text{Al}_2\text{O}_{4-x}$ spinel may be described as an effective porosity. The defect reaction predicts that the porosity increases as the defect $\text{Mg}_{1-x}\text{Al}_2\text{O}_{4-x}$ spinel composition approaches the $\gamma\text{-Al}_2\text{O}_3$ structure. This analogy is consistent with the porosity that is often observed in $\gamma\text{-Al}_2\text{O}_3$.¹ The contribution of a high concentration of anion and cation vacancies to porosity may explain the refinement results of neutron diffraction data by Zhou and Snyder.¹⁶ They report a large fraction of Al^{3+} ions occupy the non-spinel 32e sites, and speculate that this occupation occurs in the surface layers of $\gamma\text{-Al}_2\text{O}_3$. Molecular dynamics simulations of $\gamma\text{-Al}_2\text{O}_3$ surfaces reveal that this interpretation is accurate¹⁷; however, no clear connection has been made for the relationship of the surface ions to the bulk structure.¹ A clustering of the vacancies in the defect spinel structure is effectively a “nanopore” in the bulk with an associated surface. The Al ions at the surface of these vacancies will presumably occupy the non-spinel 32e sites which have been observed in both neutron diffraction studies and molecular dynamics simulations.

2.6 Conclusions

Many studies focus on the distribution of Al^{3+} and Mg^{2+} over the tetrahedral and octahedral sites in non-stoichiometric spinel. The models used in

these studies are developed on the assumption that 32 oxygen ions occupy the unit cell. The results presented in this study indicate this assumption is not valid. Rather the formation of $V_{O}^{\cdot\cdot}$ increases with increasing Al_2O_3 content. This assumption leads to an incorrect estimate of the cation vacancies per unit cell.

Extension of this proposed defect equation to $\gamma-Al_2O_3$ reveals that the number of ions occupying one formula unit is 2 Al^{3+} and 3 O^{2-} , not $8/3 Al^{3+}$ and 4 O^{2-} (16 Al^{3+} and 24 O^{2-} per unit cell). Clustering of the $V_{O}^{\cdot\cdot}$ and $V_{Al}^{\cdot\cdot}$ results in nanopores which are inherent to the $\gamma-Al_2O_3$ microstructure. One consequence of accounting for an inaccurately high number of cations in the defect structure model of $\gamma-Al_2O_3$ is the determination an incorrect distribution of the cations over the tetrahedral and octahedral sites. The authors are confident that application of the proposed defect reaction: $Al_2O_3 \rightarrow V_{Mg}^{\cdot\cdot} + 2Al_{Al}^{\cdot} + 3O_O^{\cdot} + V_O^{\cdot\cdot}$ for alumina-rich spinel will lead to significant progress in our understanding of the $\gamma-Al_2O_3$ structure.

2.7 References

1. I. Levin and D. Brandon, "Metastable Alumina Polymorphs: Crystal Structures and Transition Sequences," *J. Am. Ceram. Soc.*, **81** [8] 1995-2012 (1998).
2. R. I. Sheldon, T. Hartmann, K. E. Sickafus, A. Ibarra, B. L. Scott, D. N. Argyriou, A. C. Larson, and R. B. Von Dreele, "Cation Disorder and Vacancy Distribution in Nonstoichiometric Magnesium Aluminate Spinel, $MgO_xAl_2O_3$," *J. Am. Ceram. Soc.*, **82** [12] 3293-8 (1999).
3. A. Ibarra, R. Vila, and M. J. de Castro, "On the Cation Vacancy Distribution in $MgAl_2O_4$ Spinel," *Philos. Mag. Lett.*, **64** [1] 45-8 (1991).
4. R. Dupree, M. H. Lewis, and M. E. Smith, "A Study of the Vacancy Distribution in Non-Stoichiometric Spinel by Magic-Angle Spinning NMR," *Philos. Mag. A*, **53** [2] L17-L20 (1986).
5. Topas V3: General Profile and Structure Analysis Software for Powder Diffraction Data, [Computer Program] Bruker AXS, Karlsruhe, Germany, 2005.
6. S. T. Mixture, "Large-Volume Atmosphere-Controlled High Temperature X-Ray Diffraction Furnace," *Meas. Sci. Technol.*, **14** [7] 1091-8 (2003).
7. A. Navrotsky, B. A. Wechsler, K. Geisinger, and F. Seifert, "Thermochemistry of Magnesium Aluminate-Aluminum Oxide ($MgAl_2O_4$ - $Al_{8/3}O_4$) Defect Spinel," *J. Am. Ceram. Soc.*, **69** [5] 418-22 (1986).
8. A. N. Tsvigunov, A. V. Belyakov, P. D. Sarkisov, P. P. Faikov, N. T. Andrianov, B. V. Zhadanov, and Y. V. Ivleva, "Synthesis of Nonstoichiometric Aluminomagnesium Spinel with a Tetragonal Lattice (Review)," *Glass Ceram.*, **63** [11-12] 371-6 (2006).
9. Y. Okuyama, N. Kurita, and N. Fukatsu, "Defect Structure of Alumina-Rich Nonstoichiometric Magnesium Aluminate Spinel," *Solid State Ionics*, **177** [1-2] 59-64 (2006).
10. R. K. Datta and R. Roy, "Order-Disorder in $MgAl_2O_4$. The Systems: $MgAl_2O_4$ - $LiAl_5O_8$, $MgAl_2O_4$ - $NiCr_2O_4$, $MgAl_2O_4$ - $NiAl_2O_4$, and $NiAl_2O_4$ - $ZnAl_2O_4$," *Am. Mineral.*, **53** [9-10] 1456-75 (1968).
11. P. Porta, F. S. Stone, and R. G. Turner, "Distribution of Nickel Ions among Octahedral and Tetrahedral Sites in Nickel Aluminum Oxide-Magnesium Aluminum Oxide ($NiAl_2O_4$ - $MgAl_2O_4$) Solid Solutions," *J. Solid State Chem.*, **11** [2] 135-47 (1974).

12. J. N. Roelofsen, R. C. Peterson, and M. Raudsepp, "Structural Variation in Nickel Aluminate Spinel (NiAl_2O_4)," *Am. Mineral.*, **77** [5-6] 522-8 (1992).
13. H. Jagodzinski and H. Saalfeld, "Distribution of Cations and Structural Relations in Magnesium Aluminum Spinels," *Z. Kristallogr.*, **110**, 197-218 (1958).
14. C.-J. Ting and H.-Y. Lu, "Defect Reactions and the Controlling Mechanism in the Sintering of Magnesium Aluminate Spinel," *J. Am. Ceram. Soc.*, **82** [4] 841-8 (1999).
15. K. P. R. Reddy and A. R. Cooper, "Oxygen Diffusion in Magnesium Aluminate Spinel," *J. Am. Ceram. Soc.*, **64** [6] 368-71 (1981).
16. R. S. Zhou and R. L. Snyder, "Structures and Transformation Mechanisms of the η , γ and θ Transition Aluminas," *Acta Crystallogr., Sect. B: Struct. Sci.*, **B47** [5] 617-30 (1991).
17. S. Blonski and S. H. Garofalini, "Molecular Dynamics Simulations of α -Alumina and γ -Alumina Surfaces," *Surf. Sci.*, **295** [1-2] 263-74 (1993).

2.8 Tables

Table V. Reaction Temperatures and Times for $\text{Ni}_x\text{Mg}_{1-x}\text{Al}_2\text{O}_4$ Spinel Solid Solution, where $0 \leq x \leq 1$, in ~ 300 torr of H_2

Temperature (°C)	Time (hrs)
650	94
700	51
750	29
800	24
850	24
900	12
950	12
1000	12

2.9 Figures

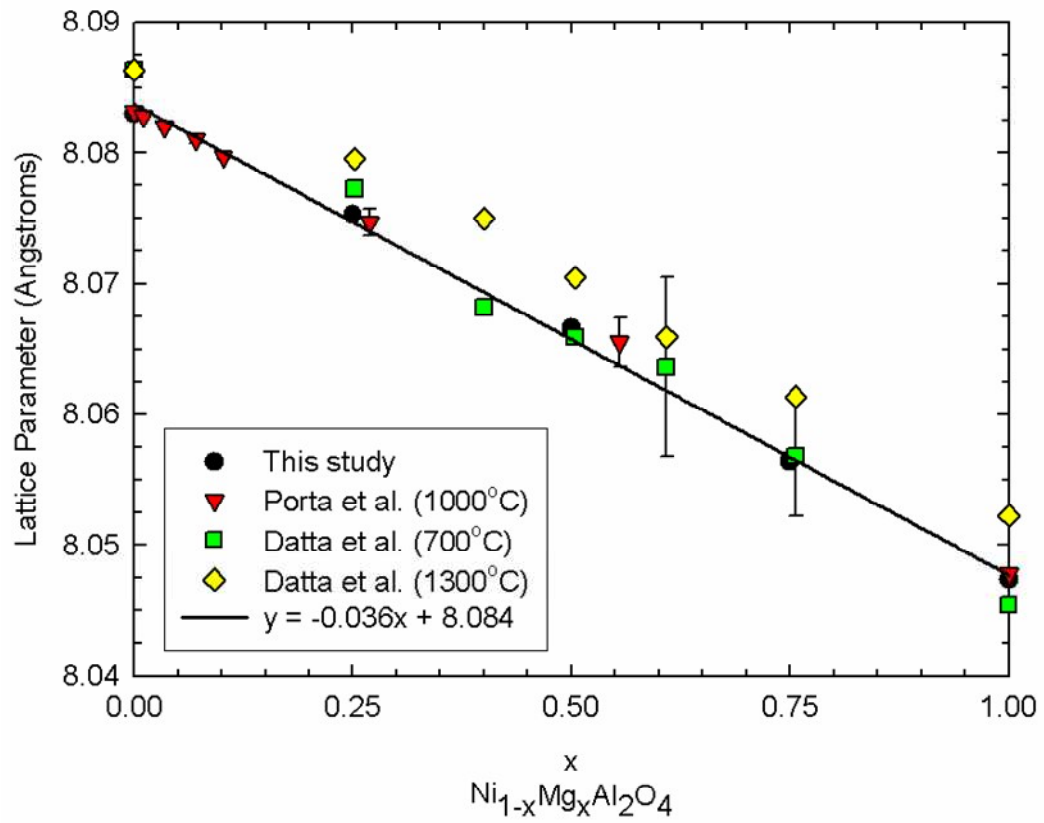


Figure 12. The change in lattice parameter as a function of x for $\text{Ni}_x\text{Mg}_{1-x}\text{Al}_2\text{O}_4$. The error bars for this study are smaller than the data point.

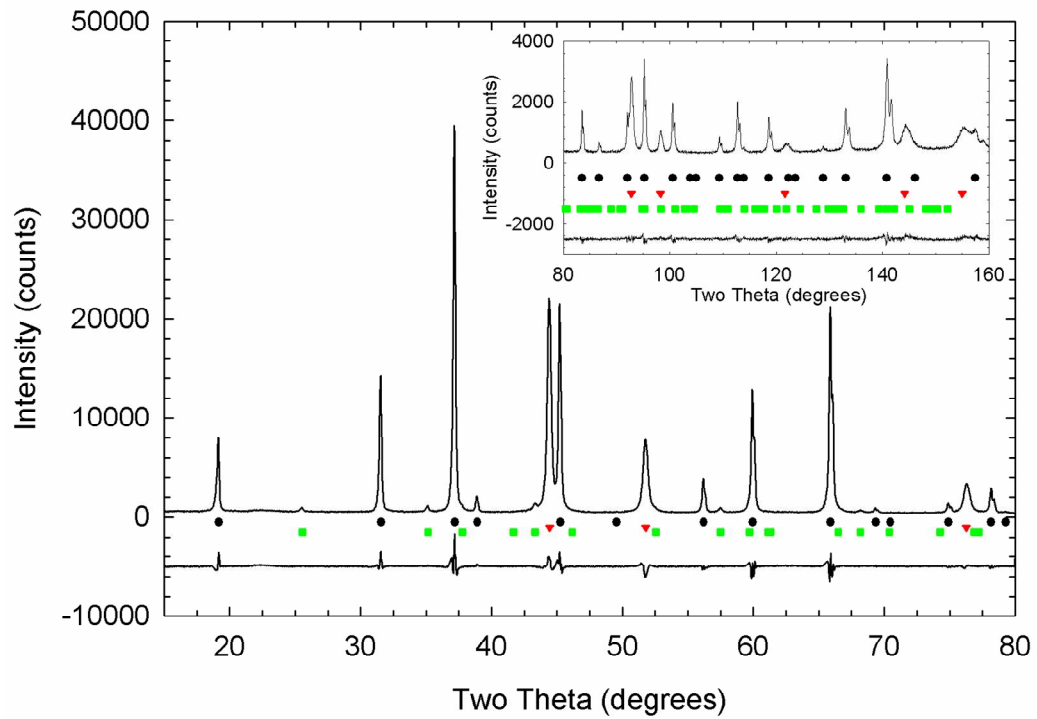


Figure 13. An example refinement of XRD data for $\text{Ni}_{0.5}\text{Mg}_{0.5}\text{Al}_2\text{O}_4$ reacted at 850°C for 24 hrs in H_2 . The markers identifying the diffraction line positions for the respective phases are: black-circles = spinel, red-triangles = nickel, and green-squares = corundum.

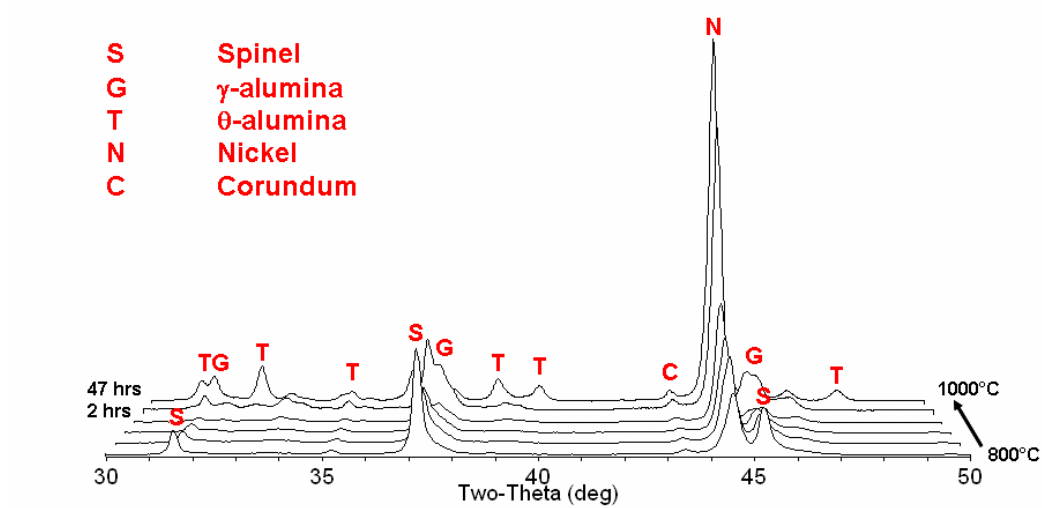


Figure 14. X-ray diffraction data illustrating the transformation of NiAl_2O_4 to metastable alumina polymorphs as the hydrogen reaction temperature increases from 800°C to 1000°C in 50°C intervals. The last two scans are the XRD patterns for the reaction products following reaction with H_2 at 1000°C for 2 hrs and 47 hrs.

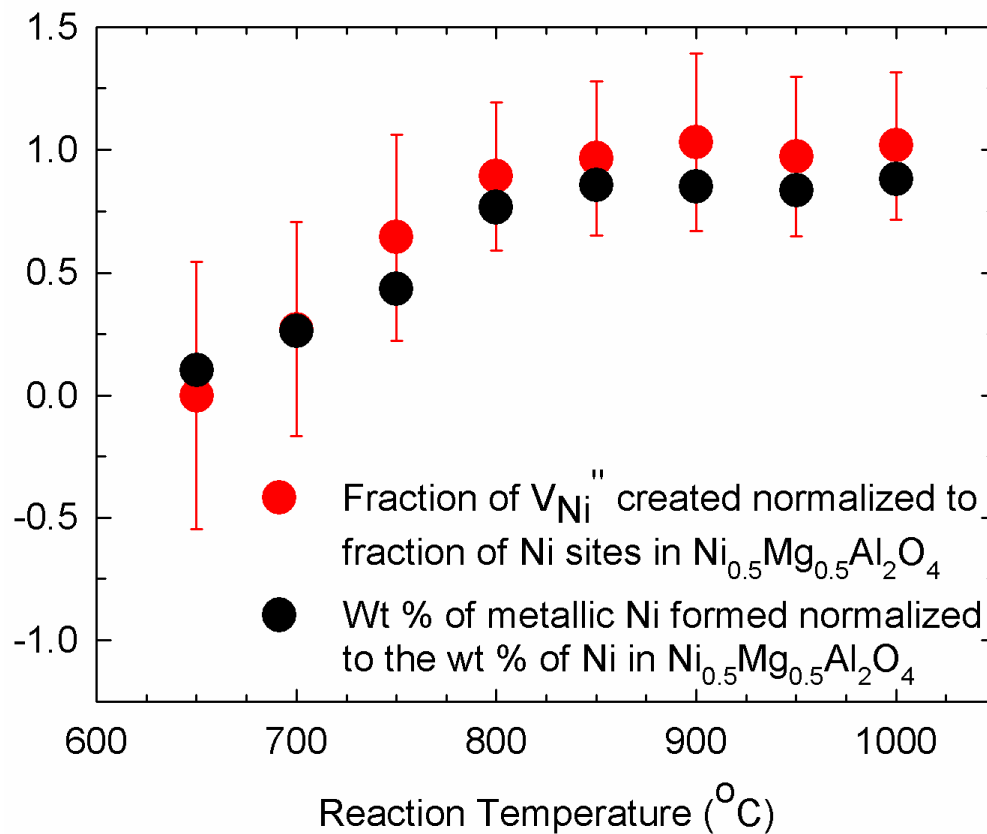


Figure 15. The normalized fraction of nickel vacancies formed and the weight percent of metallic nickel formed during the hydrogen reaction with $\text{Ni}_{0.5}\text{Mg}_{0.5}\text{Al}_2\text{O}_4$ as a function of reaction temperature.

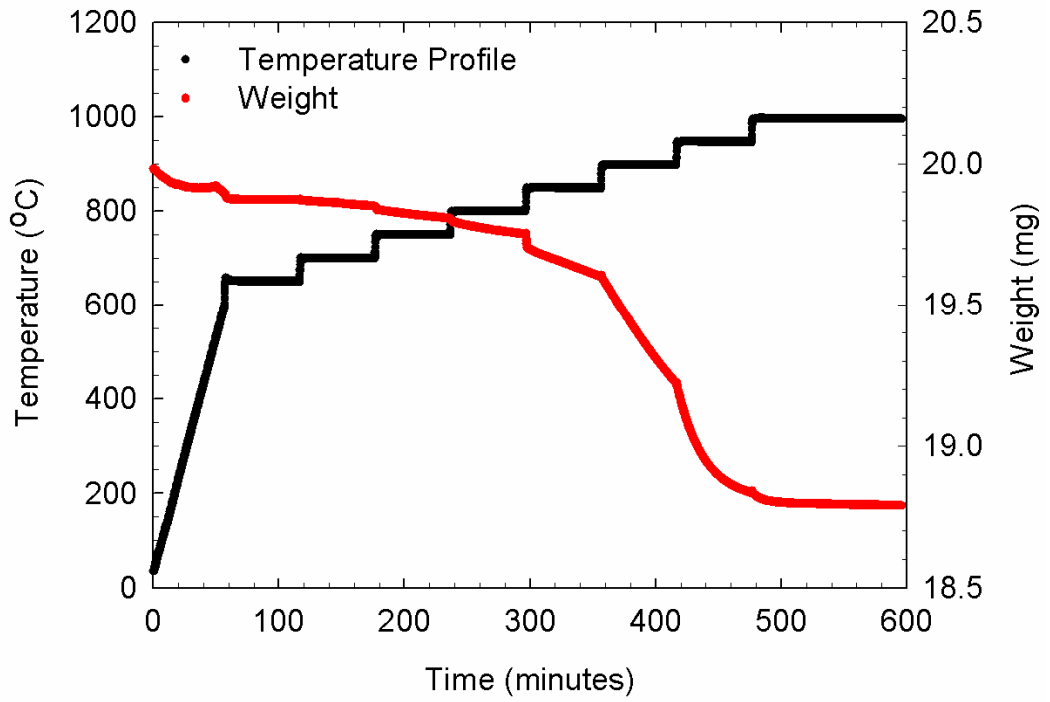


Figure 16. TGA data illustrating the weight loss for the spinel samples as a function of temperature. This data is recorded in-situ in flowing 4H₂-96N₂ at 100 mL/min.

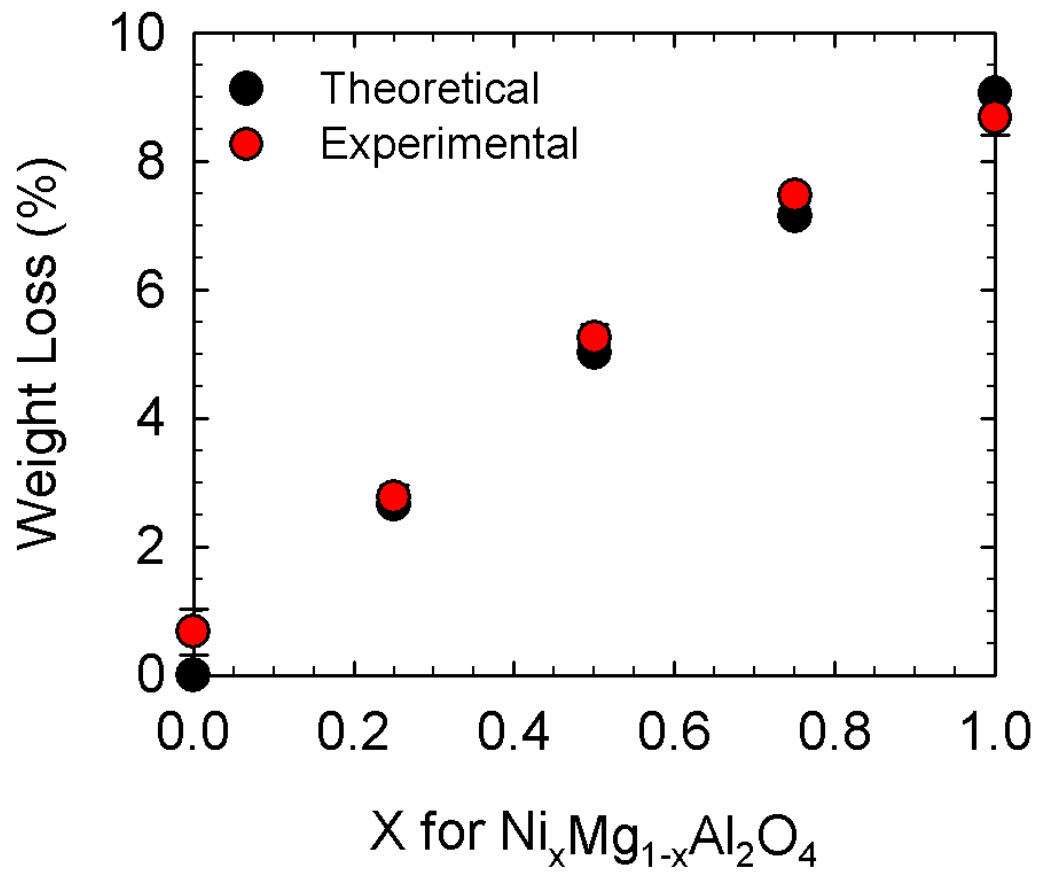


Figure 17. The experimentally determined weight loss in the spinel compositions $\text{Ni}_x\text{Mg}_{1-x}\text{Al}_2\text{O}_4$ during reaction with hydrogen at 1000°C is compared with a theoretical weight loss due to the formation of oxygen vacancies.

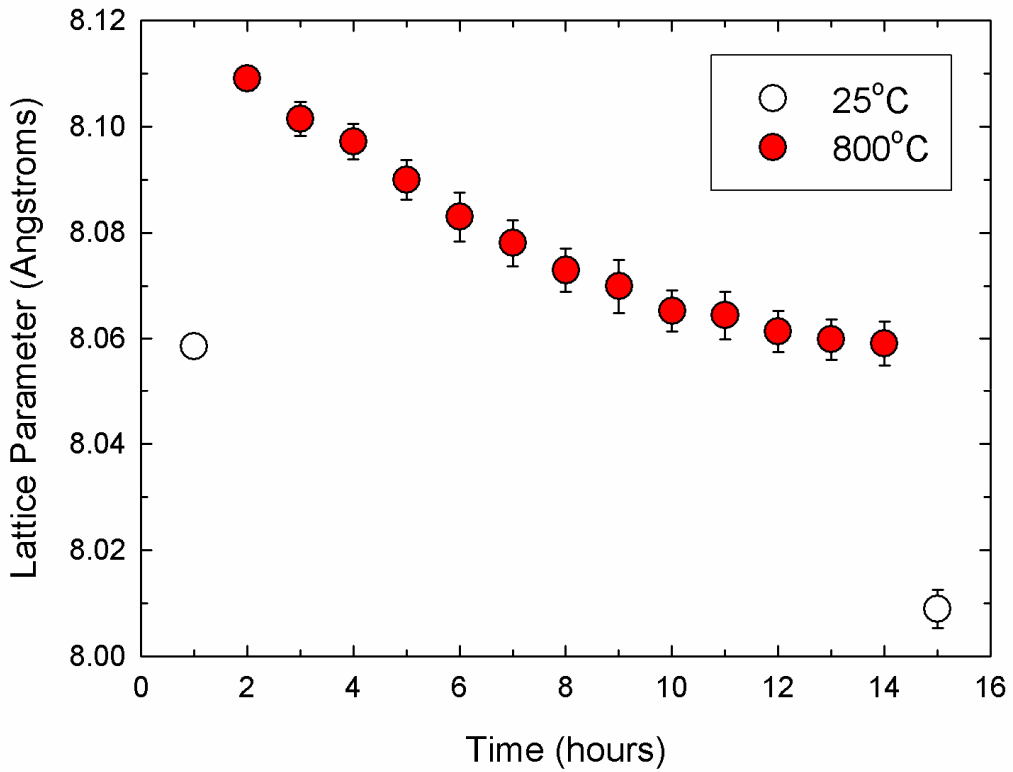
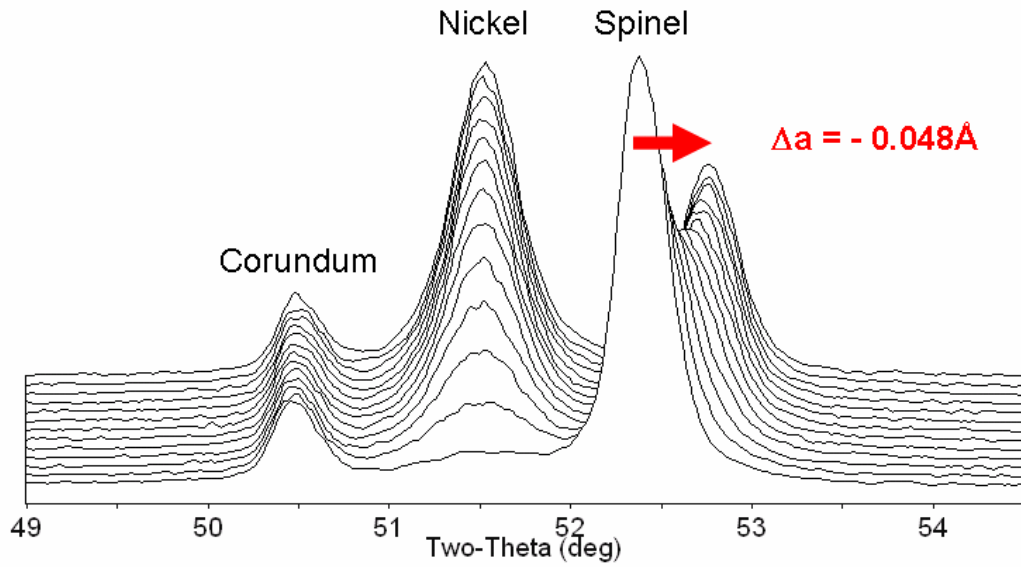


Figure 18. (a) In situ XRD of $\text{Ni}_{0.5}\text{Mg}_{0.5}\text{Al}_2\text{O}_4$ in flowing $4\text{H}_2\text{-}96\text{N}_2$ at 800°C . Successive scans were recorded in 1 hour intervals. (b) Change in lattice parameter as Ni is reduced from $\text{Ni}_{0.5}\text{Mg}_{0.5}\text{Al}_2\text{O}_4$ during reaction with H_2 .

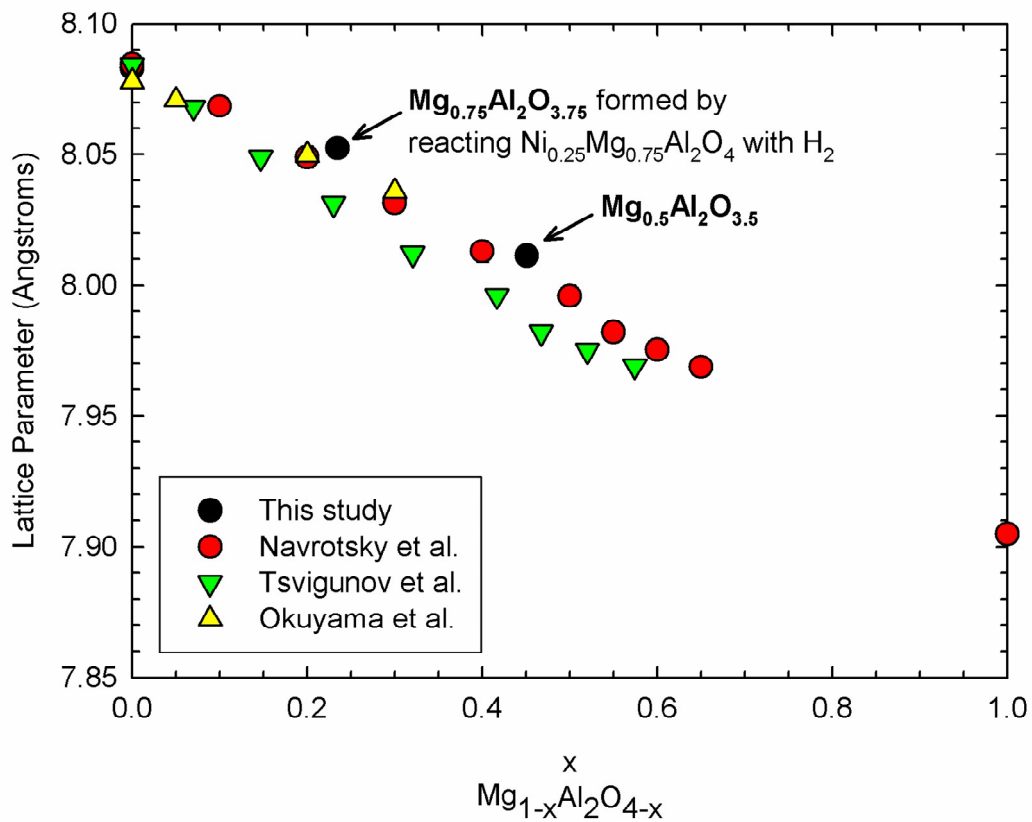


Figure 19. Change in lattice parameter for compositions MgAl_2O_4 , $\text{Mg}_{0.75}\text{Al}_2\text{O}_{3.75}$, $\text{Mg}_{0.5}\text{Al}_2\text{O}_{3.5}$, $\text{Mg}_{0.25}\text{Al}_2\text{O}_{3.25}$ formed through reaction of $\text{Ni}_x\text{Mg}_{1-x}\text{Al}_2\text{O}_4$ with hydrogen.

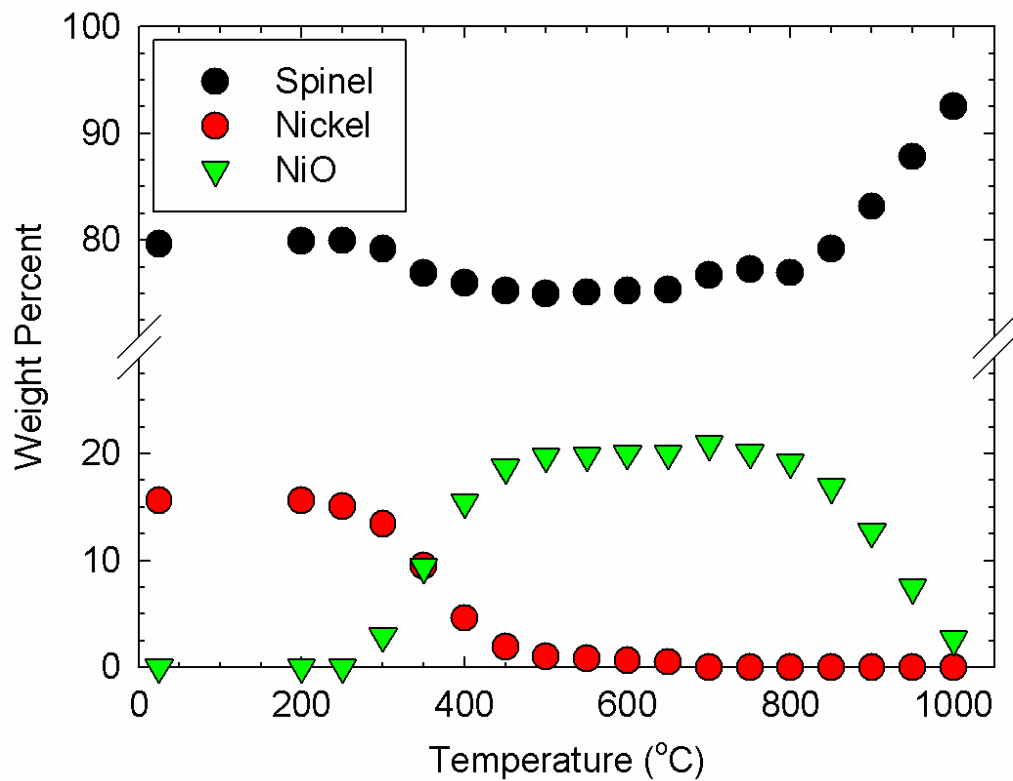


Figure 20. The weight percent of phases calculated from in situ XRD data recorded for the re-oxidation of Ni + Mg_{0.5}Al₂O_{3.5} (Ni_{0.5}Mg_{0.5}Al₂O₄ previously reacted at 1000°C in H₂) following 1 hr at respective reaction temperature. The error bars are smaller than the data point.

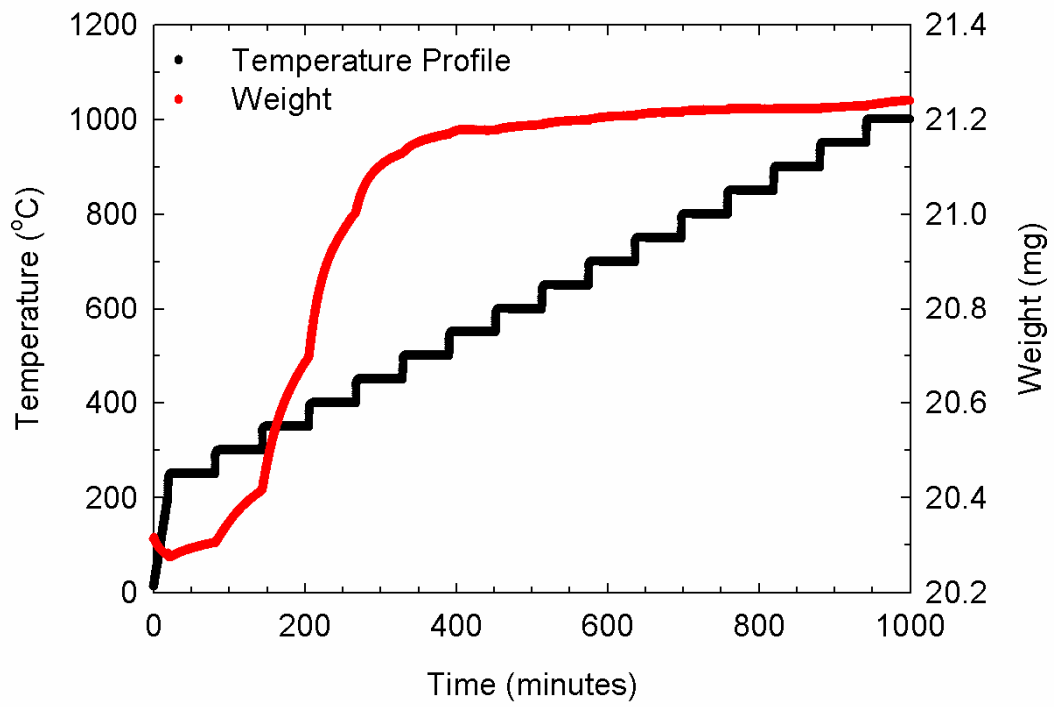


Figure 21. In situ TGA data showing the weight gain as Ni + Mg_{0.5}Al₂O_{3.5} re-oxidizes to form Ni_{0.5}Mg_{0.5}Al₂O₄.

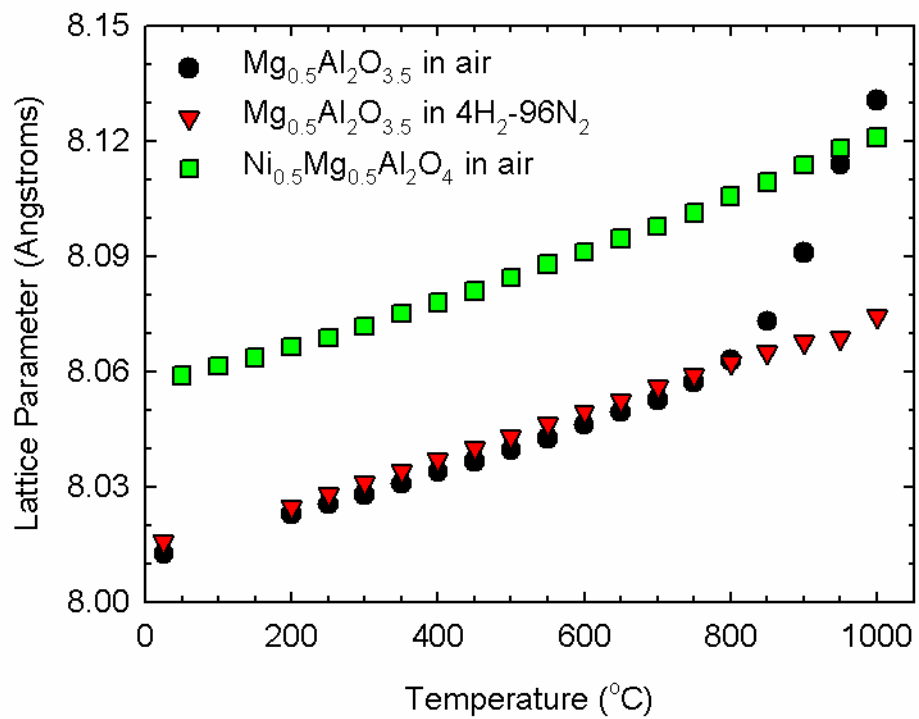


Figure 22. The change in the spinel lattice parameter calculated from HTXRD data recorded in situ for the re-oxidation of Ni + $\text{Mg}_{0.5}\text{Al}_2\text{O}_{3.5}$ ($\text{Ni}_{0.5}\text{Mg}_{0.5}\text{Al}_2\text{O}_4$ previously reacted at 1000°C in H_2). The error bars are smaller than the data point.

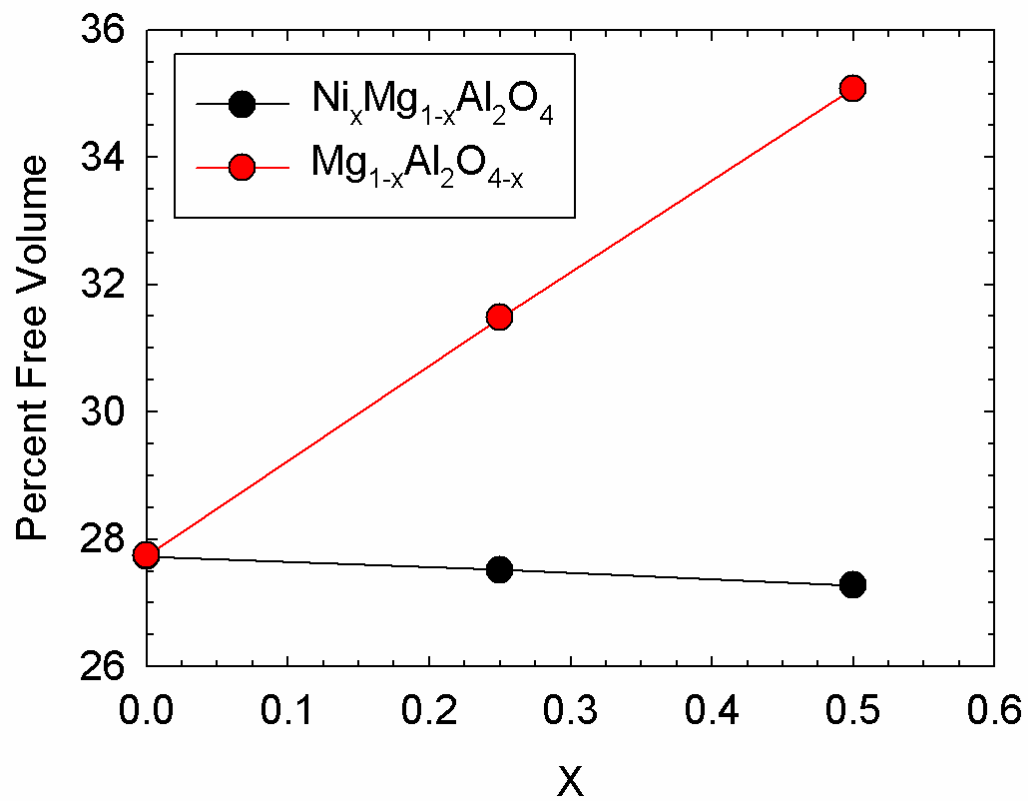


Figure 23. The percent free volume in $\text{Ni}_x\text{Mg}_{1-x}\text{Al}_2\text{O}_4$ and $\text{Mg}_{1-x}\text{Al}_2\text{O}_{4-x}$ calculated using the measured lattice parameters.

Chapter 3: (Ni,Mg)-aluminate Spinel Catalysts

3.1 Abstract

The present study focuses on the activation and phase stability of $\text{Ni}_x\text{Mg}_{1-x}\text{Al}_2\text{O}_4$ spinel, where $0 \leq x \leq 1$ in dry hydrogen atmospheres. The reduced spinels form evenly dispersed metallic nickel crystallites supported on non-stoichiometric $\text{Mg}_{1-x}\text{Al}_2\text{O}_{4-x}$ spinel. The average nickel crystallite size ranges from ca. 10 nm at 650°C to ca. 80 nm at 1000°C. The dispersion of the nickel crystallites increases with higher nickel loadings. The stability limit for the non-stoichiometric $\text{Mg}_{1-x}\text{Al}_2\text{O}_{4-x}$ spinel is determined to be between $0.5 \leq x \leq 0.75$ using Rietveld refinement of X-ray diffraction data. The large volume shrinkage in the spinel phase, attributed to the reduction of Ni from the framework, induces a significant amount of strain in the non-stoichiometric spinel support. Based on the results of previous researchers, this strain is speculated to contribute to the reforming activity of methane. *In situ* diffraction reveals that the re-oxidation of Ni/Mg_{0.5}Al₂O_{3.5} in air results in the oxidation of the supported nickel for temperatures between 300-500°C, while the re-oxidation of $\text{Mg}_{1-x}\text{Al}_2\text{O}_{4-x}$ requires temperatures in excess of 800°C.

3.2 Introduction

The development of Ni-based catalysts for methane reforming reactions is desirable due to the high cost and limited availability of supported noble metal catalysts (Rh, Ru, Ir, Pt, and Pd). The catalytic activity of Ni supported on various oxides for methane decomposition has been extensively reported in the literature.¹⁻⁸ Deactivation of these catalysts results from sintering of both the support and the metal crystallites, carbon deposition on the metal, oxidation of the metal, sulfur poisoning of the metal, and phase transformations of the catalyst during time on stream.⁹

The support substrate is a significant factor in the performance of the catalyst – dictating the ability of the catalyst to resist both sintering and coking.^{1, 4, 10-12} The ability of the support to maintain a high dispersion of nickel crystallites during operation aids the long term stability of the catalyst against deactivation. The successful stabilization of nickel by the support will suppress its rate of sintering. Sintering of the Ni limits the activity of the catalyst by reducing the number of active sites and increasing the average particle size. Growth of the Ni particles beyond a critical ensemble size enables the nucleation of carbon.^{13, 14} The accumulation of carbon deactivates the catalyst by blocking the active sites. A strong interaction between the Ni and the support will yield a catalyst that exhibits an excellent resistance to both sintering and coking.

Activated [Ni,Mg]Al₂O₄ catalysts have been widely studied for use in methane reforming reactions. Both Ni/NiAl₂O₄ and Ni/MgAl₂O₄ catalysts exhibit high activities and good resistance to sintering.^{1, 11} The sintering resistance of these catalysts is attributed to the high temperatures that are required to reduce the nickel from these catalysts indicating a strong interaction of the nickel with the support. In a recent study on Ni/ γ -Al₂O₃ catalysts for CO₂ reforming of CH₄ it is observed that the γ -Al₂O₃ support contributes more to the reforming activity than the supported metallic nickel.¹⁰ However, metastable γ -Al₂O₃ transitions to catalytically inactive α -Al₂O₃ during operation.¹⁵ Accompanied with this phase transition is a drastic decrease in surface area of the alumina support.^{16, 17}

Reduced NiAl_2O_4 spinel forms metallic nickel and $\gamma\text{-Al}_2\text{O}_3$ effectively forming the $\text{Ni}/\gamma\text{-Al}_2\text{O}_3$ reported by Cheng et al.¹⁰ The addition of Mg to $\gamma\text{-Al}_2\text{O}_3$ improves the stability of the catalyst and its resistance to coke formation.¹¹ These individual observations may be combined by reducing (Ni,Mg)-aluminate spinel to develop a catalyst exhibiting the activity of $\gamma\text{-Al}_2\text{O}_3$ and the stability of Mg-doped $\gamma\text{-Al}_2\text{O}_3$. The present study focuses on the activation and phase stability of (Ni,Mg)-aluminate spinel in dry hydrogen atmospheres. The performance of these materials in methane reforming reactions is evaluated based on reports in the literature for similar Ni-based catalysts.

3.3 Experimental procedure

The compositional series $\text{Ni}_x\text{Mg}_{1-x}\text{Al}_2\text{O}_4$, where $0 \leq x \leq 1$, was synthesized from reagent grade $\text{Mg}(\text{OH})_2$, NiO , and Al_2O_3 powders. Pellets were sintered at 1450°C in increments of 18 hrs until phase purity was achieved. Between sintering cycles the pellets were crushed and ground using an alumina mortar and pestle for analysis using XRD. Following the synthesis, the spinel powders were ball milled using alumina media in deionized water and subsequently dried at 90°C .

The hydrogen reactions with the spinel powders were conducted in a closed system of ~ 300 torr of ultra pure H_2 for various times. The heat treatment temperatures and times are recorded in Table I. The reaction times exceed the time required to completely react the spinel samples with hydrogen for the given temperature. The completion of the hydrogen reaction was determined using *in situ* high temperature X-ray diffraction for isothermal treatments in flowing $4\text{H}_2\text{-}96\text{N}_2$. The end of the reaction is determined to be the time at which the formation of additional metallic nickel ceases.

X-ray diffraction data was collected using $\text{CuK}\alpha$ radiation in Bragg-Brentano geometry. Data was collected from $5\text{-}160^\circ 2\theta$ using a 0.03° step size and 5 second dwell time. Topas V3 software was used to perform Rietveld refinement analyses on the X-ray diffraction data.¹⁸ Thermogravimetric measurements were collected under flowing $4\text{H}_2\text{-}96\text{N}_2$ at 50 mL/min . The TGA

measurements were recorded three or more times to determine the experimental error. Scanning electron microscopy was performed using an FEI Quanta 200F field emission environmental electron microscope equipped with a backscatter detector, and EDX detector.

3.4 Results

3.4.1 Formation of metallic nickel

The reaction of hydrogen with (Ni,Mg)-aluminate spinel powders results in the formation of metallic nickel for all temperatures between 650°C and 1000°C. Figure 24 shows a back-scattered ESEM image of $\text{Ni}_{0.5}\text{Mg}_{0.5}\text{Al}_2\text{O}_4$ powder prior to and following reaction with hydrogen at 950°C for 12 hrs. Following reaction with hydrogen, evenly dispersed nickel metal crystallites are formed on the surface of the spinel powders. The bright white crystallites are metallic nickel supported on non-stoichiometric/defect spinel powder.

3.4.2 Temperature vs. size of crystallites

The size of the nickel crystallites formed during the hydrogen reaction is dependent on the reaction temperature. A plot of this trend is shown in Figure 25 for all nickel containing compositions. The average crystallite size ranges from ca. 10 nm for reactions occurring at 650°C to ca. 80 nm at 1000°C. There is no systematic effect of composition on the size of the crystallites for a given reaction temperature, however, the weight percent of metallic nickel formed at each reaction temperature is affected by the composition.

3.4.3 Time vs. size of crystallites

The average crystallite size of the nickel crystallites shown in Figure 25 is collected for reaction times varying from 12 hours at 1000°C to 94 hrs at 650°C. The reaction times for the data shown in Figure 25 are given in Table VI. These reaction times exceed the time required to fully react the spinel for a given reaction temperature. Though the reaction times vary significantly within this data set, the average crystallite size of the nickel crystallites exhibits a strong linear dependence on reaction temperature.

3.4.4 Wt % of metallic Ni vs. Size

A direct comparison of the average crystallite size with the weight percent of metallic nickel formed is shown in Figure 26. This plot reveals that the relationship between the average crystallite size and the weight percent of metallic nickel formed is dependent on the spinel composition. As metallic nickel is formed through the reaction of spinel with hydrogen the average crystallite size increases. The crystallite growth rate as a function of metallic nickel formed is compositionally dependent. Crystallites formed during the hydrogen reaction with spinel compositions containing a higher amount of nickel ($\text{Ni}_{0.5}\text{Mg}_{0.5}\text{Al}_2\text{O}_4$) exhibit a slower growth rate as metallic nickel is formed; e.g. for $\text{Ni}_{0.25}\text{Mg}_{0.75}\text{Al}_2\text{O}_4$ reacted with hydrogen at 750°C, 4 wt % Ni is formed and the average crystallite size is 20 nm; for $\text{Ni}_{0.5}\text{Mg}_{0.5}\text{Al}_2\text{O}_4$ reacted with hydrogen at 700°C, 4.8 wt % Ni is formed and the average crystallite size is 12 nm. Though smaller crystallites have formed on the $\text{Ni}_{0.5}\text{Mg}_{0.5}\text{Al}_2\text{O}_4$, a larger percentage of the reaction product is metallic nickel.

3.4.5 Reaction products

3.4.5.1 Spinel stability limits

The products of the hydrogen reaction with spinel are dependent on the spinel composition. For the spinel compositions $\text{Ni}_x\text{Mg}_{1-x}\text{Al}_2\text{O}_4$, where $X \leq 0.50$, the products are non-stoichiometric spinel and metallic nickel. The composition of the non-stoichiometric spinel depends on the amount of nickel reduced from the spinel phase. The authors have shown that the non-stoichiometric spinel phase formed through reaction with hydrogen contains an equivalent number of nickel vacancies and oxygen vacancies. The composition of the non-stoichiometric spinel phase formed via the selective reduction of nickel from the lattice is written as $\text{Mg}_{1-x}\text{Al}_2\text{O}_{4-x}$ to reflect the stoichiometry of this defect spinel structure. The spinel compositions with nickel contents for $X \geq 0.75$ result in the formation of transition alumina polymorphs in addition to the formation of metallic nickel.

3.4.5.2 Transition sequence for $Ni_{0.75}Mg_{0.25}Al_2O_4$ and $NiAl_2O_4$

The partial transformation of $Ni_{0.75}Mg_{0.25}Al_2O_4$ and $NiAl_2O_4$ to γ alumina begins as early as 800°C. The development of superstructure lines as a result of cation ordering in the spinel phase is observed in the X-ray diffraction patterns for $Ni_{0.75}Mg_{0.25}Al_2O_4$ and $NiAl_2O_4$. A subsequent transition of the gamma alumina does not occur at any reaction temperature up to 1000°C for $Ni_{0.75}Mg_{0.25}Al_2O_4$. The reaction products for $NiAl_2O_4$ at temperatures ranging from 800°C to 1000°C are shown in Figure 29. For the $NiAl_2O_4$ reaction with hydrogen, the transition sequence from gamma alumina to theta alumina is observed at 1000°C. The extent of the gamma alumina to theta alumina transition is time dependent. The transition of theta alumina to alpha alumina is not observed within 47 hours at 1000°C.

3.4.5.3 Quantification of phases

The weight fractions of the products formed during the hydrogen reaction are determined from the Rietveld refinement of X-ray diffraction data. An example set of data illustrating the quality of these refinements is shown in Figure 27. The corundum present in the sample is the result of ball milling the powders prior to the reaction with hydrogen. The amount of corundum does not change during the hydrogen reaction indicating that it does not affect products of the reaction.

The formation of metallic nickel as a function of the reaction temperature is shown in Figure 28. The weight percent of metallic nickel formed increases with increasing reaction temperature until a maximum is reached at 850°C. For reaction temperatures exceeding 850°C, no additional metallic nickel is formed. The maxima for $Ni_{0.25}Mg_{0.75}Al_2O_4$ and $Ni_{0.5}Mg_{0.5}Al_2O_4$ correspond to the weight percent of nickel in the respective spinel composition prior to reaction with hydrogen. The maxima are indicated in the Figure 28 by horizontal lines which are color coordinated with the respective composition. The temperature at which the maxima are attained is compositionally independent. All nickel is reduced

from each composition for reaction temperatures $\geq 850^{\circ}\text{C}$ for the reaction times listed in Table VI.

3.4.6 Re-oxidation of reduced (Ni,Mg)-aluminate spinels

The re-oxidation of the reduced $\text{Ni}_{0.5}\text{Mg}_{0.5}\text{Al}_2\text{O}_4$ spinel ($\text{Ni}/\text{Mg}_{0.5}\text{Al}_2\text{O}_{3.5}$) following reaction at 1000°C for 12 hrs is shown in Figure 31. These X-ray data are collected in situ following a 1 hr dwell at each temperature in static air. The weight fraction for each phase is calculated using Rietveld refinement. A plot of the phase fractions for each dwell temperature is given in Figure 31. Oxidation of the metallic nickel begins at 300°C and is complete by 500°C . Between 500°C and 800°C there is no apparent reaction between the NiO, $\text{Mg}_{0.5}\text{Al}_2\text{O}_{3.5}$ and corundum. At 800°C the non-stoichiometric spinel begins to react with the NiO. This reaction is depicted by the decrease in weight loss of NiO concurrent with the increase in weight percent of spinel. The residual corundum that is present from the ball milling of the powders remains unreacted throughout the re-oxidation reaction. The dissolution of NiO into the spinel phase is nearly complete following reaction at 1000°C for 1 hr.

3.4.7 Spinel structure

3.4.7.1 Lattice Constant & Strain

During the reaction of hydrogen with (Ni,Mg)-aluminate spinel, nickel is reduced from the spinel structure. The associated changes in the spinel lattice constant and lattice strain with the selective reduction of nickel from $\text{Ni}_{0.5}\text{Mg}_{0.5}\text{Al}_2\text{O}_4$ are shown in Figure 30. The spinel lattice collapses with increasing reaction temperature until a minimum in the lattice parameter is reached at 850°C . The collapse of the lattice correlates with the formation of metallic nickel. The lattice parameter decreases for the reaction temperatures during which nickel is selectively reduced from the lattice. Once all of the nickel is reduced from the spinel framework, the lattice parameter reaches a minimum value. Concurrent with the collapse of the lattice is the build up of strain. The strain reaches a maximum at 750°C before being partially relieved to a constant value at 850°C .

3.5 Discussion

3.5.1 Formation of metallic nickel

It is observed that the average crystallite size of the metallic nickel formed during the reduction reaction is about the same for all compositions at a given reaction temperature; however, more metallic nickel is formed for compositions containing a higher nickel content in the spinel phase prior to the hydrogen reaction. These relationships imply that the concentration of nucleation sites is higher for spinel samples containing more nickel in the spinel phase prior to the hydrogen reaction. A larger concentration of nuclei results in a larger number of metallic nickel crystallites with a smaller average crystallite size. The nickel atoms are distributed over a larger number of sites, thereby reducing the average crystallite size. Based on this observation, we conclude that the number of nucleation sites for crystallite growth increases along the series $\text{MgAl}_2\text{O}_4 < \text{Ni}_{0.25}\text{Mg}_{0.75}\text{Al}_2\text{O}_4 < \text{Ni}_{0.5}\text{Mg}_{0.5}\text{Al}_2\text{O}_4$.

Both minimizing the size and maximizing the number of Ni crystallites is beneficial to methane reforming processes. Bengaard et al. show that small nickel particles below a critical size do not form carbon.¹³ The study consists of two Ni-based catalysts supported on MgAl_2O_4 each having a different nickel particle size. The catalyst containing larger nickel particles exhibits a faster rate of carbon formation, and a lower onset temperature for the growth of carbon relative to the catalyst containing smaller nickel particles. The larger number of nickel particles formed on the support is effectively more reaction sites, thereby, enhancing the efficiency of the methane reforming reaction.⁹

The linear relationship describing the dependence of the average crystallite size of the nickel crystallites on the reaction temperature, despite the widely varying reaction times, indicates that the final size of the nickel crystallites is independent of the reaction time. Sintering of the nickel does not occur for longer reaction times.

3.5.2 Reaction products

3.5.2.1 Spinel stability limits

The stability limit for non-stoichiometric magnesium aluminate spinel is determined from the appearance of decomposition products in the X-ray diffraction patterns. The stability limit for the non-stoichiometric $\text{Mg}_{1-x}\text{Al}_2\text{O}_{4-x}$ spinel formed through the reaction of hydrogen with (Ni,Mg)-aluminate spinel lies between $0.50 < X < 0.75$. The $\text{Ni}_{0.5}\text{Mg}_{0.5}\text{Al}_2\text{O}_4$ is stable over the temperature range from 650°C to 1000°C following the complete reduction of nickel from the spinel framework. However, $\text{Ni}_{0.75}\text{Mg}_{0.25}\text{Al}_2\text{O}_4$ begins to transition to gamma alumina through reaction with H_2 at 800°C for long annealing times.

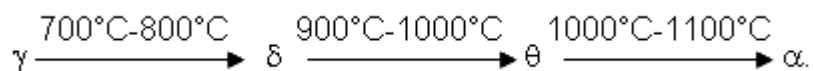
According to Colin the stable phases for $\text{MgO} \cdot x\text{Al}_2\text{O}_3$ where $X > 1$ are γ alumina and α alumina for temperatures between 800°C and 1000°C under reducing conditions.¹⁹ In this study, there is no evidence of α - Al_2O_3 forming as the result of the spinel phase decomposing at temperatures $\leq 1000^\circ\text{C}$. However, Navrotsky et al. report that the solubility limit for the synthesis of $(1-x)\text{MgAl}_2\text{O}_4 \cdot x\text{Al}_{8/3}\text{O}_4$ spinel in air lies near $x=0.65$, at which point excess alumina is no longer dissolved into the spinel structure.²⁰ This discrepancy is the result of the different synthesis routes amongst the studies. Navrotsky et al. prepared $(1-x)\text{MgAl}_2\text{O}_4 - x\text{Al}_{8/3}\text{O}_4$ solid solutions for $0.55 \leq X \leq 0.65$ at 1840°C for 1 hr in air and quenched the samples into water. The phase field developed by Colin predicts that such solid solutions are stable at 1840°C under reducing conditions. These findings indicate that the reaction times used are too short for the phase transformation of spinel into γ - Al_2O_3 and α - Al_2O_3 to be realized. This result is rather intriguing because the formation of $\text{Mg}_{0.5}\text{Al}_2\text{O}_{3.5}$ through solid state reaction requires temperatures in excess of 1600°C, whereas it is formed at 850°C through the hydrogen reaction with $[\text{Ni},\text{Mg}]\text{Al}_2\text{O}_4$.^{19, 21, 22}

3.5.2.2 Transition sequence for $\text{Ni}_{0.75}\text{Mg}_{0.25}\text{Al}_2\text{O}_4$ and NiAl_2O_4

$\text{Ni}_{0.75}\text{Mg}_{0.25}\text{Al}_2\text{O}_4$ and NiAl_2O_4 do not form stable non-stoichiometric spinel phases following the complete reduction of nickel from the lattice. This result is

consistent with the observations discussed in the previous paragraph. The compositional limit for non-stoichiometric $\text{Mg}_{1-x}\text{Al}_2\text{O}_{4-x}$ lies near $x=0.71$.²⁰ The presence of Mg prevents the transformation of the reduced $\text{Ni}_{0.75}\text{Mg}_{0.25}\text{Al}_2\text{O}_4$ into $\theta\text{-Al}_2\text{O}_3$. Stabilizing the $\gamma\text{-Al}_2\text{O}_3$ structure is desirable to prevent the dramatic decrease in surface area associated with the transition to $\theta\text{-Al}_2\text{O}_3$.^{16, 17} The incorporation of Mg into $\gamma\text{-Al}_2\text{O}_3$ significantly increases the stability of the catalyst and its coking resistance presumably by suppressing the transition of $\gamma\text{-Al}_2\text{O}_3$ to δ , θ or α -alumina polymorphs.¹¹

The reaction sequence for $\text{Ni}_{0.75}\text{Mg}_{0.25}\text{Al}_2\text{O}_4$ and NiAl_2O_4 differs due to the stabilizing effect of magnesium in the $\gamma\text{-Al}_2\text{O}_3$ structure. The transformation of the NiAl_2O_4 spinel following reaction with hydrogen at temperatures $\geq 800^\circ\text{C}$ resembles the reaction path exhibited for the dehydroxylation of boehmite.²³ The phase transformation of boehmite from $\gamma \rightarrow \alpha$ alumina is reported to occur via the following reaction sequence:



The temperatures for which the transitions between the metastable phases occur are indicated. The translational structures of the transition alumina polymorphs refer to the degree of cation ordering. The oxygen sublattice of the transition aluminas is continuous with the stoichiometric spinel phase.²³ The transformation sequence observed for the reduction of NiAl_2O_4 does not include the transition through δ alumina; rather a direct transition from $\gamma \rightarrow \theta$ is observed at 1000°C . Consistent with this observation, Moroz et al. report the transformation sequence for nickel doped alumina to be $\gamma \rightarrow \theta \rightarrow \alpha$.²⁴ They speculate that the occupation of divalent nickel in the tetrahedral sites forces aluminum into strictly occupying octahedral sites, thereby, inhibiting the structural rearrangement to $\delta\text{-Al}_2\text{O}_3$. This transformation sequence implies that some unreacted nickel remains in the metastable alumina polymorphs during the hydrogen reactions. The transition of $\theta\text{-Al}_2\text{O}_3$ into stable $\alpha\text{-Al}_2\text{O}_3$ occurs for temperatures in excess of 1000°C . The partial reduction of NiAl_2O_4 at 1100°C

and 1300°C results in the formation of metallic nickel and α -Al₂O₃ with residual defect spinel at the reaction interface.²⁵

The transition of $\gamma \rightarrow \delta$ alumina and $\delta \rightarrow \theta$ alumina is accompanied by sintering of the nanoporous microstructure characteristic of γ -alumina. This sintering process results in a significant reduction of the internal surface area.²⁶ The partial transformation of a Ni/ γ -Al₂O₃ catalyst to α -Al₂O₃ in CH₄ reforming with CO₂ results in a drastic decrease in surface area.⁴ Ultimately, the complete transformation of γ -Al₂O₃ into α -Al₂O₃ will lead to deactivation of the alumina support. Fully dehydroxylated α -alumina is not catalytically active, though the defect structures of the transition aluminas are active.¹⁵

The characteristic microstructures of the γ , δ , and θ aluminas formed by the dehydration of boehmite (γ -AlOOH) are independent of the preparation time and temperature.²⁷ Transcription of this behavior to our system implies that the microstructure of the γ -alumina formed in this study is characteristic of that formed by dehydrating boehmite. The catalytic activity of the transition aluminas is dependent on the stoichiometry, texture and structure. The continuous transformation of the non-stoichiometric spinel into γ -Al₂O₃ with higher nickel loadings is an indication of the catalytic activity of these supports.

3.5.3 Quantification of phases

The reduction of nickel from the spinel solid solutions exhibits the same temperature dependence independent of the composition. This observation implies that the reducibility of the nickel from the solid solutions is compositionally independent. As a result, the interaction of the nickel particles with the non-stoichiometric spinel support is expected to be the same for Ni_{0.25}Mg_{0.75}Al₂O₄ and Ni_{0.5}Mg_{0.5}Al₂O₄ compositions. This conclusion is not drawn for Ni_{0.75}Mg_{0.25}Al₂O₄ and NiAl₂O₄ due to the instability of the Mg_{1-x}Al₂O_{4-x} defect spinel for $x \geq 0.71$.

3.5.4 Re-oxidation of reduced (Ni,Mg)-aluminate spinels

The re-oxidation of Ni occurs at very low temperature (300°C-500°C), however, the NiO does not begin to dissolve back into the spinel phase until

800°C. This result offers an explanation for the re-reduction behavior of a spent Ni/MgO-doped α -Al₂O₃ catalyst observed by Richardson et al.²⁸ The catalyst initially reduced at 710°C, however, upon re-reduction of the oxidized catalyst the reduction temperature dropped to 312°C. This decrease in reduction temperature may result because the calcination temperature (650°C) was too low and/or the time was too short to completely react the nickel oxide with the MgO-doped alumina support.

3.5.5 Spinel structure

3.5.5.1 Lattice strain

The strain is maximized concurrently with the sharp decrease in lattice parameter. The gradual release of the strain over the reaction temperatures from 750°C to 850°C implies that the strain is relieved through structural rearrangements rather than microcracking of the grains. There is no cracking observed at the NiAl₂O₄/Al₂O₃ interface during the reduction of NiAl₂O₄ at 1350°C for 0.5 hrs, though cracking is frequently observed at the original spinel grain boundaries.²⁹

The reaction paths observed for the reduction reaction of (Ni,Mg)-aluminate spinel parallel those exhibited by boehmite. It follows that comparisons can be made between the non-stoichiometric spinels and transition aluminas derived in this study with those formed through the dehydration of aluminum hydroxides. Cornelius et al. have suggested that the catalytic activity of transition aluminas is the result of “strained” oxygen bridges that form through the condensation of adjacent hydroxyl ions.³⁰ The condensation of hydroxyl ions in transition aluminas is analogous to the formation of nickel and oxygen vacancies in spinel. Therefore, the strain that develops in the defect spinel is anticipated to exhibit a comparable catalytic activity to γ -Al₂O₃.

The spinel structure becomes increasingly “defective” as the nickel loading increases in the calcined catalyst. The number of V_{Ni}^{''} and V_O^{''} is directly proportional to the nickel loading in the (Ni,Mg)-aluminate spinel prior to activation.(see chapter 2) Upon reduction, the formation of V_{Ni}^{''} and V_O^{''} in the

spinel structure results in a significant volume shrinkage marked by the sharp decrease in the lattice parameter. This shrinkage creates substantial strain in the defect spinel framework. A group of researchers studying the formation of metal-ceramic composites by partially reducing NiAl_2O_4 have reported similar observations.³¹⁻³³ The amount of strain is related to the volume shrinkage and, in turn, the strain is dependent on the nickel loading. The well known catalytic activity of transition aluminas exhibiting a so-called defect spinel structure suggests that the isostructural $\text{Mg}_{1-x}\text{Al}_2\text{O}_{4-x}$ formed in this study will exhibit significant activity, as well. The strained structure of $\text{Ni/MgAl}_2\text{O}_4$ catalysts may explain the results reported by Guo et al.¹¹ They report $\text{Ni/MgAl}_2\text{O}_4$ catalysts exhibit a higher activity and better stability relative to $\text{Ni}/\gamma\text{-Al}_2\text{O}_3$ and $\text{Ni/MgO-Al}_2\text{O}_3$ catalysts. The activity of $\text{Ni/MgAl}_2\text{O}_4$ catalysts increases with nickel loading from 1-15 wt % despite significant amounts of carbon deposition. The amount of carbon accumulated increases with the nickel loading. One explanation for this seemingly anomalous behavior is the MgAl_2O_4 support exhibits higher activity for methane reforming than the nickel particles. Carbon deposition onto the nickel surface would have little effect on the overall activity of the catalyst. Additionally, the increased strain associated with a higher nickel loading explains the enhanced activity of the catalyst.

3.6 Conclusion

$\text{Ni}_x\text{Mg}_{1-x}\text{Al}_2\text{O}_4$ spinel, where $x \leq 0.75$, are promising candidates for use as catalysts in methane reforming reactions. The incorporation of Mg into $\gamma\text{-Al}_2\text{O}_3$ stabilizes the spinel structure and suppresses its transition to alternative alumina polymorphs. The formation of increasingly more defective spinel structures with higher nickel contents implies that the spinel may contribute to the methane reforming activity. The catalytic activity of single phase non-stoichiometric $\text{Mg}_{1-x}\text{Al}_2\text{O}_{4-x}$ spinel should be assessed to elucidate its role in methane steam reforming reactions.

3.7 References

1. A. Al-Ubaid and E. E. Wolf, "Steam Reforming of Methane on Reduced Non-Stoichiometric Nickel Aluminate Catalysts," *Appl. Catal.*, **40** [1-2] 73-85 (1988).
2. A. S. Al-Ubaid, "Activity and Stability of Ni Spinel Catalysts in Water - Methane Reaction," *React. Kinet. Catal. Lett.*, **38** [2] 399-404 (1989).
3. A. Bhattacharyya and V. W. Chang, "CO₂ Reforming of Methane to Syngas: Deactivation Behavior of Nickel Aluminate Spinel Catalysts," *Catal. Deact. 1994, Proc. Int. Symp., 6th*, **88**, 207-13 (1994).
4. A. M. Gadalla and B. Bower, "The Role of Catalyst Support on the Activity of Nickel for Reforming Methane with CO₂," *Chem. Eng. Sci.*, **43** [11] 3049-62 (1988).
5. J. Guo, H. Lou, and X. Zheng, "The Deposition of Coke from Methane on a Ni/MgAl₂O₄ Catalyst," *Carbon*, **45** [6] 1314-21 (2007).
6. K. Y. Koo, H.-S. Roh, Y. T. Seo, D. J. Seo, W. L. Yoon, and S. B. Park, "Coke Study on MgO-Promoted Ni/Al₂O₃ Catalyst in Combined H₂O and CO₂ Reforming of Methane for Gas to Liquid (GTL) Process," *Appl. Catal. A*, **340** [2] 183-90 (2008).
7. C. Otero Areán, M. Peñarroya Mentrut, A. J. López López, and J. B. Parra, "High Surface Area Nickel Aluminate Spinels Prepared by a Sol-Gel Method," *Colloids Surf., A*, **180** [3] 253-8 (2001).
8. L. Zhou, M. Sakurai, and H. Kameyama, "A Novel Catalyst with Plate-Type Anodic Alumina Supports, Ni/NiAl₂O₄/γ-Al₂O₃/Alloy, for Steam Reforming of Methane," *Appl. Catal. A*, **347** [2] 200-7 (2008).
9. J. R. Rostrup-Nielsen, "Catalytic Steam Reforming," pp. 1-117 in *Catalysis: Science and Technology*, Vol. 5. Edited by J. R. Anderson and M. Boudart. Springer-Verlag, Berlin, 1984.
10. Z. X. Cheng, X. G. Zhao, J. L. Li, and Q. M. Zhu, "Role of Support in CO₂ Reforming of CH₄ over a Ni/γ-Al₂O₃ Catalyst," *Appl. Catal. A*, **205** [1-2] 31-6 (2001).
11. J. Guo, H. Lou, H. Zhao, D. Chai, and X. Zheng, "Dry Reforming of Methane over Nickel Catalysts Supported on Magnesium Aluminate Spinels," *Appl. Catal. A*, **273** [1-2] 75-82 (2004).

12. N. Sahli, C. Petit, A. C. Roger, A. Kiennemann, S. Libs, and M. M. Bettahar, "Ni Catalysts from NiAl₂O₄ Spinel for CO₂ Reforming of Methane," *Catal. Today*, **113** [3-4] 187-93 (2006).
13. H. S. Benggaard, J. K. Nørskov, J. Sehested, B. S. Clausen, L. P. Nielsen, A. M. Molenbroek, and J. R. Rostrup-Nielsen, "Steam Reforming and Graphite Formation on Ni Catalysts," *J. Catal.*, **209** [2] 365-84 (2002).
14. D. L. Trimm, "Catalysts for the Control of Coking During Steam Reforming," *Catal. Today*, **49** [1-3] 3-10 (1999).
15. K. Wefers and C. Misra, *Oxides and Hydroxides of Aluminum*; pp. 1-92. Alcoa Laboratories, Pittsburgh, 1987.
16. J. H. De Boer and B. C. Lippens, "Studies on Pore Systems in Catalysts II. The Shapes of Pores in Aluminum Oxide Systems," *J. Catal.*, **3** [1] 38-43 (1964).
17. B. C. Lippens and J. H. D. Boer, "Studies on Pore Systems in Catalysts III. Pore-Size Distribution Curves in Aluminum Oxide Systems," *J. Catal.*, **3** [1] 44-9 (1964).
18. Topas V3: General Profile and Structure Analysis Software for Powder Diffraction Data, [Computer Program] Bruker AXS, Karlsruhe, Germany, 2005.
19. F. Colin, "Des Phases Formees Au Cours De La Reduction De Certains Oxydes Mixtes nAl₂O₃:MO," *Rev. Int. Hautes Temp. Refract.*, **5** [4] 267-83 (1968).
20. A. Navrotsky, B. A. Wechsler, K. Geisinger, and F. Seifert, "Thermochemistry of Magnesium Aluminate-Aluminum Oxide (MgAl₂O₄-Al_{8/3}O₄) Defect Spinel," *J. Am. Ceram. Soc.*, **69** [5] 418-22 (1986).
21. A. F. Henriksen and W. D. Kingery, "The Solid Solubility of Sc₂O₃, Al₂O₃, Cr₂O₃, SiO₂ and ZrO₂ in MgO," *Ceramurgia Int.*, **5** [1] 11-7 (1979).
22. B. Hallstedt, "Thermodynamic Assessment of the System MgO-Al₂O₃," *J. Am. Ceram. Soc.*, **75** [6] 1497-507 (1992).
23. I. Levin and D. Brandon, "Metastable Alumina Polymorphs: Crystal Structures and Transition Sequences," *J. Am. Ceram. Soc.*, **81** [8] 1995-2012 (1998).

24. E. M. Moroz, O. A. Kirichenko, A. V. Ushakov, and E. A. Levitski, "Phase Composition of Aluminum Oxides Promoted by Cr, Cu, and Ni Additives," *React. Kinet. Catal. Lett.*, **28** [9] 9-15 (1985).
25. Z. Zhang, E. Üstündag, and S. L. Sass, "Partial Reduction of NiAl₂O₄ - Mechanism and the Influence of Doping," *Mater. Res. Soc. Symp. Proc.*, **398**, 489-94 (1996).
26. S. J. Wilson, "Phase Transformations and Development of Microstructure in Boehmite-Derived Transition Aluminas," *Proc. Br. Ceram. Soc.*, **28**, 281-94 (1979).
27. S. J. Wilson, "The Dehydration of Boehmite, γ -AlOOH, to γ -Alumina," *J. Solid State Chem.*, **30** [2] 247-55 (1979).
28. J. T. Richardson, R. M. Scates, and M. V. Twigg, "X-Ray Diffraction Study of the Hydrogen Reduction of NiO/ α -Al₂O₃ Steam Reforming Catalysts," *Appl. Catal. A*, **267** [1-2] 35-46 (2004).
29. E. Üstündag, R. Subramanian, R. Dieckmann, and S. L. Sass, "In Situ Formation of Metal-Ceramic Microstructures in the Ni---Al---O System by Partial Reduction Reactions," *Acta Metall. Mater.*, **43** [1] 383-9 (1995).
30. E. B. Cornelius, T. H. Milliken, G. A. Mills, and A. G. Oblad, "Surface Strain in Oxide Catalysts-Alumina," *J. Chem. Phys.*, **59**, 809-13 (1955).
31. E. Üstündag, B. Clausen, and M. A. M. Bourke, "Neutron Diffraction Study of the Reduction of NiAl₂O₄," *Appl. Phys. Lett.*, **76** [6] 694-6 (2000).
32. B. Clausen, E. Ustundag, and M. A. M. Bourke, "Investigation of the Reduction of NiAl₂O₄," *Adv. X-Ray Anal.*, **44**, 32-7 (2001).
33. E. Üstündag, Z. Zhang, M. L. Stocker, P. Rangaswamy, M. A. M. Bourke, S. Subramanian, K. E. Sickafus, J. A. Roberts, and S. L. Sass, "Influence of Residual Stresses on the Evolution of Micro-Structure During the Partial Reduction of NiAl₂O₄," *Mater. Sci. Eng., A*, **238** [1] 50-65 (1997).

3.8 Tables

Table VI. Reaction Temperatures and Times for the Spinel Series $\text{Ni}_x\text{Mg}_{1-x}\text{Al}_2\text{O}_4$, where $0 \leq x \leq 1$, in 300 torr of H_2

Temperature (°C)	Time (hrs)
650	94
700	51
750	29
800	24
850	24
900	12
950	12
1000	12

3.9 Figures

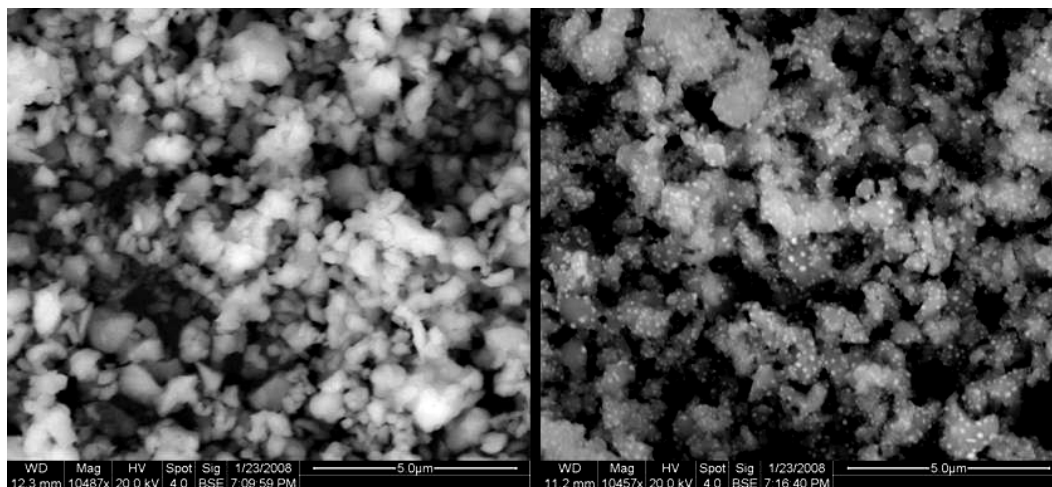


Figure 24. A SEM micrograph illustrating the formation of metallic nickel crystallites evenly dispersed on the surface of spinel. This sample is $\text{Ni}_{0.5}\text{Mg}_{0.5}\text{Al}_2\text{O}_4$ following exposure to H_2 at 950°C for 12 hrs.

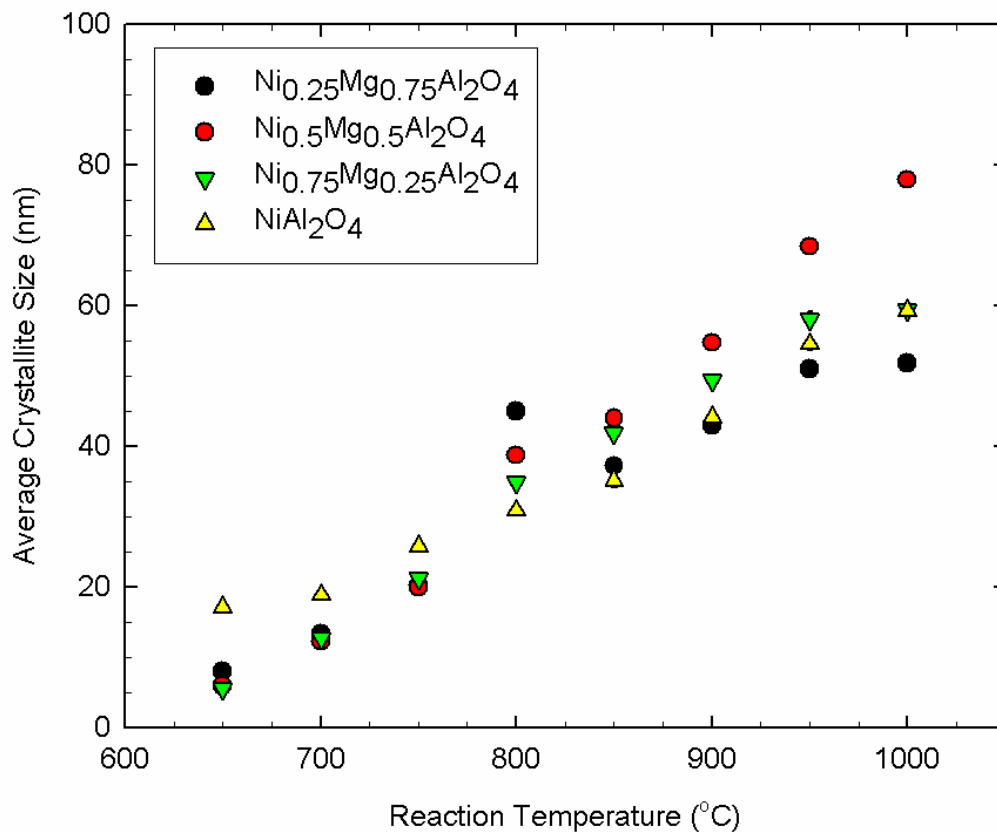


Figure 25. A plot of the average crystallite size for nickel at the specified reaction temperatures. The error bars are smaller than the data points.

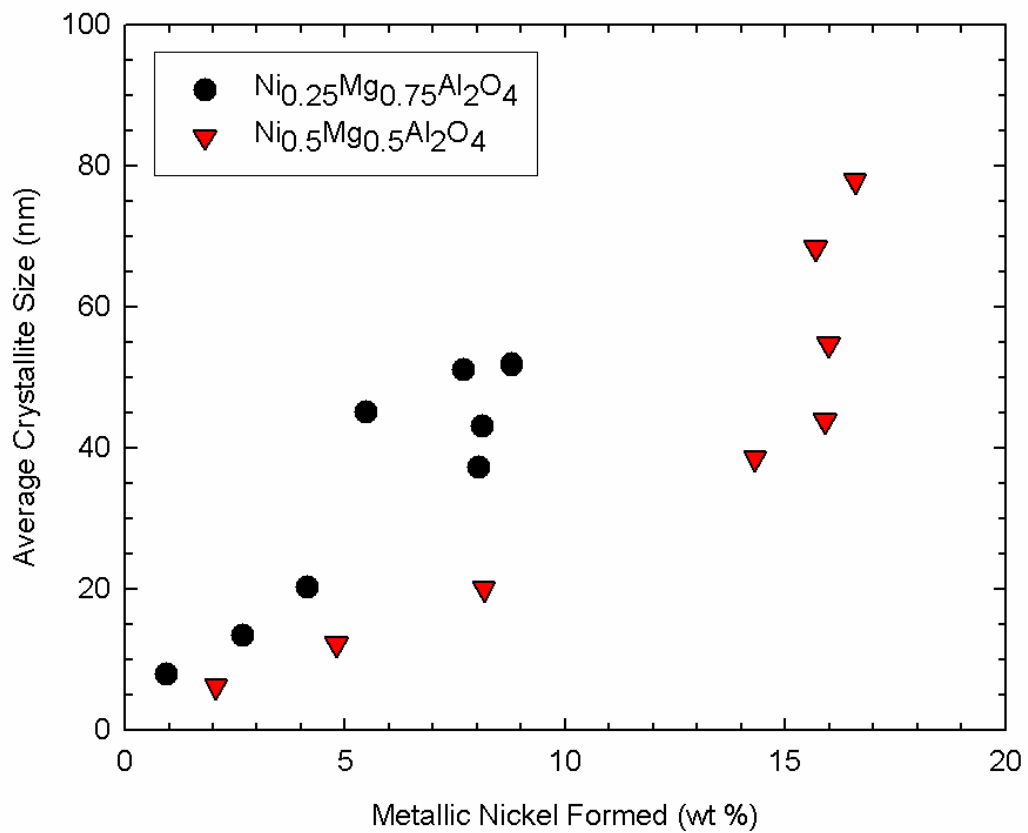


Figure 26. The relationship between the average crystallite size and the weight percent of metallic nickel formed for the spinel compositions $\text{Ni}_{0.25}\text{Mg}_{0.75}\text{Al}_2\text{O}_4$ and $\text{Ni}_{0.5}\text{Mg}_{0.5}\text{Al}_2\text{O}_4$. The error bars are smaller than the data points.

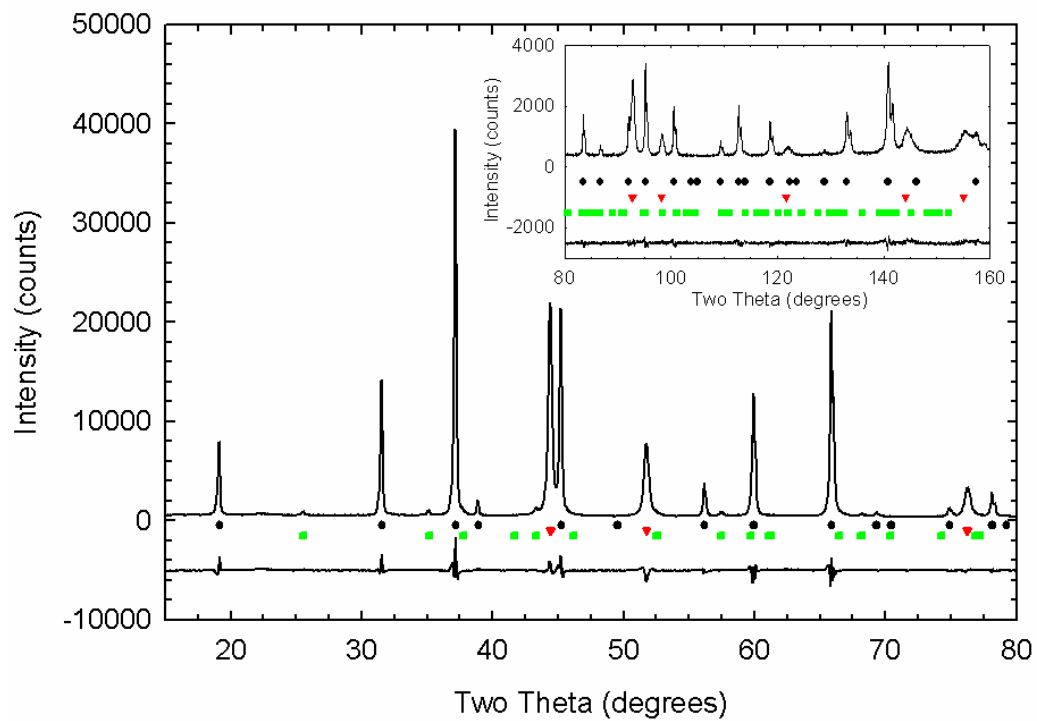


Figure 27. An example of the Rietveld refinement of X-ray diffraction data used to calculate both the weight fractions of the products formed and the average crystallite size of metallic nickel formed for $\text{Ni}_{0.25}\text{Mg}_{0.75}\text{Al}_2\text{O}_4$ reacted with H_2 at 850°C . (GOF=1.83, Rwp=8.61)

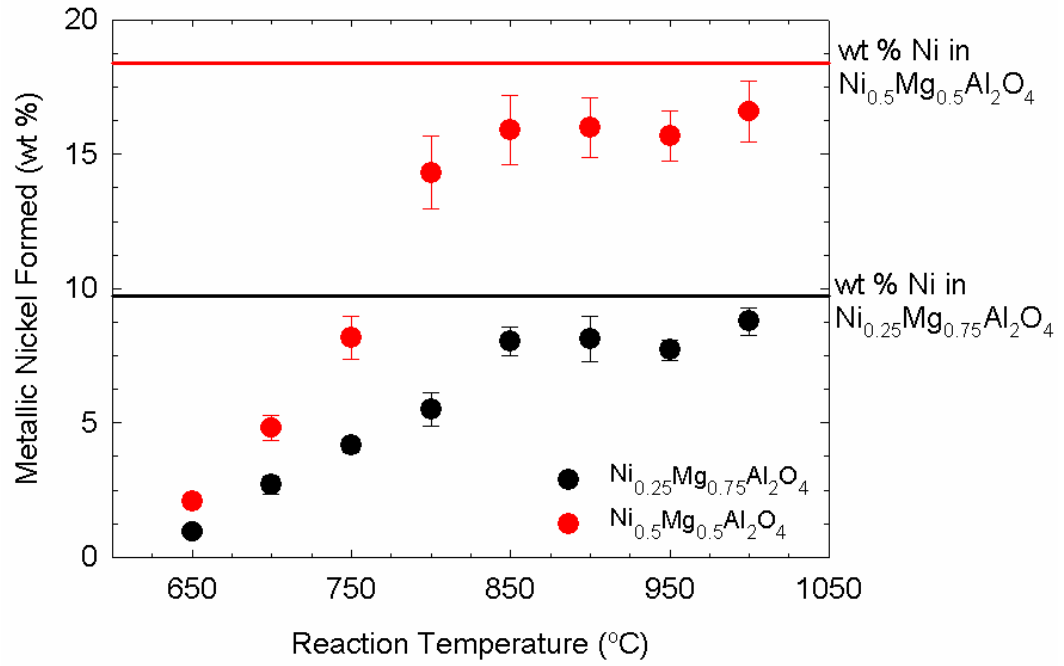


Figure 28. The weight percent of metallic nickel formed during reaction with hydrogen at the specified reaction temperature.

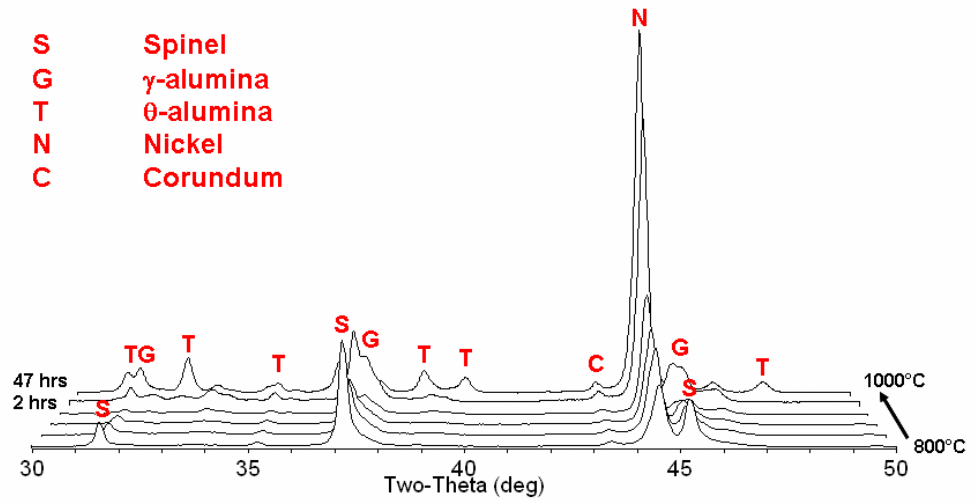


Figure 29. The reaction products for NiAl_2O_4 with H_2 at the indicated temperatures.

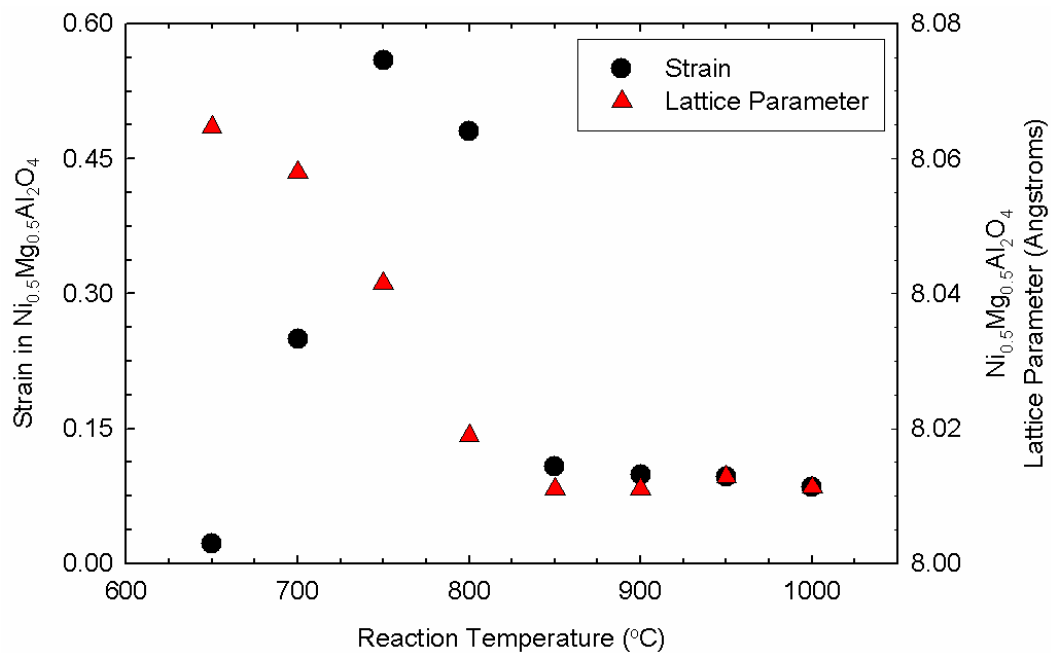


Figure 30. The change in lattice parameter as a function of reaction temperature for $\text{Ni}_{0.5}\text{Mg}_{0.5}\text{Al}_2\text{O}_4$. The error bars are smaller than the data points.

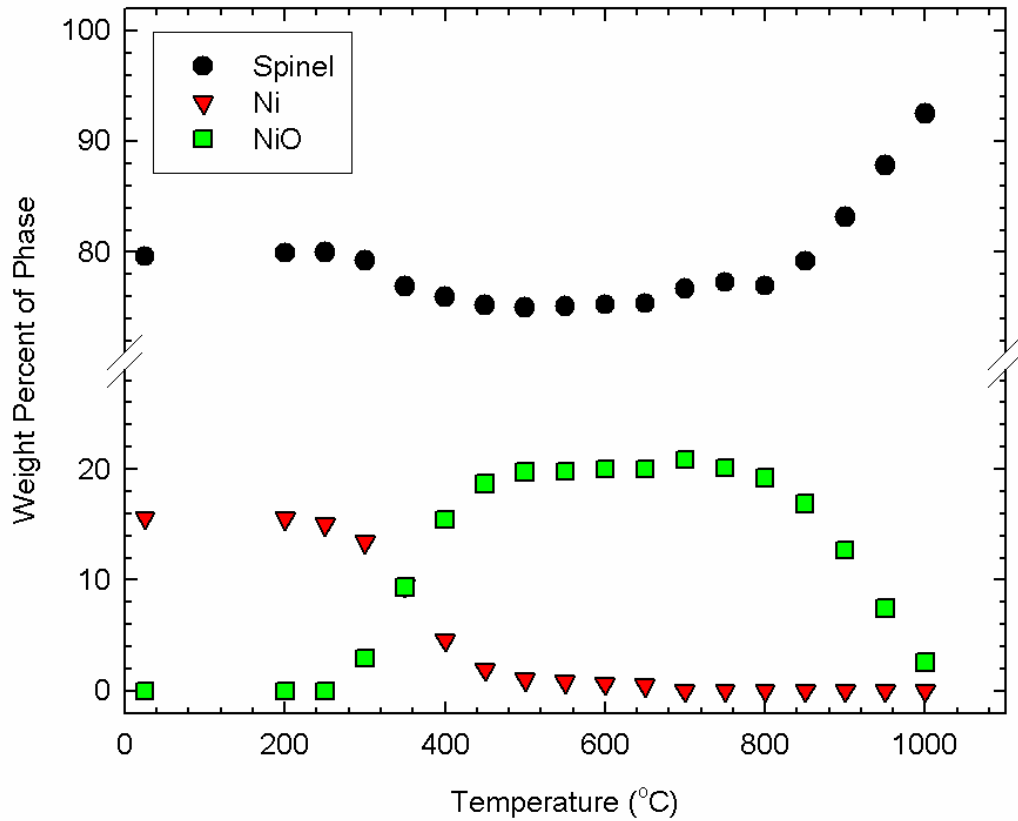


Figure 31. The phase transformation sequence during the re-oxidation of Ni supported on non-stoichiometric spinel. X-ray data is collected after 1 hr dwell at each temperature. The error bars are smaller than the data points.

Linking spinel glass-ceramics to single phase spinel

Prior to the single phase spinel study, I demonstrated that the hydrogen reaction with NiO MgO Al₂O₃ SiO₂ glass-ceramics is complicated by the presence of multiple phases. To simplify the analysis, single phase [Ni,Mg]Al₂O₄ solid solutions were synthesized and reacted with hydrogen. These results are presented in chapters 2 & 3. The stability limit for the Ni_xMg_{1-x}Al₂O₄ spinel is determined to be 0.5<x<0.75. In chapter 1, the composition of the spinel phase crystallizing from NiO MgO 2Al₂O₃ 5SiO₂ glasses is determined to be Ni_{0.5}Mg_{0.5}Al₂O₄. This spinel phase is predicted based on the single phase study to be stable following the complete reaction with hydrogen at temperatures up to 1000°C. The following in situ experiment demonstrates the connection between the results presented in chapters 1 through 3.

The high temperature X-ray diffraction pattern for NiO MgO 2Al₂O₃ 5SiO₂ glass-ceramic reacted in H₂ at 1000°C for 12 hrs is shown in Figure 32. The formation of metallic nickel reaches a maximum after 4 hrs. The intensities of the spinel diffraction lines decrease simultaneously with increasing nickel intensity. Concurrently, the spinel intensity reaches a minimum value and the nickel intensity reaches a maximum value. This correlation suggests that the nickel is reducing from the spinel phase, and the non-stoichiometric spinel in the glass-ceramic is stable in dry hydrogen up to 1000°C. There is no sign of additional decomposition products forming and the spinel intensity reaches an equilibrium value following the complete reaction with hydrogen at 1000°C. The reaction of the spinel glass-ceramic with hydrogen is in agreement with the stability studies for the single phase spinel samples in hydrogen.

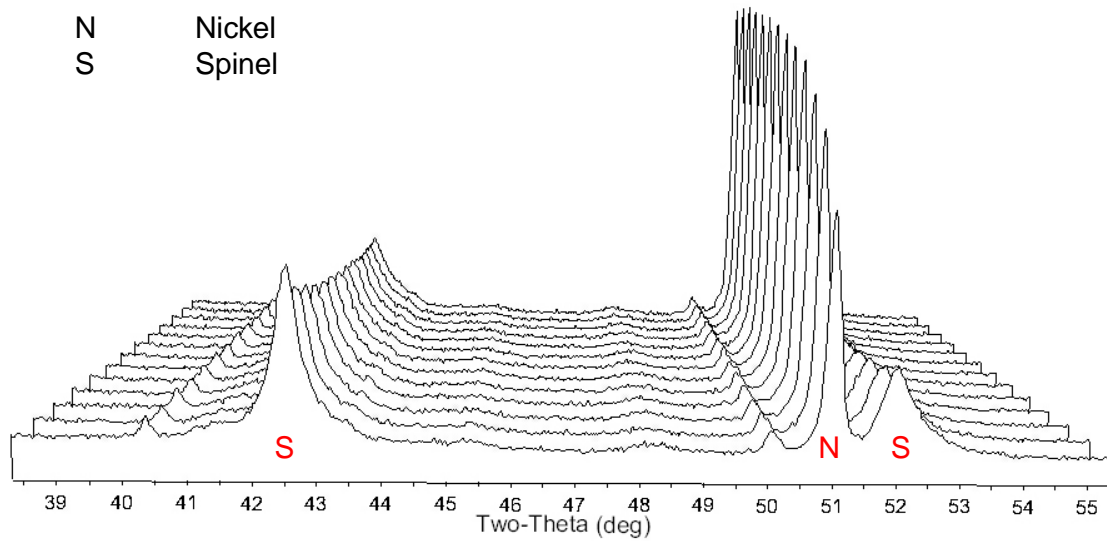


Figure 32. HTXRD pattern for NiO MgO 2Al₂O₃ 5SiO₂ glass-ceramic reacted with H₂ at 1000°C in flowing 4H₂-96N₂. The scans are recorded in 1 hr intervals.

Appendix 1: NiO MgO Al₂O₃ SiO₂ Glasses

A1.1 Introduction

The ideal design for a gas separation membrane is a thick film (~0.1mm) supported on a macroporous body. To achieve a continuous, pinhole-free film, the powdered glass needs to flow prior to crystallization. This chapter investigates the effects of NiO-MgO, Al₂O₃ and SiO₂ components on the glass viscosity and the crystallization behavior of NiO-MgO-Al₂O₃-SiO₂ glasses. A qualitative interpretation of the glass viscosity is based on both the glass transition temperature (DTA) and softening behavior of powder samples (HSM). Glass crystallization temperatures are determined from DTA data.

The NiO-MgO-Al₂O₃-SiO₂ glass compositions are plotted in Figure 33 along with the approximate cordierite phase field. The NiO/MgO ratio is fixed at 0.6 (mol %) or 1.85 (wt %) over this compositional range. This ratio is chosen with the assumption that the [Ni,Mg]-aluminate spinel crystallizing from these glasses will have a composition with a Ni/Mg ratio ~ 0.6. The results presented in chapter 1 indicate that the composition of the spinel phase crystallizing in stoichiometric cordierite glasses correlates to the initial glass composition. The importance of this ratio is to ensure the stability of the Ni_xMg_{1-x}Al₂O₄ spinel following reaction with hydrogen while maximizing the amount of nickel reduced – maximizing the amount of nickel reduced from spinel will maximize the porosity in the glass-ceramic membrane. In chapter 2, the stability limit of non-stoichiometric Mg_{1-x}Al₂O_{4-x} spinel is determined to be between 0.5 ≤ x ≤ 0.75 and is reported to be ~0.71.¹

A1.2 Experimental Procedures

NiO-MgO-Al₂O₃-SiO₂ glasses having a composition of 8.3-12.0 mol % NiO, 13.8-21.7 mol % MgO, 11.7-19.6 mol % Al₂O₃, and 51.1-60.4 mol % SiO₂ were batched from reagent grade Mg(OH)₂, NiO, Al₂O₃ and SiO₂. Twenty five gram batches were mixed in deionized water and dried prior to melting. The dried batches were reacted at 1600°C for 4 hrs in a Pt crucible. The melts were quenched into DI water at the end of 4 hrs.

Differential thermal analysis measurements were recorded using a DuPont 1600 DTA in static air at a heating rate of 50 K/min. Samples were contained in alumina pans and alumina powder was used as the reference material. The sample sizes ranged from 20 to 35 mg. The analysis of each composition was repeated three times.

The flow behavior of powdered glasses having a particle size < 45 microns was analyzed using hot stage microscopy (HSM). Images of 3 mm cylindrical pellets were recorded every 10°C between 700°C and 1200°C at a heating rate of 10 K/min.

A1.3 Results and discussion

XRD patterns for the DTA samples of each glass were recorded to identify the phases that correspond to the exotherms in the thermal analysis (not shown). All glasses crystallize to form β -quartz at the surface and spinel in the bulk. The exotherms for the bulk crystallization (spinel) are determined from DTA data of bulk samples, and the surface crystallization temperatures are determined from DTA data of ball milled powder. The glass transition temperature and crystallization temperatures for the glasses are reported in Table VII.

It is important to recall that the NiO and MgO contents are correlated because the NiO/MgO ratio is fixed at 0.6 for all glass compositions. Therefore, the following data will be presented as the combined effect of NiO-MgO on the glass properties.

A1.3.1 Glass transition temperature

The effects of NiO-MgO, Al_2O_3 and SiO_2 on the glass transition temperature are shown in Figure 34, Figure 35, and Figure 36, respectively. The glass transition temperature decreases with increasing NiO-MgO content and increases with increasing Al_2O_3 content. The SiO_2 content appears to have little or no effect on the glass transition temperature.

A1.3.2 Crystallization temperatures

The effects of NiO-MgO, Al₂O₃ and SiO₂ on the spinel and β-quartz crystallization temperatures are shown in Figure 37, Figure 38, and Figure 39, respectively. The trends in the spinel crystallization behavior are the same as the trends observed in the glass transition behavior. NiO-MgO additions lower the spinel crystallization temperature, while Al₂O₃ additions increase the crystallization temperature. One notable difference in the trends for the glass transition temperature and spinel crystallization temperature is less scatter in the crystallization temperature data than the glass transition temperature data. The thermal history of the glass will significantly impact the measured glass transition temperature.² The glasses used in this study were quenched into DI water which may lead to variations in the thermal history between and within samples.

The degree to which the β-quartz crystallization temperature is affected by compositional changes for these glasses is less than the effect on the spinel crystallization temperature. The β-quartz crystallization temperature has a compositional dependence that is in slight contrast to the relationship for the spinel crystallization temperature with the glass composition. The NiO-MgO additions result in a sharp decrease in the β-quartz crystallization temperature between 22 mol % and 26 mol % NiO-MgO. For 26 mol%<NiO-MgO<35 mol%, the β-quartz crystallization temperature is independent of the NiO-MgO content. The sharp decrease in β-quartz crystallization temperature corresponds to 17 mol%<Al₂O₃<20 mol % and 57 mol %<SiO₂<58 mol %. The sudden change in the β-quartz crystallization temperature may be related to a change in the glass microstructure such as glass-in-glass phase separation. NiO MgO 2Al₂O₃ 5SiO₂ glasses having at least 5 wt % NiO are reported to phase separate.³

The β-quartz and spinel crystallization temperatures were plotted together to show that the spinel crystallization temperature is lower than the β-quartz crystallization temperature for the compositions with the highest NiO-MgO contents, and the spinel T_c > β-quartz T_c for low NiO-MgO contents. The compositions for which spinel T_c < β-quartz T_c are highlighted in Figure 33 as

blue-diamonds. The composition which exhibits the highest β -quartz crystallization temperature is indicated as a star in Figure 33. This composition has the lowest NiO-MgO and highest Al_2O_3 content both of which lead to a higher glass transition temperature and crystallization temperature.

A1.3.3 Hot stage microscope (HSM)

An example set of HSM data for 11.9NiO 19.8MgO 11.7 Al_2O_3 56.6 SiO_2 glass recorded at 10 K/min is shown in Figure 40. The onset and inflection temperatures corresponding to softening of the NiO-MgO- Al_2O_3 - SiO_2 glasses are reported in Table VII. These temperatures are interpreted as the onset and minimum for the derivative curve, respectively. None of the powders showed any signs of significant softening or sintering.

The crystallization of these glasses will inhibit the flow and sintering of the glass-ceramic particles. A decrease in the glass viscosity (T_g) may be achieved by increasing the NiO-MgO content or decreasing the Al_2O_3 content, however, these compositional changes lead to a reduction in the crystallization temperatures. β -quartz crystallization is expected to be the main limiting factor in the sintering of the glass particles because it nucleates at the surface. Therefore, it is desirable to maximize the difference between the softening and β -quartz crystallization temperatures. The 13.1NiO 21.7MgO 14.2 Al_2O_3 51.1 SiO_2 glass has the largest difference between the T_g and β -quartz T_c , however, the spinel crystallization temperature is lower than the β -quartz crystallization temperature for this composition. The spinel crystallization in the bulk may effectively increase the viscosity of the glass over this temperature range thus inhibiting the sintering of the glass powder.

A1.4 Conclusions

All glasses crystallize to spinel in the bulk and β -quartz at the surface. The following compositional effects are observed:

- NiO-MgO additions decrease the T_g and T_c for both spinel and β -quartz
- Al_2O_3 additions increase the T_g and T_c for both spinel and β -quartz

- SiO₂ additions do not significantly impact T_g and T_c for both spinel and β-quartz.

None of these glasses are good candidates for tape casting a thick film. A decrease in the glass viscosity is accompanied with decreasing crystallization temperatures for this composition space.

A1.5 Suggestions

- Repeat the HSM measurements with a dwell at the inflection temperature to achieve sintering of the glass powder.
- Extend the composition space to higher NiO-MgO contents and lower SiO₂ contents. Though decreasing the Al₂O₃ content is effective at lowering the glass viscosity, it will limit the phase fraction of spinel that may crystallize in the bulk.
- Consider alternative methods to produce a thick film such as vapor deposition.

A1.6 References

1. A. Navrotsky, B. A. Wechsler, K. Geisinger, and F. Seifert, "Thermochemistry of Magnesium Aluminate-Aluminum Oxide (MgAl_2O_4 - $\text{Al}_{8/3}\text{O}_4$) Defect Spinel," *J. Am. Ceram. Soc.*, **69** [5] 418-22 (1986).
2. J. E. Shelby, *Introduction to Glass Science and Technology*; p. 155. Royal Society of Chemistry, Cambridge, 1997.
3. G. H. Beall and J. E. Pierson, Corning Incorporated, "Nickel Aluminosilicate Glass-Ceramics," U.S. 5,352,638, February 22, 1994.

A1.7 Tables

Table VII. NiO-MgO-Al₂O₃-SiO₂ Glass Properties

NiO mol %	MgO mol %	Al ₂ O ₃ mol %	SiO ₂ mol %	T _g (°C)	T _g e.s.d (°C)	T _c - bulk (°C)	T _c e.s.d (°C)	T _c - powder (°C)	HSM - onset (°C)	HSM - inflection (°C)	T _g - T _c quartz (°C)
8.3	13.8	17.5	60.4	793	12	1007	2	994	-	-	-
11.9	19.8	11.7	56.6	767	6	919	0	945	810	900	135
8.4	14.0	19.6	58.0	794	10	1010	3	995	900	960	95
12.0	19.9	14.0	54.0	767	3	935	3	949	820	900	129
13.1	21.7	14.2	51.1	767	2	927	2	957	780	895	177
11.0	18.2	16.5	54.4	774	1	961	2	950	800	880	150
9.7	16.0	16.8	57.5	800	8	988	2	960	810	880	150
11.0	18.2	14.4	56.4	781	3	953	2	960	810	895	150
10.9	18.1	17.8	53.2	790	4	970	1	956	810	885	146

A1.8 Figures

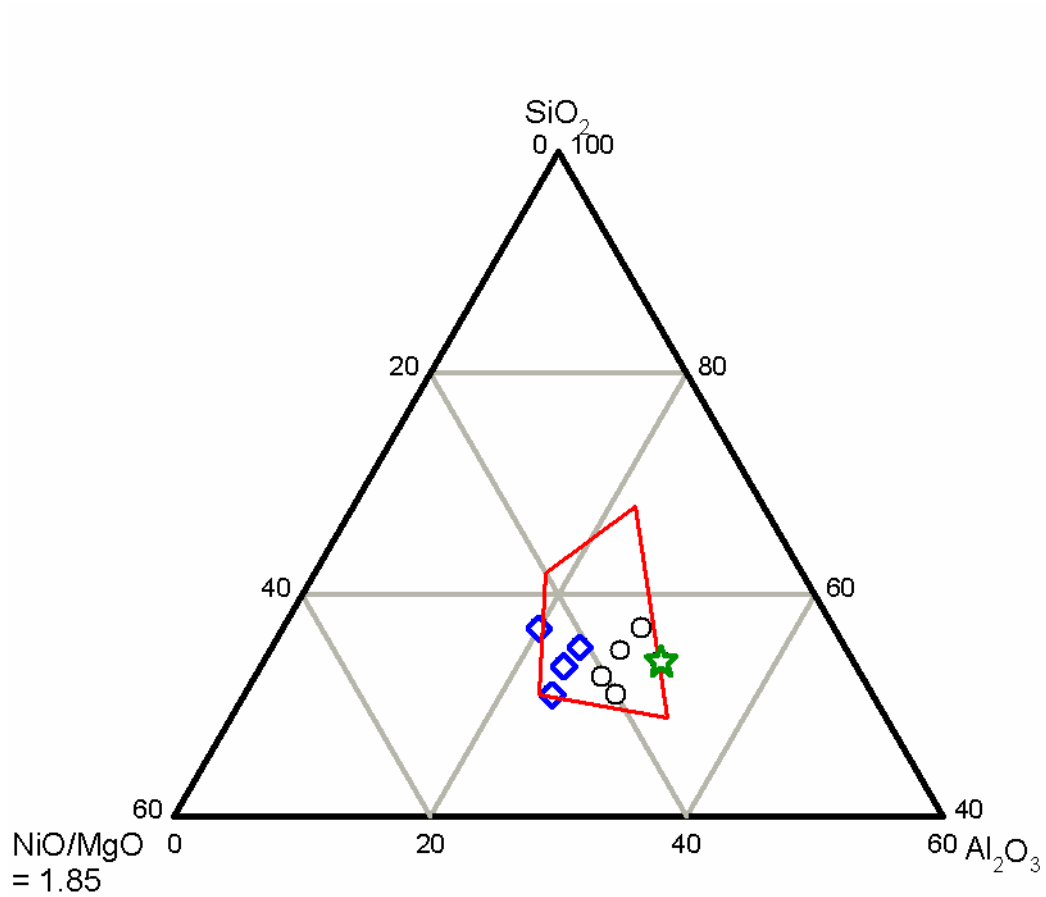


Figure 33. The NiO-MgO-Al₂O₃-SiO₂ glass compositions (wt %) for which the viscosity and crystallization behavior are analyzed. The red outline indicates the approximate cordierite phase field in the MgO-Al₂O₃-SiO₂ system.

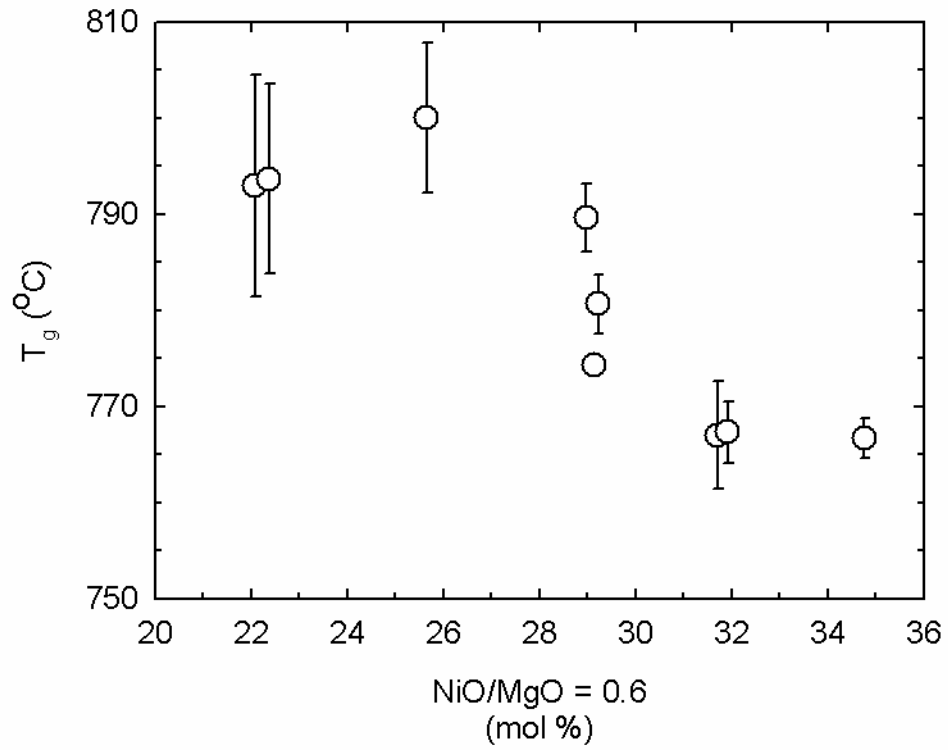


Figure 34. The effect of NiO-MgO on the glass transition temperature in NiO-MgO-Al₂O₃-SiO₂ glasses.

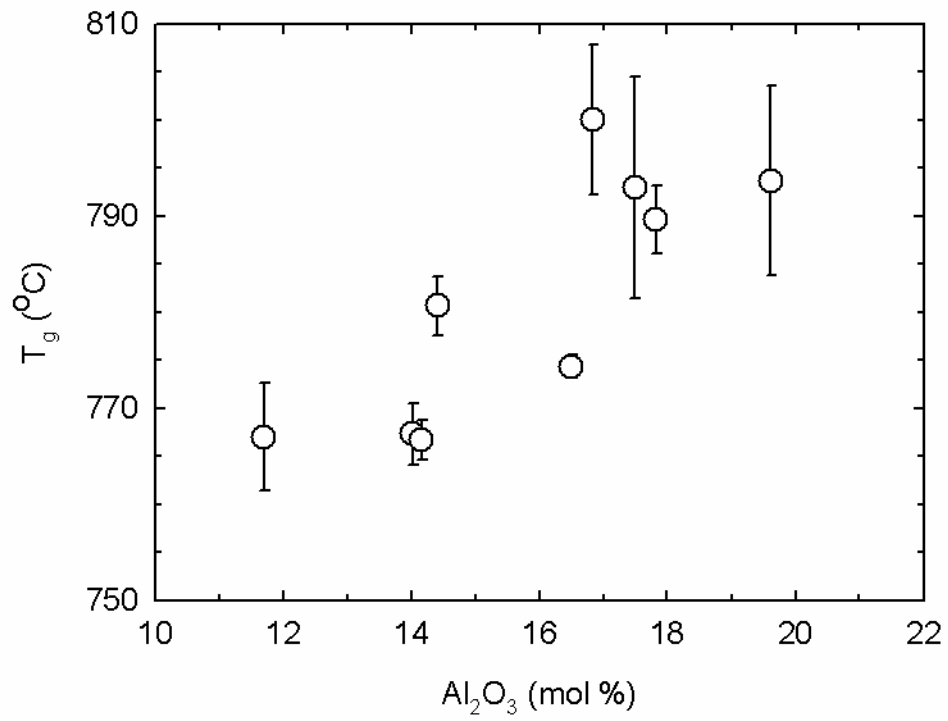


Figure 35. The effect of Al₂O₃ on the glass transition temperature in NiO-MgO-Al₂O₃-SiO₂ glasses.

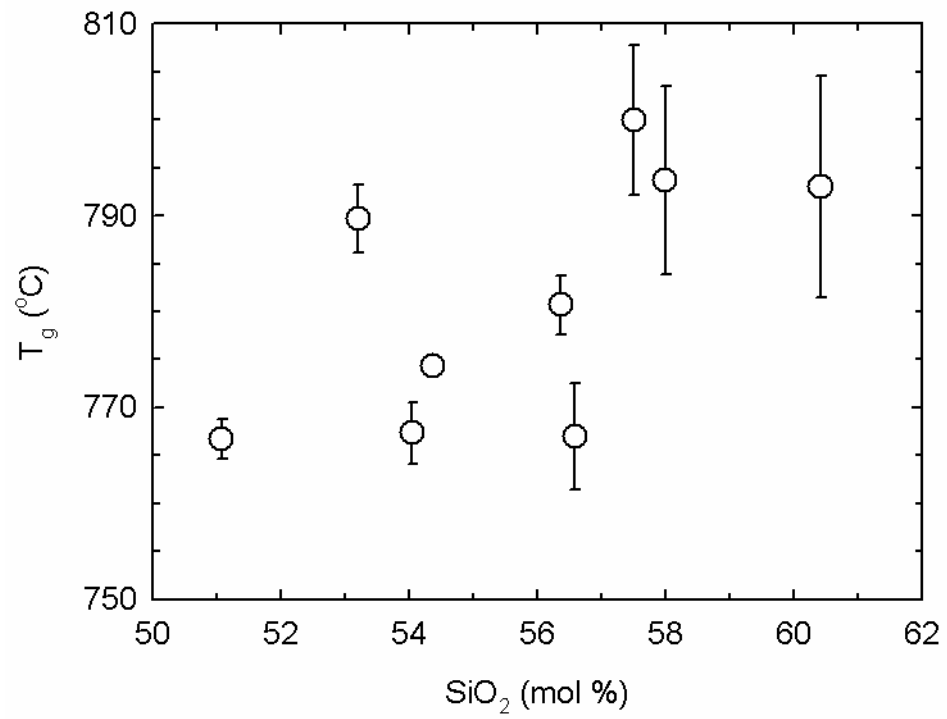


Figure 36. The effect of SiO₂ on the glass transition temperature in NiO-MgO-Al₂O₃-SiO₂ glasses.

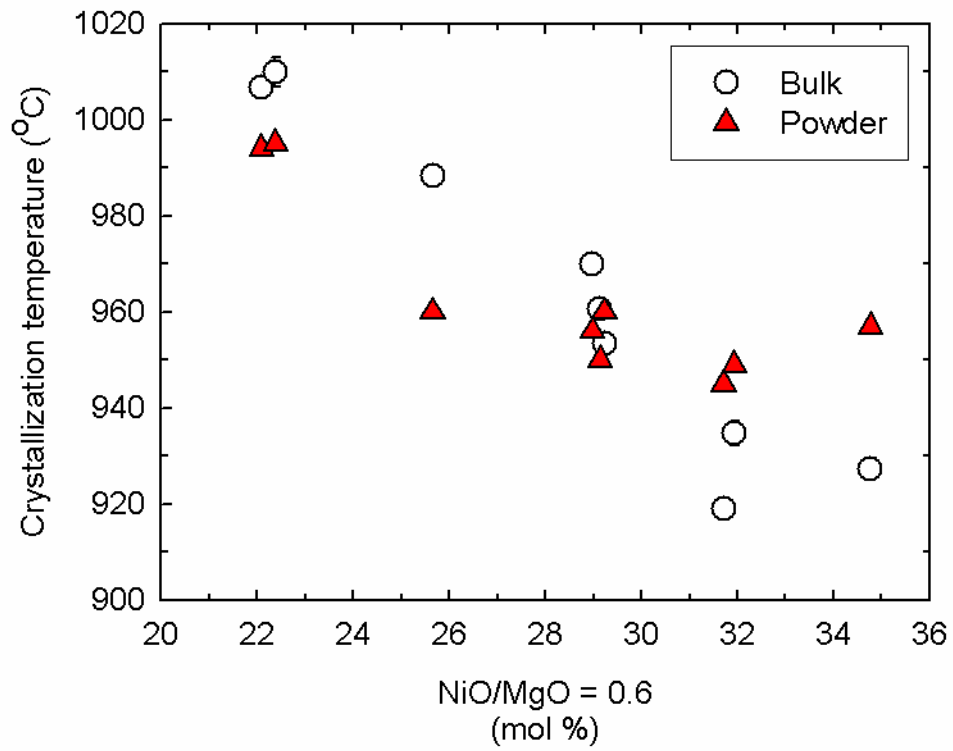


Figure 37. The effect of NiO-MgO on the crystallization temperatures for spinel and β -quartz in NiO-MgO-Al₂O₃-SiO₂ glasses.

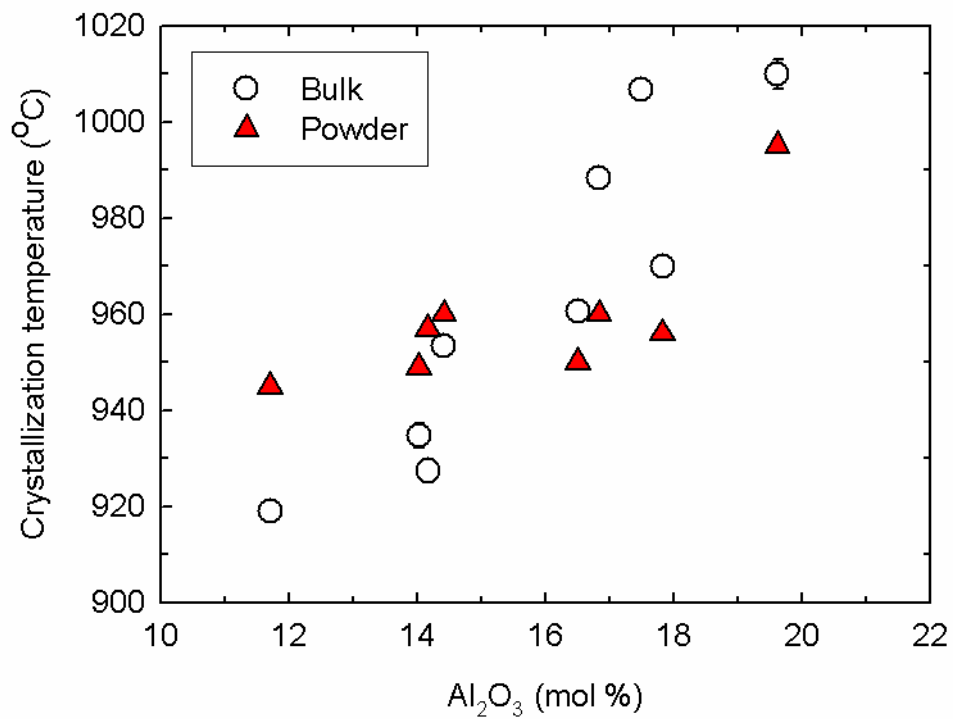


Figure 38. The effect of Al₂O₃ on the crystallization temperatures for spinel and β-quartz in NiO-MgO-Al₂O₃-SiO₂ glasses.

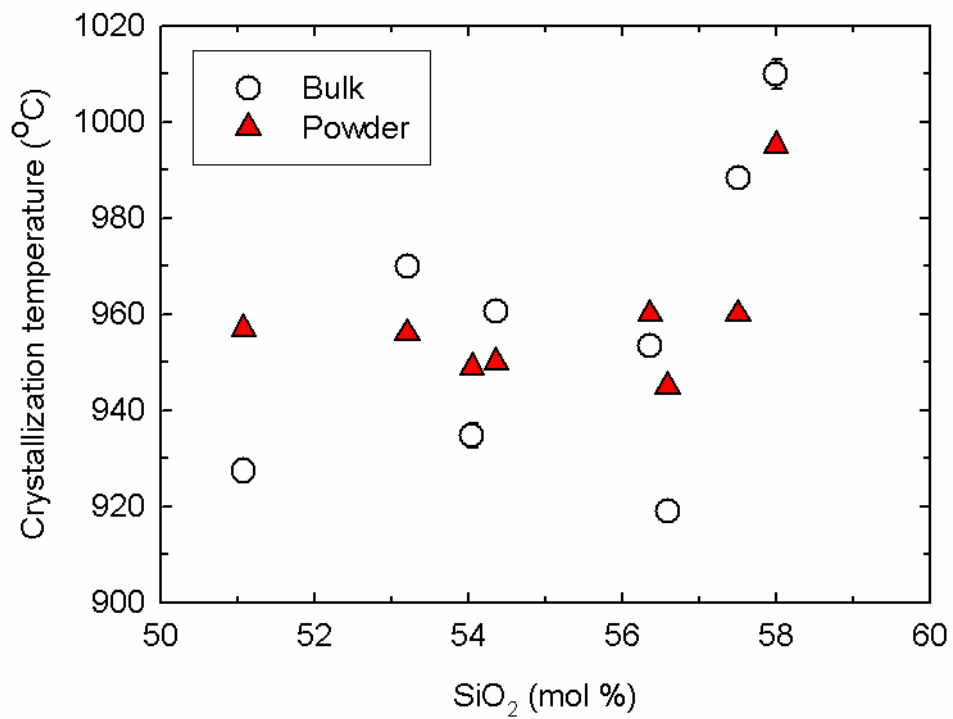


Figure 39. The effect of SiO₂ on the crystallization temperatures for spinel and β -quartz in NiO-MgO-Al₂O₃-SiO₂ glasses.

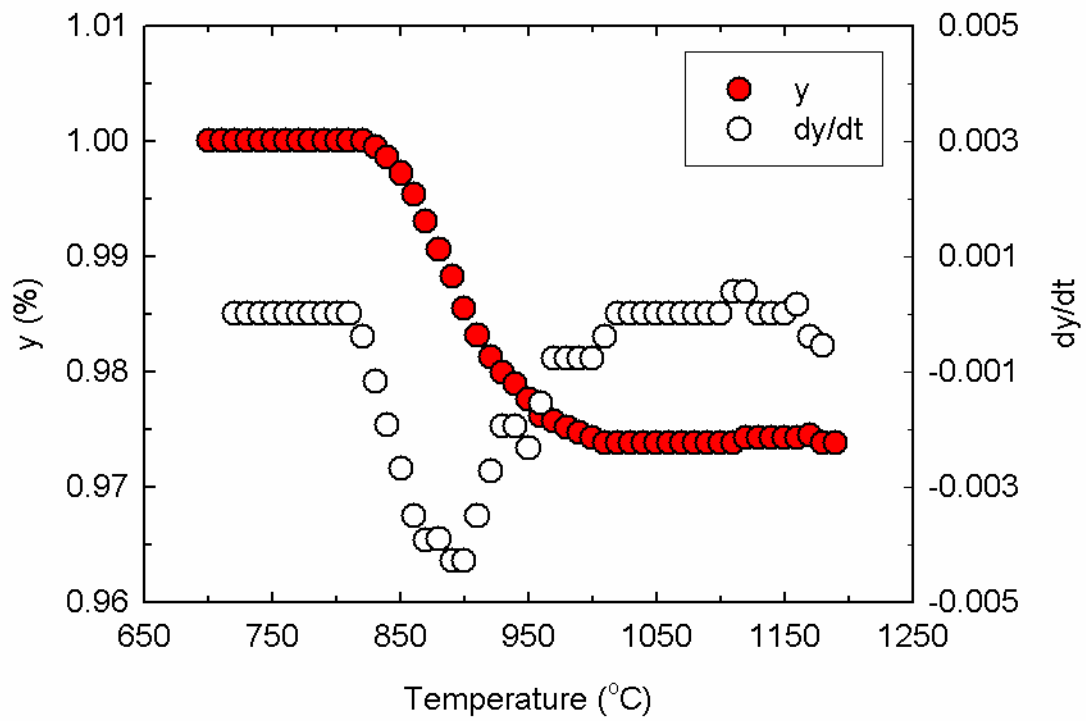


Figure 40. HSM data for 11.9NiO 19.8MgO 11.7Al₂O₃ 56.6SiO₂ glass recorded at 10 K/min.

Appendix 2: Measuring high temperature permeability

A2.1 Pressure-drop technique

The solution for gas permeability (molecules/cm-s-atm) through a plate is given by:

$$K = \left(\frac{VL}{ART} \right) \left[\frac{\ln(P/P^*)}{t} \right]$$

where V is the volume of gas (cm³), L is thickness of the plate (cm), A is the area of the plate through which gas flows (cm²), R is the gas constant, T is the absolute temperature (K), and t is the time (s) required for the pressure to drop from P to P*.¹ The values V, L, A, R, and T are all constant for a given set of experimental conditions. Measurement of P as a function of time in isothermal conditions is used to calculate the permeability. The slope of the regression line for a plot of ln(P/P*) vs t is equal to the permeability times the constant (VL/ART).

A2.2 High temperature permeability apparatus

A schematic diagram for the measurement of high temperature permeability through a plate is shown in Figure 41. The system is comprised of a 50 cm³ volume standard, a mechanic roughing pump, a sealed alumina tube, an absolute pressure gauge (capacitance manometer), a vacuum gauge, a thermocouple, and a gas cylinder. The volume of the high pressure side of the system is calibrated using the volume standard and applying the ideal gas law. A solid metal plate is used in place of the sample to calibrate the system volume.

The sample holder is shown in Figure 42. The sample holder is machined stainless steel with a 3/4" diameter raised bevel. A graphite gasket is placed between the raised bevel and the sample to form a seal. The graphite gasket is cut from graphite foil.

A2.3 References

1. J. E. Shelby, *Gas Diffusion in Solids and Melts*. ASM International, Materials Park. OH, 1996.

A2.4 Figures

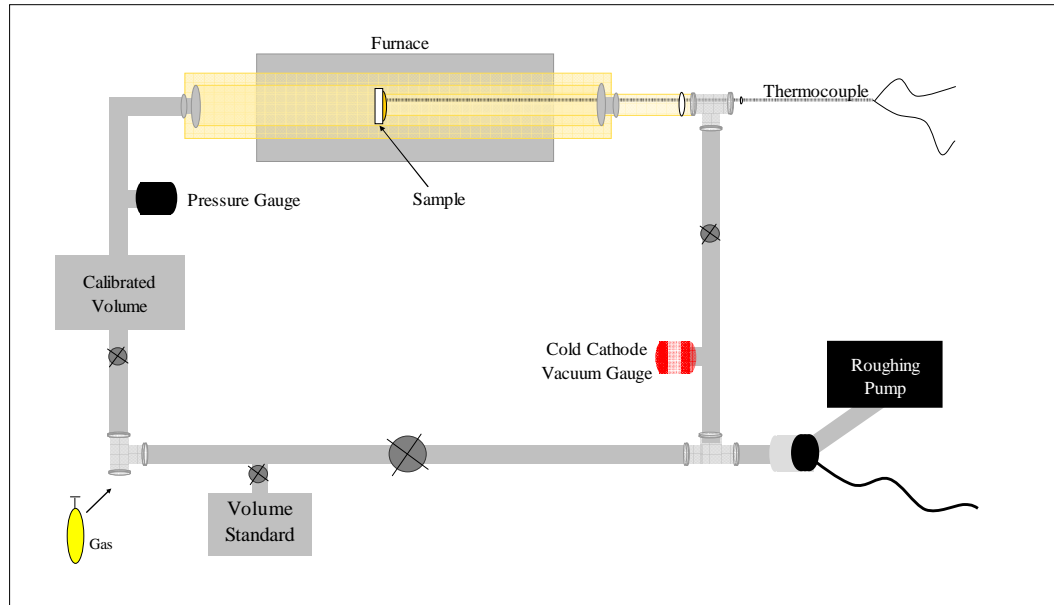


Figure 41. Pressure-drop measurement for the determination of hydrogen permeability through porous monoliths.

